Order Number 9402387

Electronic alignment of H(2p) from oriented $(H_2^+)^*$ produced in 4.0 keV H_2^+ collisions with helium

Calabrese, Dominic, Ph.D.

The University of Nebraska - Lincoln, 1993

U·M·I
300 N. Zeeb Rd.
Ann Arbor, MI 48106

ELECTRONIC ALIGNMENT OF H(2P) FROM ORIENTED $(H_2^+)^*$ PRODUCED IN 4.0 keV H_2^+ COLLISIONS WITH HELIUM

by

Dominic Calabrese

A DISSERTATION

Presented to the Faculty of

The Graduate College in the University of Nebraska

In Partial Fulfillment of Requirements

For the Degree of Doctor of Philosophy

Major: Physics &
Astronomy

Under the Supervision of Professor Duane H. Jaecks

Lincoln, Nebraska

August 1993

DISSERTATION TITLE

Electronic Alignment of H(2p) From Oriented $(H_2^+)^*$ Produced in 4.0 keV H_2^+ Collisions With Helium

BY

Dominic Calabrese

SUPERVISORY COMMITTEE:

APPROVED	DATE
Duane H Jaecks Signature	July 6-93
Duane H. Jaecks Typed Name	
William B. Campbell Signature	July 9, '93
William B. Campbell Typed Name	
M Eugene Rudd Signature	Aug 3, 1993
M. Eugene Rudd Typed Name	
Anthony F. Starace Signature	
Anthony F. Starace Typed Name	
Gordon A. Gallup Signature	
Gordon A. Gallup Typed Name	
Signature	
Typed Name	

GRADUATE COLLEGE
UNIVERSITY OF NEBRASKA

ELECTRONIC ALIGNMENT OF H(2P) FROM ORIENTED $(H_2^+)^*$ PRODUCED IN 4.0 keV H_2^+ COLLISIONS WITH HELIUM

Dominic Calabrese, Ph.D.

University of Nebraska, 1993

Advisor: Duane H. Jaecks

The electronic alignment of H(2p) from oriented $(H_2^+)^*$ produced in 4.0 keV H_2^+ collisions with helium is investigated for a variety of center-of-mass energies of the fragment particles. The experiment is performed by measuring the polarization of L_α in coincidence with the charged particle scattered at a specific laboratory scattering angle. The laboratory scattering angle and the laboratory energy of the charged particle not only specifies the instantaneous orientation of the parent molecule relative to the incident beam velocity, but also the center-of-mass energy of the fragment particles.

Photon and proton detection systems were specially designed and implemented to increase data collection efficiency. This was important because of the time-consuming nature of the photon-particle coincidence method.

In special cases, symmetry arguments for the collision system are employed in order to qualitatively assess and predict the characteristics of the nascent charge cloud. These arguments also help one to qualitatively predict the possible symmetries of the excited states of the parent molecule.

The results are discussed in order to determine the efficacy of existing models for the $(HeH_2)^+$ complex.

To my parents

Giacomo

and

Antonia

who taught me

Il denaro fa l'uòmo ricco, l'educazione lo fa signore

ACKNOWLEDGEMENTS

I would like to personally thank Professor Duane H. Jaecks for suggesting this topic. His guidance and assistance throughout this project was invaluable.

This project could not be completed without the assistance and support of many individuals. My sincerest gratitude and thanks go to Dr. Orhan Yenen and Lisa M. Wiese for their patience and understanding in teaching a mechanically inexperienced graduate student the "ins" and "outs" of the North Accelerator in the sub-basement at Behlen Laboratory. I would also like to thank Lisa for her painstaking assistance in aligning the parallel-plate analyzer. Frequent discussions on experimental atomic and molecular physics, with the always enthusiastic Dr. Yenen, have enlightened and enriched my understanding of the subject.

I am indebted to Don Fuerhing (posthumous) and his machine shop staff. Special thanks go out to Mr. Jack Loos who was responsible for the construction of much of the apparatus necessary for this project. Finally, I would like to thank Bob Kelty and his electronic shop staff for their technical assistance and support.

I wish to thank George W. Kerby III and Brian W. Moudry for their support throughout my seven years here at UNL. Our spirited discussions on physics, politics, sports, and other subjects have informed me greatly.

Special thanks also go out to my mentors at DePaul University. I would especially like to thank Dr. Anthony F. Behof and Dr. Gerard P. Leitz in encouraging me to attend graduate school.

I am deeply indebted to my wife Rosie whose constant support and encouragement have helped me through the many pitfalls which occur during graduate school. I am also deeply indebted to her patience and understanding during my seven years at UNL. Without her constant

emotional support, this project could not be possible.

At this point, I would like to express my gratefulness and love to my parents, Giacomo and Antonia, and my brother Frank for their encouragement and support throughout each level of my education. Their support will always be remembered.

Lastly, I would like to thank Almighty God providing me with patience, strength, and understanding through the gifts of His graces.

TABLE OF CONTENTS

LIST OF FIGURES

CHAPTER 1

INTRODUCTION

Although there have been numerous investigations of inelastic processes involving kilo-electron-volt atom-molecule collisions, many aspects of the underlying collision mechanisms remain a mystery. Difficulties in understanding these processes are incurred from the large number of degrees of freedom associated with the molecule. Therefore, a deeper understanding of such processes requires one to study the simplest atom-molecule system, namely H_2^+-He.

Because of its simplicity, the H_2^+-He complex has been the subject of many studies over the past 25 years. Early investigations of proton production from keV energy H_2^+ collisions with He suggested that transitions from the $1s\sigma_g$ to the $2p\sigma_u$ state (refer to Fig. 1.1) dominated the collision process. However, these results were in contradiction with the results of Van Zyl *et al* (1964) which showed that the total cross section for proton production is of the same order of magnitude as the cross section for the combined production of H(2s) and L_α. These paradoxical results were addressed in the work of Jaecks *et al* (1983). They measured the polarized L_α radiation in coincidence with the scattered proton, resulting from H_2^+-He→H(2p)+H^++He for an H_2^+ projectile energy of 3.22 keV. Their results for the production of 5 eV protons in coincidence with polarized L_α resulting from the dissociation of H_2^+ when the internuclear axis of the molecule was

perpendicular to the incident beam direction, showed that the dominant L_α producing transition was the excitation from $1s\sigma_g$ to the $2p\pi_u$ state. This was the first observation of electronic alignment in molecular excitation of oriented molecules. They postulated that two excitation channels dominate in the production of protons from the collision-induced dissociation of H_2^+ on He, namely the $2p\pi_u$ state for H_2^+ perpendicular to the beam direction; and the $2p\sigma_u$ state for H_2^+ parallel to the beam direction. The results were interpreted within the quasidiatomic model (Dowek *et al* 1982 and Yenen 1986).

In the case of near-zero energy projectile-frame protons, the production of these fragments was attributed to (1) $1s\sigma_g$-$2p\sigma_u$ transitions from H_2^+ at large internuclear separations and high vibrational states; (2) vibrational excitation into the continuum of the $1s\sigma_g$ state; and (3) predissociation by tunneling through a rotational barrier induced from a series of collisionally produced rotation-vibration quasi-bound states (Fournier *et al* 1987). Recently, an additional mechanism for near-zero energy projectile-frame protons was introduced by Jaecks *et al* (1990). They measured the near-zero energy center-of-mass frame protons from H_2^+-He collisions at 4.0 keV, when the internuclear axis was parallel to the incident beam velocity. Their results suggested that direct electronic excitation from $1s\sigma_g$ to the $2p\pi_u$ and $3d\sigma_g$ was the dominant process for such near-zero center-of-mass protons produced in the collision-induced dissociation of 4.0 keV H_2^+ on He. Furthermore, since this process occurs at 2.5-3 times the equilibrium separation of H_2^+, only the ν=9-11 vibrational states contribute to the observed protons. However, a measurement of the relative contribution of the excited states was not possible.

Even though these studies have enhanced the previously accumulated knowledge of the $(HeH_2)^+$ complex, some aspects of inelastic processes in ion-molecule collisions are still unclear. For example, consider the following three questions. First, how does one identify the molecular states which produce protons for various center-of-mass energies from the dissociation of oriented H_2^+ molecules? The work of Yenen (1986) answers this question for only one particular molecular orientation and center-of-mass energy, since his proton energy analyzer did not have sufficient energy resolution to distinguish between different velocity vectors resulting from various proton velocities and H_2^+ orientations. Secondly, what is the relative contribution of the $2p\pi_u$ and $3d\sigma_g$ molecular states to the observed near-zero energy projectile frame protons? Thirdly, can the answers to the above questions be interpreted in terms of some existing model for this prototype atom-molecule collision complex? Over the past 20 years, several models such as the quasidiatiomic (Jaecks *et al* 1983), triatomic cubic correlation diagram (Dowek *et al* 1982), and diatomics-in-molecules (Kuntz 1972) treatments have been introduced to explain atom-molecule collisions. To date, the viability of these models has yet to be critically tested.

This thesis is an attempt to answer the some of the above questions. The work described below is a report on several measurements for the electronic alignment of oriented molecules obtained by the polarized photon-particle coincidence technique. In particular, the process under consideration is the production of $H^+ + H(2p)$ from the collision-induced dissociation of 4.0 keV H_2^+ incident on He. Although time consuming, optical alignment measurements such as these can test and probe theory in a critical way.

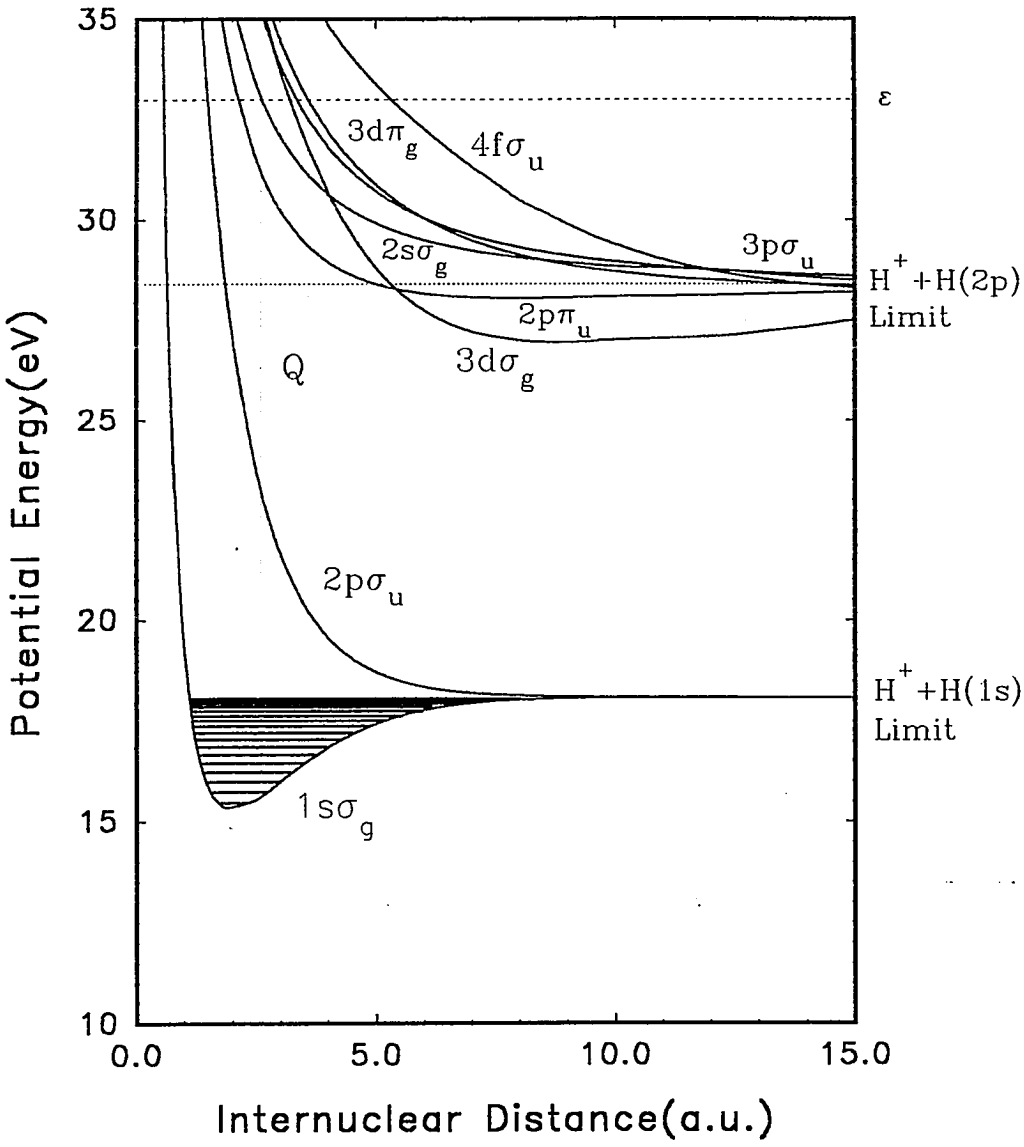

Figure 1.1: H_2^+ energy curves which includes the six states producing L_α. A transition for an arbitrary inelastic energy loss Q is also shown. Part of the inelastic energy loss goes into the center-of-mass energy, ε, of the fragments. Note the number of states that contribute to a particular ε. An alignment measurement and an estimate of Q will help in determining the excited states producing the observed protons. Note that the ground vibrational states are also shown. Data for the plots are obtained from Bates et al (1953), and Madsen and Peek (1971).

CHAPTER 2

THEORY

2A. INTRODUCTION

In order to gain a deeper understanding of atomic and molecular collisions, theory and experiment must complement each other. For slow and intermediate velocity collisions, the benefits of this statement have been manifested by treating such collisions as the formation of a temporary molecule (Lichten 1980). This idea originated from two theories, namely, the Born-Oppenheimer approximation (1927) and the Hund-Mulliken molecular orbital method (1927).

It is well known that the Born-Oppenheimer approximation breaks down when two energy curves are nearly degenerate (see Fig. 2.1). This occurs because the neglected term which couples the nuclear and electronic motion become significant. One handles this problem by introducing degenerate perturbation theory. In this approximation the curve crossing is avoided and the wave function becomes a linear combination of the nearly degenerate states. As a consequence, states of the same symmetry cannot cross (Neumann and Wigner 1929). Moreover, these such curves can only describe elastic processes in qualitative analyses. These orbitals, which are eigenfunctions of the electronic Hamiltonian for fixed internuclear separation, form part of what is termed an

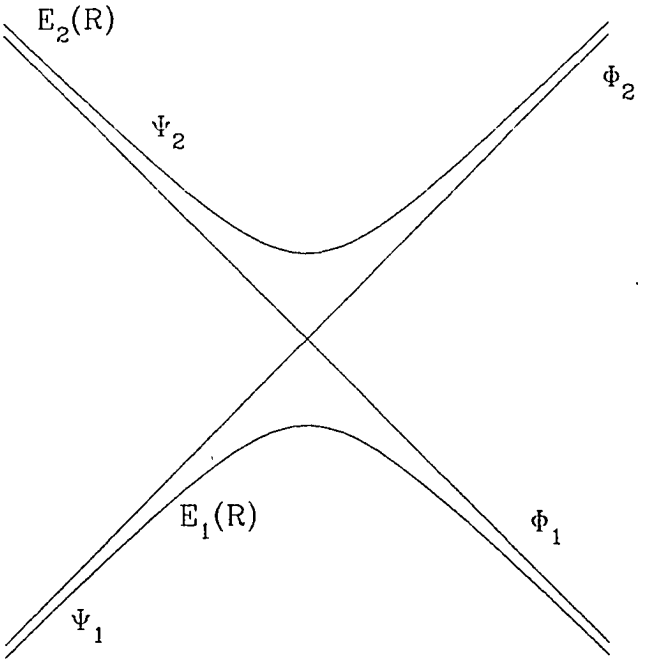

Figure 2.1: Region where two adiabatic curves Ψ_1 and Ψ_2 become nearly degenerate. In this region the Born–Oppenheimer approximation breaks down. Furthermore, the character of the adiabatic orbitals change rapidly. On the other hand, the nature of the diabatic orbitals Φ_1 and Φ_2 do not change very much in the degenerate region; therefore, they must cross.

adiabatic basis. They lead to the construction of adiabatic correlation diagrams. This basis has had limited success in quantitative calculations (*e.g.* low energy collisions of highly ionized particles with monatomic hydrogen). For further details, the interested reader is referred to the excellent review by Basu *et al* (1978).

In situations where the temporary molecule has many electrons, the electron motion becomes more complex. Inelastic effects which become important do not manifest themselves unless quantitative theoretical studies include many adiabatic terms. Since too few terms were used in initial theoretical investigations, theoreticians were unsuccessful in predicting the results of Ziemba and Everhart (1959). This led Lichten (1963) into using molecular states built up from molecular orbitals which obey the independent particle model (Hund-Mulliken 1927). Thus, the total wave function which neglects electron-electron interactions is a product of one-electron wave functions. These states form a diabatic basis. In this basis, two states of the same symmetry can cross. Qualitatively speaking, as the particles approach each other, part of the electron flux in state ϕ_1 can drain into state ϕ_2 (see Fig.2.1). This is called a diabatic transition. It is also possible that the incoming particles produce a diabatic type transition and the outgoing particles produce an adiabatic type transition. These types of "nonadiabatic" processes are responsible for interference effects in cross section measurements (Bobashev 1978 and Heinrichs 1968).

The success of this convenient basis led Fano and Lichten into introducing the electron promotion model to explain inelastic effects in Ar^+-Ar collisions. This enabled atomic physicists to construct diabatic correlation diagrams for qualitative analysis of

various collision systems. With the subsequent extension of this model to asymmetric collision systems (Barat and Lichten 1972), it has been possible to quantitatively and qualitatively interpret salient features in processes such as the production of inner-shell vacancies in ion-atom collisions (Anholt 1985 and Fastrup and Kessel 1978); interference in elastic and inelastic collisions (Rosenthal and Foley 1970 and Lichten 1980); and to some extent outer-shell excitations (Barat 1980).

To describe excitation mechanisms in atom-molecule collisions several models have been introduced. Dowek *et al* (1982) introduced the cubic and cylindrical correlation diagrams for triatomic systems, by generalizing the Barat-Lichten (1972) rules to three-particle atom-molecule complexes. The qualitative quasidiatomic model (Jaecks *et al* 1983) which utilizes the Barat-Lichten (1972) rules treats the molecule as an atom, since the lower lying levels of small molecules are atom-like in nature (Herzberg 1966). There is also a semi-empirical adiabatic scheme for estimating energies of polyatomic molecules in terms of energies of various states of the diatomic fragments of the temporary molecule. This is called diatomics-in-molecule model (Kuntz 1972). However, there are no good "rules of thumb" or Fano-Lichten (1965) type curves to describe molecular excitation processes. Nor are there general excitations mechanisms (such as translational and rotational coupling characteristic of atom-atom collisions) which are attributed atom-molecule collisions.

The purpose of this chapter is to introduce the various models used in interpreting atom-molecule collisions. The advantages and disadvantages will be briefly discussed. Before delving into the details of the various models concerning the $(HeH_2)^+$ complex,

one must become acquainted with the H_2^+ molecule. It seems appropriate at this point to discuss the H_2^+ molecule and its basic dissociation dynamics.

2B. THE H_2^+ MOLECULE

2B.1 BASIC IDEAS

H_2^+ is one of natures simplest molecule. It is one of the few molecules in which its Schroedinger equation is separable within the Born-Oppenheimer approximation (1927). Thus its energy curves are known with high precision (Bates *et al* 1953 and Peek 1971).

The potential energy curves are shown in Fig. 1.1. Because the present work deals with the dissociation of H_2^+ into $H^+ + H(2p)$, six molecular states can contribute to the observed protons: they are the $2s\sigma_g$, $3d\sigma_g$, $3p\sigma_u$, $4f\sigma_g$, $2p\pi_u$, and the $3d\pi_u$ states. The π-states dissociate into $H^+ + H(2p_{\pm 1})$, while the σ-states dissociate equally into $H^+ + H(2p_0)$ and $H^+ + H(2s)$ due to Stark mixing.

In this experiment H_2^+ will be produced by direct ionization of H_2 by high energy electrons. Consequently, the ion is initially in a Franck-Condon distribution of $1s\sigma_g$ vibrational states. The Franck-Condon factors have been calculated by Dunn (1966). A histogram of these population factors is shown in Fig. 2.2. One can easily see that the $v=2$ state is most heavily populated. On the other hand, the rotational distribution of H_2^+ will not differ much from the Boltzmann distribution of its parent moleHxle (Los and Grovers 1978).

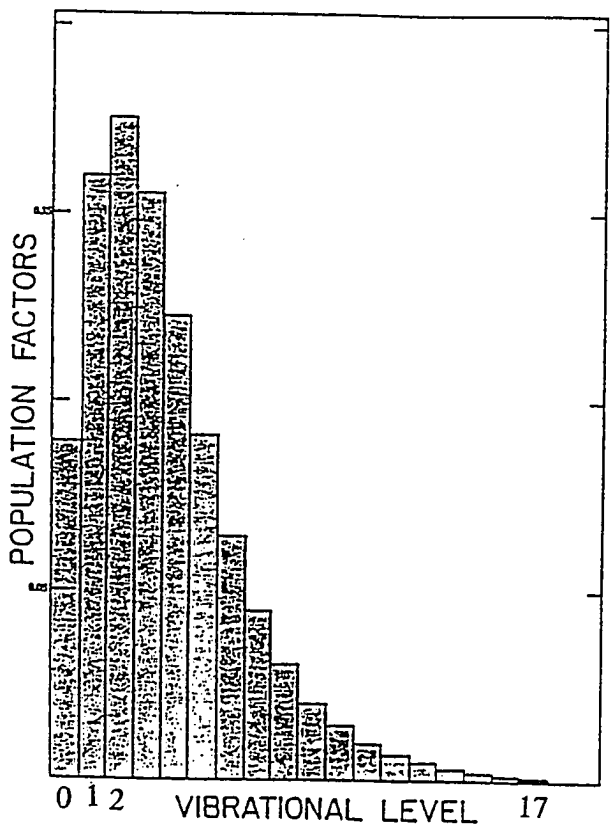

Figure 2.2: Franck–Condon factors for the ground state of H_2^+ (from of Dunn 1966).

2B.2 H_2^+ DISSOCIATION; BASIC COLLISION DYNAMICS

Dissociation takes place if the inelastic energy loss incurred during the collision is greater than the binding energy of the molecule. This statement assumes that electronic transitions to bound excited states do not occur. It has been shown that the $3d\sigma_g$ and $2p\pi_u$ states can support bound states at large internuclear separations (Beckel *et al* 1973 and Shafi *et al* 1973).

One question remains, " How does the molecule dissociate?" The answer to this question is based on the comparison of the collision time, the vibrational and rotational times, and the dissociation time of the molecule. It can be shown that typical collision times are of the order of 10^{-16} sec. However, typical vibration, rotation, and dissociation times are 10^{-14}, 10^{-13}, and 10^{-15} seconds, respectively. This means that the vibrational and rotational motions remain frozen during the dissociation process. It also means that the dissociation process occurs in two steps, excitation with subsequent dissociation. This is analogous to the application of the Franck-Condon principle in the excitation of molecules by photon impact. This two step approximation is called the axial recoil approximation (Zare 1967).

Since the dissociation takes place along the internuclear axis and since the z-component of the angular momentum of H_2^+ is to be defined parallel to the internuclear axis, the quantization axis for the dissociating molecule will be the internuclear axis.

2B.3 DISSOCIATION KINEMATICS

Consider the collision-induced dissociation of a diatomic molecule with initial energy E_o. When the molecule is excited, it loses an amount of energy Q (see Fig. 1.1).

This quantity is comprised of the energy difference between the molecule's initial vibrational state and the vibrational continuum, the total energy needed to excite the fragment particles (in this case the 2p state of H), and the total kinetic energy ϵ imparted to the fragments above the H^+-H(2p) dissociation limit. Actually Q and thus ϵ are averages from a distribution of inelastic energy losses and center-of-mass energies, since transitions may occur at different internuclear separations. Nonetheless, energy analysis and coincidence spectra still make it possible to obtain insights of the collision process.

Because of conservation of energy and momentum, each fragment particle acquires a center-of-mass energy $\epsilon_+=\epsilon/2$. This is shown in the Newton diagram of Fig. 2.3. The laboratory kinetic energy of the fragment particles are written as

$$E_{\pm} = \frac{1}{2}m(\vec{V}_o \pm \vec{v})^2 = \frac{1}{2}mV_o^2 + \frac{1}{2}mv^2 \pm m\vec{v}\cdot\vec{V}_o \qquad (2.1)$$

where $\bar{V}_o$ is the velocity of the center of mass of H_2^+; v is the velocity of the fragment in the center-of-mass; and the $\pm$ sign represents the forward and backward scattered fragments in the center-of-mass frame. In terms of E_o, Q, and ϵ_+ the above quantity is written as

$$E_{1_{\pm}} = \frac{E_o - Q}{2} + \epsilon_+ \pm 2\sqrt{\frac{(E_o - Q)\,\epsilon_+}{2}}\cos\phi \qquad (2.2)$$

where ϕ is the orientation of the molecule relative to the beam axis. Further quantitative

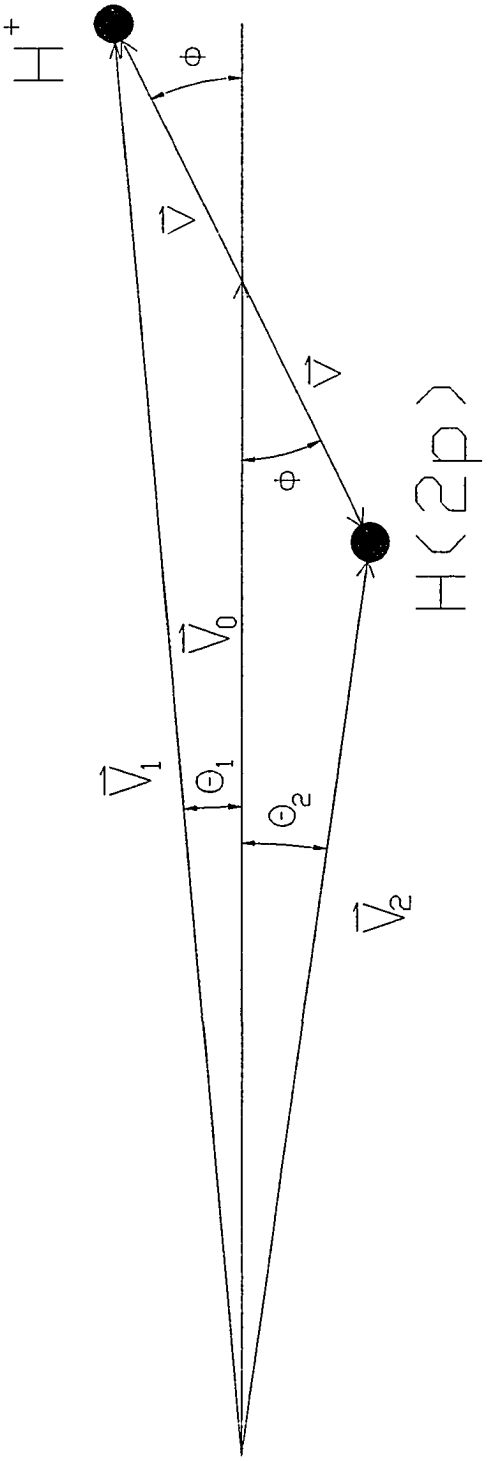

Figure 2.3: Newton diagram depicting H_2^+ dissociation kinematics. The deflection of the molecule's center-of-mass is not shown.

details of H_2^+ kinematics are presented in Appendix C.

2C. THE TRIATOMIC MODEL FOR $(HeH_2)^+$

Consider the cubic correlation diagram shown in Fig. 2.4 (Dowek *et al* 1982). The values R and r represent the center-of-mass to center-of-mass distance from the molecule to the atom and the internuclear separation of the molecule, respectively. Three faces of the cube represents correlation diagrams for limiting diatomic cases. These correlation diagrams obey the Barat-Lichten rules (1972) where the number of radial nodes is conserved along each separate face. Once each face is completed, the energy surfaces are drawn from continuity considerations. Excitations occur through the promotion of various surfaces. In Fig. 2.4(a), the linear formation $C_{\infty v}$ of the triatomic molecule is considered.

On the first face (1) of the cube r=0 and R varies from 0 to ∞. This represents the fusing of two H-atoms into He. Hence, face (1) corresponds the He-He correlation diagram with Be united atom limit. Face (2) has R=∞. Thus it represents H-H correlation diagram with the atomic levels of He at united atom limit of H-H. The third face (3) where r=∞ requires special consideration. When R=r/2 the He atom coincides with one of the H atoms forming Li united atom. On either side of this point, one has an H-He correlation diagram. This face actually depends on the geometry of the three particles. If the internuclear axis of the molecule is aligned perpendicular to the beam direction, this face corresponds to the three isolated atoms. Thus a separate cube is needed for different orientations of the molecule. Finally, face (4) with R=0 corresponds to the only triatomic face. At r=∞ the atoms are completely separated. However as r

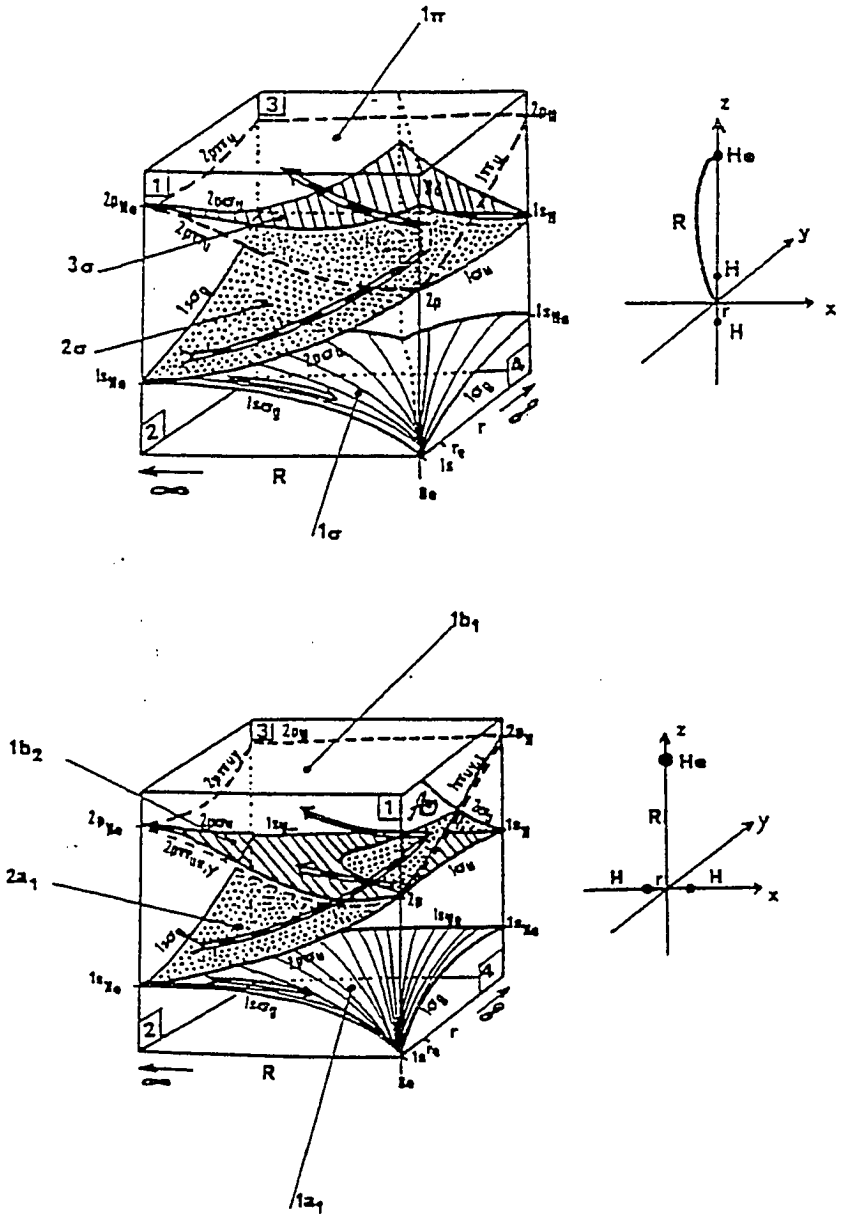

Figure 2.4: Cubic correlation diagrams for the $(HeH_2)^+$ complex for the (a) collinear approach and (b) perpendicular approach (from of Dowek et al 1982).

approaches 0, the atoms united into Be.

In most situations, r is of the same order as the equilibrium separation of the molecule. Thus, one can draw cuts of the cubes keeping r fixed. One can then analyze the complex for various internuclear orientations by making such cuts in the $C_{\infty v}$ and C_{2v} conformations at $r=r_e$ and interpolate the surfaces between these extremes. The result is a cylindrical correlation diagram. An example is shown in Fig. 2.5.

In situations where the internuclear separation and relative orientation of the molecule are approximately known, the collision mechanisms for the complex can be interpreted with a correlation diagram which corresponds to a cut in the cube parallel to face (1). Kubach *et al* (1985) have calculated such curves for the $C_{\infty v}$ and C_{2v} configurations at $r=1.4a_0$.

Although it has been fruitful in explaining one and two electron processes observed in the $(HeH_2)^+$ complex (Dowek *et al* 1982 and Sidis and Dowek 1983), the cubic correlation diagram has some disadvantages:

1. existing cubes are only drawn for a few excited states of the complex. Not all of the states leading to $He+H^+ +H(2p)$ are considered.
2. the numerous surfaces in the cube make the interpretation of various processes quite difficult.
3. extension to polyatomic systems would require the construction of multidimensional surfaces; thus, making visual analysis extremely difficult, if not impossible.
4. only atom-homonuclear diatom correlation diagrams exist. In cases where

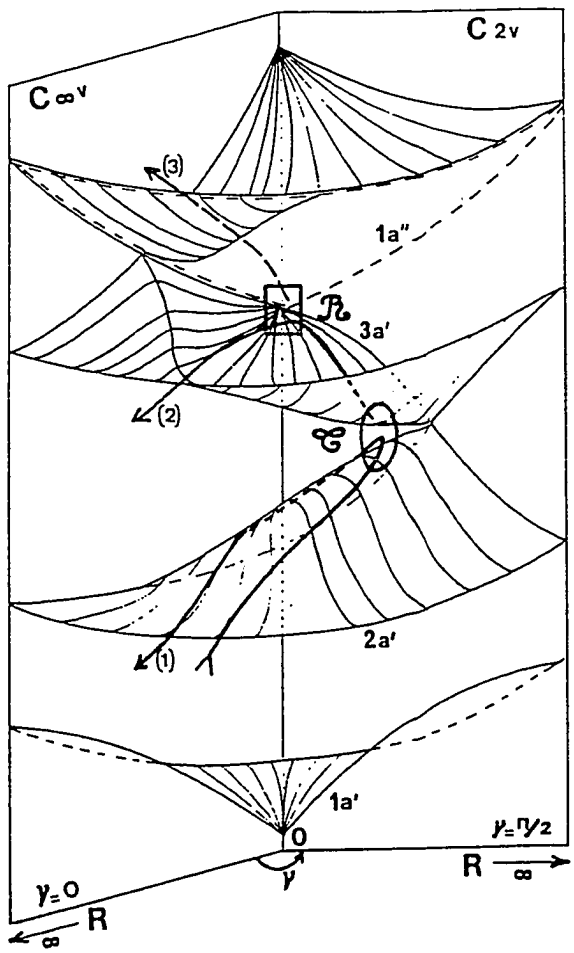

Figure 2.5: Cylindrical correlation diagram for the $(HeH_2)^+$ complex at $r=r_e$ (from of Dowek et al 1982).

the molecule is heteronuclear, the implications to face (3) are not known.

5. one must draw different correlation cubes for different relative orientations of the system.

2D. QUASIDIATOMIC MODEL

As mentioned above, the wave functions for the low lying levels of small molecules are atom-like in character. Thus one treats the molecule as if its internuclear separation is zero. This is the basis of the quasidiatomic model. Although its details have been discussed extensively by Yenen (1986), a brief outline of the model will be presented to familiarize the reader with some of its basic features.

Since the molecule is treated as an atom, one constructs the correlation diagram by generalizing the Barat-Lichten rules (1972); moreover, by conserving the number of radial nodes. The united atom limit corresponds to the united atom energy levels. In this case they correspond to the energy levels of Be. In the separated atom/molecule limit, the energies correspond to the atomic energy levels of the atom and the molecular energy levels of the molecule at its equilibrium separation. Finally, since the molecule behaves like an atom, the model is independent of the internuclear orientation of the molecule. A quasidiatomic correlation diagram for the $(HeH_2)^+$ system is shown in Fig. 2.6.

Because the molecule is treated as an atom, it seems that the model would be useful in analyzing processes where molecular excitation takes place at small internuclear separations. This was exactly the case in the experiment of Jaecks *et al* (1983), where the electronic alignment in the molecular excitation of H_2^+ was measured. They deduced that the observed protons had a center-of-mass energy nearly equal to 5 eV. Since the

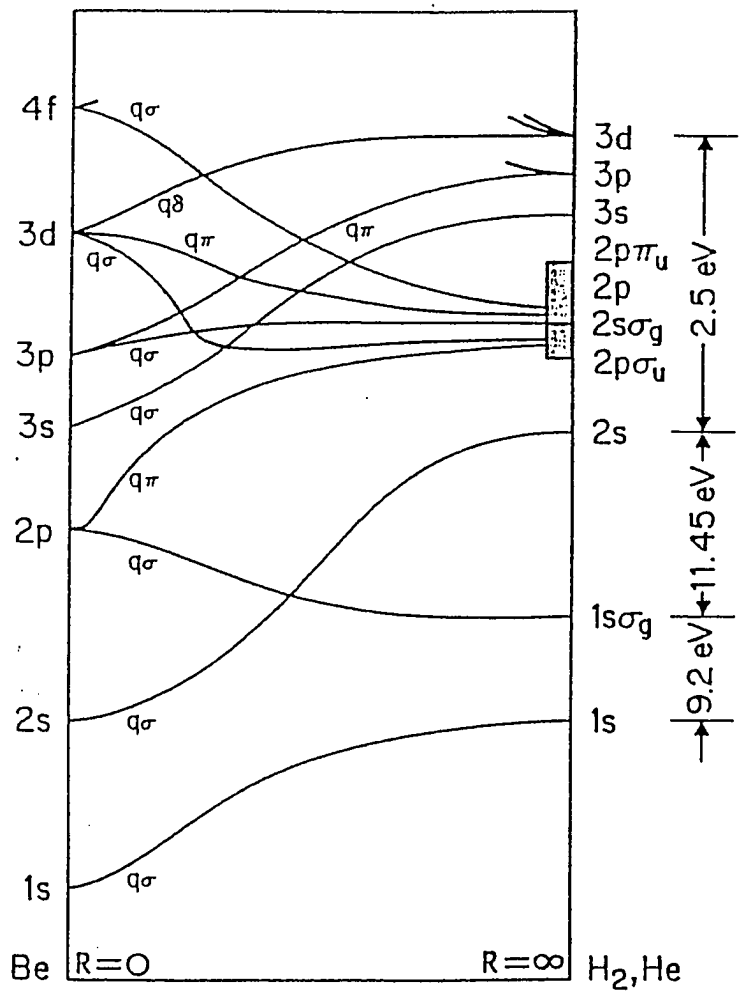

Figure 2.6: Quasidiatomic correlation diagram for the $(HeH_2)^+$ complex. R denotes the center-of-mass to center-of-mass separation between H_2 and He. The energies at the separated atom limit are not known precisely because of the uncertainty principle. This is the reason for the shaded region shown.

inelastic energy loss is large, the channel producing $H^+ + H(2p)$ must occur at small internuclear separations of the molecule. However, consider, for example, a process that produces protons at the $2s\sigma_g$-$3d\sigma_g$ crossing of the H_2^+ molecule. In this case the molecule cannot be considered atom-like since the internuclear separation is large. In the present experiment, the channels producing near-zero energy projectile frame $H^+ + H(2p)$ occur at 2-3 times the equilibrium separation of the molecule. This means that the applicability and viability of this model will be severely tested.

2E. OTHER MODELS

Recently, Russek and Furlan (1989) introduced a new class of diabatic states through a topologically composed diabatic Hamiltonian. Their results for two internuclear orientations, 60° and 90° relative to the beam axis, predict the collisional dissociation of H_2^+ to the $2p\sigma_u$. Their results successfully predict target excitation of He (Rydberg-excited) as observed by Quintana *et al* (1989). Finally, the diabatic curves suggest the possibility of Rosenthal oscillations in the charge exchange channel due to a crossing between the charge exchange channel and the target excitation channel at large internuclear separations. However, the mechanisms producing the $H^+ + H(2p)$ excitation channels could not be discussed, since their calculation does not include "π-like states" of the triatomic system.

Calculations of the adiabatic curves of the $(HeH_2)^+$ complex do exist. One of the first such calculations employed the semi-empirical diatomics-in-molecules model (Kuntz 1972). Afterward Mclaughlin and Thompson (1979) performed an *ab initio* calculation of the lowest four doublet-spin state eigenfunctions and energy surfaces of $\bar{H}e\bar{H}_2^+$.

However, only the lowest lying energy surfaces do exist; thus, making theoretical interpretations of the results impossible.

Since it is well known that the diatomics-in-molecules model is effective at large internuclear separations (Pollack and Hahn 1986), and since it is a fast method of obtaining the energy surfaces, it is hoped that many more states of HeH_2^+ are calculated. This could enable one to perform a calculation on this system by implementing the close-coupling approach (Kimura and Lane 1990).

Each of the models presented above has its limitations. This is mainly due to the inherent complexity of molecules.

CHAPTER 3

THE COINCIDENCE METHOD: BASIC IDEAS

3A. INTRODUCTION

Angular correlation and polarization data obtained from the particle photon coincidence technique allow the experimentalist to determine the magnetic substate populations of atoms. In particular, a polarization study (coherence experiment) may completely determine the excited state in the process $A+B \rightarrow A^{*}+B$. This "third-generation" type of experiment goes beyond the limited capabilities of the differential and total cross section measurements (Anderson 1988). Consequently, an abundance of detailed information of the underlying collision mechanisms in electron-atom (or molecule) and atom-atom (or molecule) studies have been produced (Anderson *et al* 1988). For example, the information obtained from coherence studies from various atom-atom processes has led to establishment of the so-called propensity rules (Anderson 1988).

Macek and Jaecks (1971) and Fano and Macek (1973) were the first to lay the

theoretical ground work for this technique. Their results express the measured polarization data in terms of atomic excitation amplitudes. However, very little work exists in expressing polarization data in terms of molecular excitation amplitudes. Two noteworthy efforts are Montgomery's (1982) calculation for $He^+ + H_2$ collisions, and Blum and Jakubowicz (1978) calculation for electron-molecule scattering. It will be shown in Sect. 3C.1 that the former calculation is not applicable in this experiment. The results of Blum and Jakubowicz (1978) have been applied in a few cases (see, for example, Malcoin and McConkey 1979).

Therefore, it is the purpose of this chapter to briefly discuss the basics of the particle-photon coincidence method as applied to polarization studies. Fundamentals pertinent only to this study will be discussed. Thus p-s transitions will only be considered. The basic ideas presented in Sect. 3B will be applied to the presented experiment in Sect. 3C. The emphasis will be on the simple physical and mathematical features. Elaborate physical and mathematical details are discussed in the articles by Fano and Macek (1973), and Anderson *et al* (1988).

3B. THE POLARIZATION PATTERN

3B.1 GENERAL IDEAS

To completely specify the state of polarization of light emitted perpendicular to the scattering plane in an atom (electron)-atom collision, a polarizer must be used in conjunction with a retarder (Fig. 3.1). If the fast axis of the retarder is at angle ß and the polarizer is at an angle α with respect to the incident beam direction z, the intensity

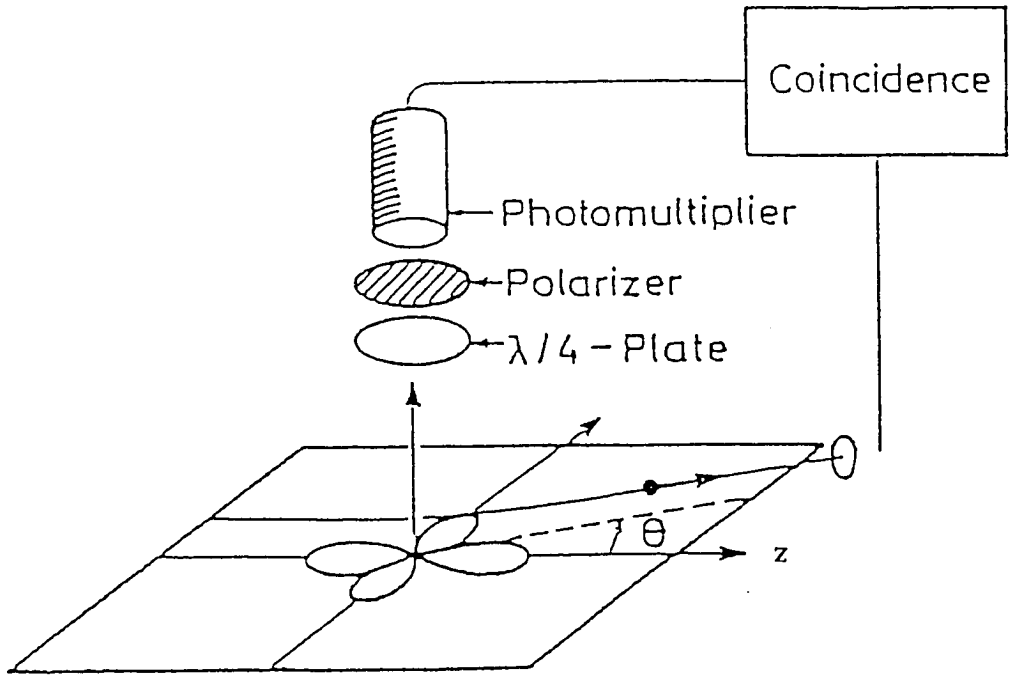

Figure 3.1: Schematic of the apparatus employed in photon–particle coincidence method. Both a polarizer and a quarter–wave plate must be used to completely specify the state of polarization of light emitted perpendicular to the scattering plane (from Anderson et al 1988).

is expressed as

$$I(\alpha,\beta) = \frac{I}{2}[1+P_1[\cos2(\alpha-\beta)\cos2\beta-\sin2(\alpha-\beta)\sin2\beta\cos\delta] + P_2[\cos2(\alpha-\beta)\sin2\beta+\sin2(\alpha-\beta)\cos\delta] + P_3[\sin2(\alpha-\beta)\sin\delta]] \quad (3.1)$$

where

$$P_1 = \frac{I(0^o,0^o,0^o)-I(90^o,0^o,0^o)}{I(0^o,0^o,0^o)+I(90^o,0^o,0^o)}, \quad (3.1a)$$

$$P_2 = \frac{I(45^o,0^o,0^o)-I(135^o,0^o,0^o)}{I(45^o,0^o,0^o)+I(135^o,0^o,0^o)}, \quad (3.1b)$$

$$P_3 = \frac{I(45^o,0^o,90^o)-I(135^o,0^o,90^o)}{I(45^o,0^o,90^o)+I(135^o,0^o,90^o)}, \quad (3.1c)$$

and δ is the phase shift introduced by the retarder (Wedding *et al* 1991). The quantities P_1, P_2, and P_3 are the relative Stokes parameters. Because P_3 measures the circular polarization of photons emitted perpendicular to the scattering plane and because each photon emitted from each sublevel of the excited p-state has its own characteristic polarization (m_l =-1, right-hand circulation of the charge cloud; m_l=1, left-hand

circulation of the charge cloud; and $m_l=0$, no circulation), P_3 is a measure of the average angular momentum the detected photon carries in a p to s transition. In cases where the Hamiltonian describing the process has positive reflection symmetry, these three parameters are sufficient in describing the excited p-state (Anderson *et al* 1988). Experiments designed to measure the three Stokes parameters are called coherence analysis studies.

In the present experiment we perform a linear polarization measurement (*i.e.* determination of P_1 and P_2 only). Hence, no circular polarization measurement is performed. Since $\beta=\delta=0$, equation (3.1) becomes

$$I(\alpha, 0^\circ, 0^\circ) = \frac{I}{2}[1+P_1\cos 2\alpha+P_2\sin 2\alpha]. \quad (3.2)$$

A schematic diagram for the present experiment is shown if Fig. 3.2. As opposed to atom (electron)-atom collisions, the scattering plane cannot be defined in the present experiment since many impact parameters will contribute to the observed processes.

Another simplification occurs if the scattered particle is collected at a laboratory scattering angle of 0°. In this case the initial and final momenta of the detected particle are in the same direction. This means that the observed process has axial symmetry along the initial and final beam axes. It has been shown that for any axially symmetric system the anisotropy of the charge cloud can be completely described by P_1 (Greene 1981). Note that in this case a particular scattering plane cannot be defined. In fact, there are infinitely many scattering planes contributing to the observed particle. Thus, the observed

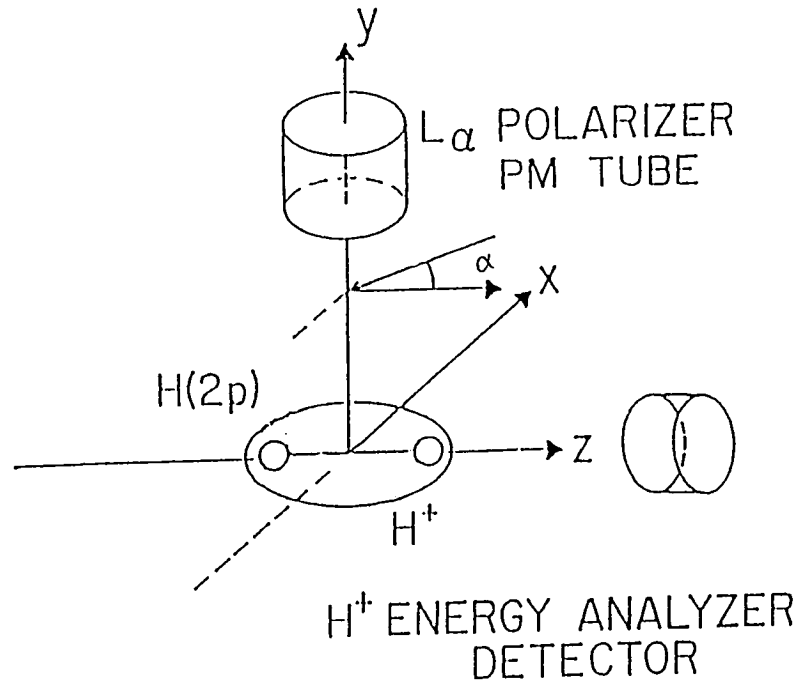

Figure 3.2: Schematic of the photon–particle coincidence method used in the present experiment. Since no quarter–wave plate is used only P_1 and P_2 can be determined. The absolute value of P_3 can also be determined if $P_1^2+P_2^2+P_3^2=1$.

phases of the scattering amplitudes are completely random (see below). Only when the cylindrical symmetry is broken can one measure non-zero P_2 and P_3. This occurs when a scattering plane is defined. Fig. 3.1 shows a process where the initial and final momenta are in different directions. Therefore, a scattering plane is defined. In this case the system has planar symmetry. Thus, P_2 and P_3 are measurable quantities.

Consider the polarization pattern shown in Fig. 3.3b. It is obtained by detecting the particle scattered at a specific angle in coincidence with the photons detected perpendicular to the xz-plane. Each point in the figure corresponds to the total number of coincidences for a specific polarizer angle. The figure represents a time-averaged projection of the electron charge cloud distribution (Fig. 3.3a) onto the xz-plane. The rate of these coincidences are proportional to the integral, over the electronic's resolution time, of the square of the dipole matrix element describing the p-s decay process (Macek and Jaecks 1971). This is written as

$$\dot{N}_c \propto \sum \int_0^{\Delta t} dt \, |\langle A_i| \, \hat{\epsilon}\cdot\vec{X} \, |A_f\rangle|^2, \qquad (3.3)$$

where $\hat{\epsilon}$ is the polarization vector of the emitted light; Δt, the resolution time of the electronic circuitry; $\langle A_i|$, the state vector representing the de-excited state; and $|A_f\rangle$, the state vector representing the excited state. Classically, one can consider equation (3.3) as representing the sum of one or more electric dipoles oscillators radiating coherently in time (Jackson 1975).

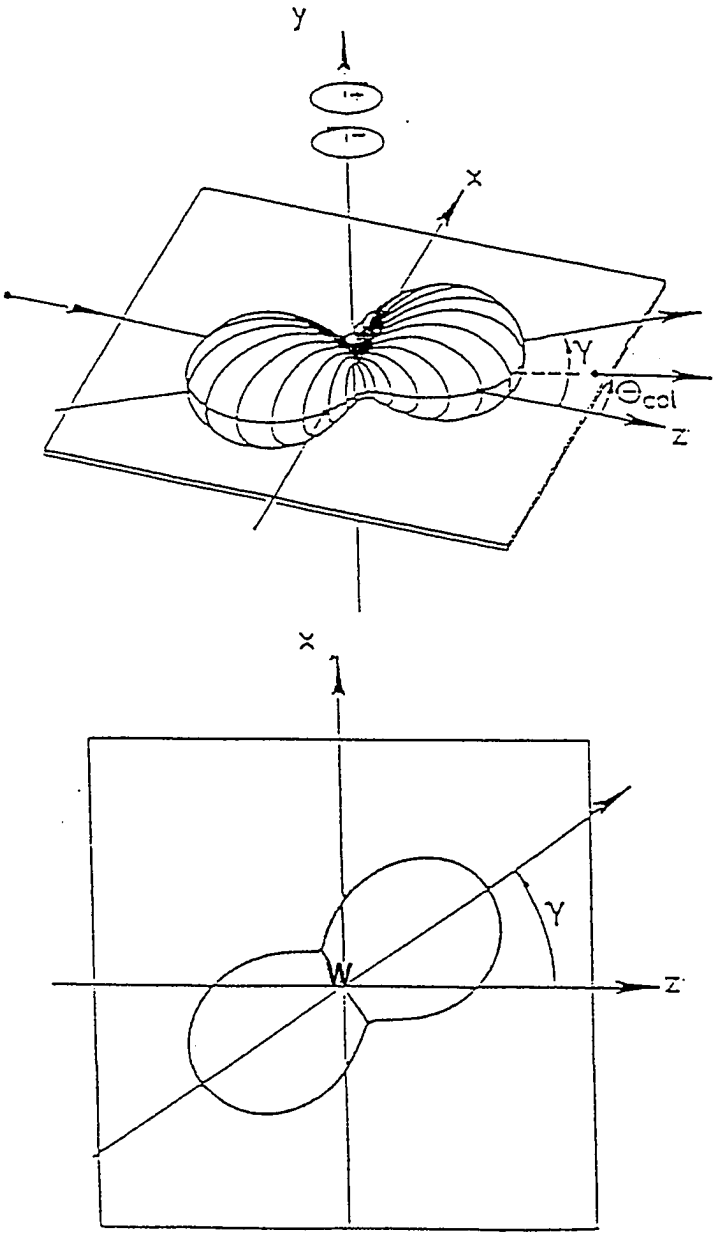

Figure 3.3: (a) Typical electron charge distribution for 2p−1s transition induced in a collision. (b) The present experiment measures the projection of the electron charge cloud onto the xz−plane (shown here). The angle γ represents the alignment of the charge cloud relative to the z−axis. In this experiment γ can only be 0° or 90° since P_2=0 (from Anderson et al 1988).

To further elucidate the features of the polarization pattern (Fig. 3.3b) and equation (3.3), we will consider the excitation of $He(2^1P_1)$ by electron impact, as discussed by Anderson *et al* (1988). The geometry of the experiment is shown in Fig. 3.1. In this case the scattering plane is defined as the xz-plane with the polarizer placed along the y-axis.

The excited p-state is written as

$$|p\rangle = a_1|1\rangle + a_0|0\rangle + a_{-1}|-1\rangle, \qquad (3.4)$$

where the a_i's are magnetic substate excitation amplitudes. However, because the Hamiltonian, and thus, the wavefunction have positive reflection symmetry about the scattering plane, $a_1 = -a_{-1}$. From equation (3.3), this yields two dipoles oscillating in the scattering plane, one in the z-direction and one in the x -direction. With $a_0^2 \sim \sigma_0 = |E_z|^2$ and $2a_1^2 \sim 2\sigma_1 = |E_x|^2$, the measured intensity is written as

$$I(\alpha, 0^\circ, 0^\circ) \propto \sigma_0 + (2\sigma_1 + \sigma_0)\sin^2\alpha + (2\sigma_0\sigma_1)^{1/2}\cos(\Delta\zeta)\sin 2\alpha, \qquad (3.5)$$

where σ_i's are cross sections for the magnetic substates; E_i's, the dipole fields classically representative of the matrix element in equation (3.3); α, the polarizer angle; and $\Delta\zeta$, the relative phase difference between the excitation amplitudes; or in a more classical sense, the phase difference between E_x and E_z. Thus, a constant phase difference results in coherent radiation of the excited state.

Using equations (3.1a-c), the Stokes' parameters are

$$P_1 = \frac{\sigma_0 - 2\sigma_1}{\sigma_0 + 2\sigma_1}, \qquad (3.6a)$$

$$P_2 = \frac{2(2\sigma_0\sigma_1)^{1/2}}{\sigma_0 + 2\sigma_1}\cos\Delta\zeta, \qquad (3.6b)$$

$$P_3 = \frac{2(2\sigma_0\sigma_1)^{1/2}}{\sigma_0 + 2\sigma_1}\sin\Delta\zeta. \qquad (3.6c)$$

The above equations satisfy the equation, $P_1^2+P_2^2+P_3^2=1$ if $\Delta\zeta$ is constant. If $\Delta\zeta$ is completely random, then P_2 and P_3 are equal to zero, resulting in completely incoherent radiation. Thus, the Stokes' parameters measure the degree of coherence for a particular process (see Anderson *et al* 1988).

There are two important points that must be emphasized about this example. First, since the excited state is a singlet state, fine and hyperfine interactions are neglected. In atoms where these interactions are important, the measured charge cloud is depolarized. It obtains a width w. (see Fig. 3.3b). The effects of this interaction will be briefly discussed in section 3B.3.

Second, since the processes of exchange and direct excitation are

indistinguishable, the excited state is pure. Consequently, only two Stokes' parameters are needed to describe the excited state (Anderson *et al* 1988). In general pure states do not occur. The effect of this phenomenon on the measured charge cloud will be discussed briefly in the next section.

3B.2 COHERENCE

In the process mentioned in Sect. A of this chapter, the state of particle B did not change. If it did, $|A_f>$ of equation (3.3) could not be written as a pure state. When an excited state, $B^*(1)$, also occurs, then the state $|A_f>$ will occur with probability p_{gnd} and p_1 for the respective ground and excited B states. Note that even if B is an electron (as in the example presented in Sect. B.1), the two probabilities are correlated with its spin states. In a coincidence measurement between A and its emitted photon, both B states will contribute to the observed signal. Thus, when more than one final state contributes to the observed signal, then many phase differences between the oscillating dipoles contribute to the observed radiation. This may result in the partial or complete destruction of coherence. Equation (3.3) is no longer valid, and the density matrix formalism must be applied. As described by Anderson (1988), the polarization depends upon weighted sum of Stokes' parameters. More formally, this means that $P_1^2+P_2^2+P_3^2<1$. Consequently, three Stokes' parameters are required to describe the excited p-state when atomic reflection symmetry is conserved (see Anderson *et al* 1988). If not, as in the case where the spin of a heavy atom flips during the collision, the charge cloud acquires a height, h; (as seen in the xy and yz-planes of Fig. 3.4) hence, a fourth Stokes's parameter, measured in the scattering plane, is required to describe the

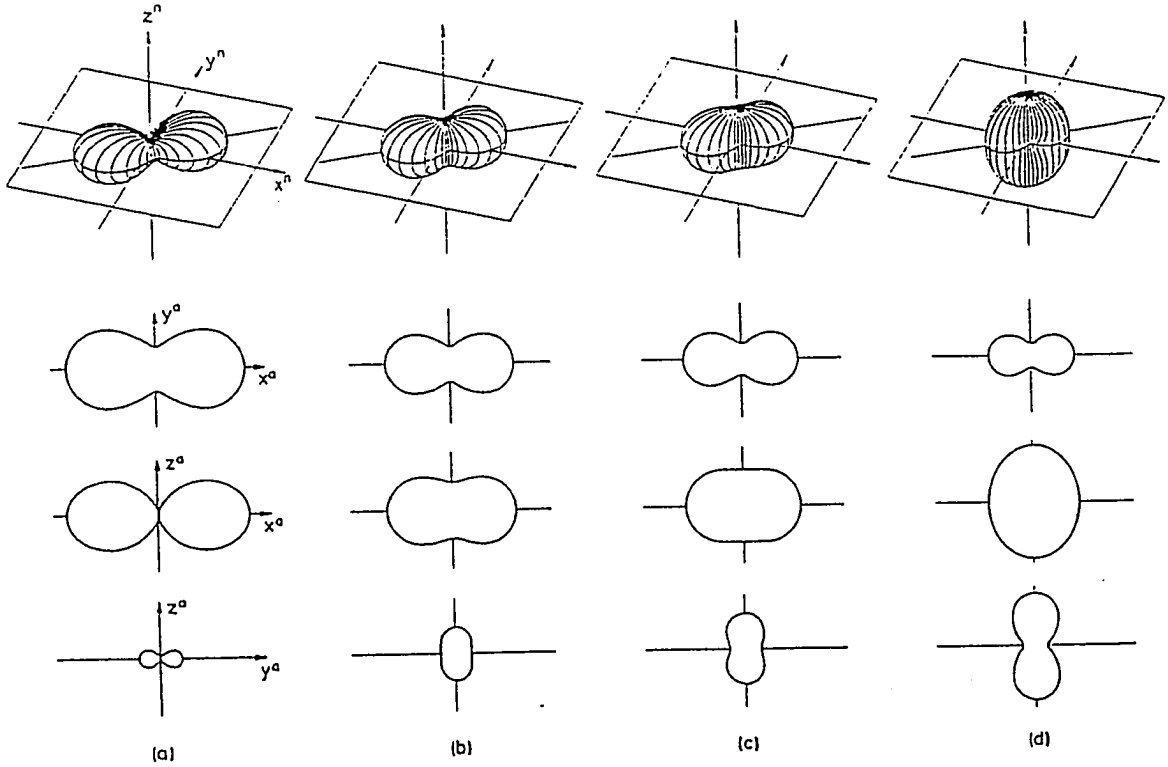

Figure 3.4 A depiction of a charge cloud when it obtains a height h due to a loss of atomic reflection symmetry. This can occur when a heavy atom flips its spin during a collision. The electron charge densities shown above have heights (a) h=0, (b) 1/4, (c) 1/3, and (c) 1/2. The quantity h is related to a fourth Stokes' parameter (see text) and the angular momentum transferred in the collision. Note that the charge cloud projections are shown relative to the atoms frame (from Anderson et al 1988).

excitation process. One possible way to regain the coherent situation is to perform the particle-photon coincidence for each known B state.

3B.3 DEPOLARIZATION EFFECTS

As previously mentioned, the experimentally obtained charge cloud distribution shown in Fig. 3.3b has a definite width w. In reality, the "dumbbell" shape of a p-state has a node at the origin. This depolarization effect can manifest itself for several reasons. They are categorized as follows:

Physical Effects:

1. cascades from higher lying levels;
2. the fine and hyperfine structure of the excited particle;
3. the orientation of the molecule (if the studied particle is a molecule);
4. the deflection of the center of mass of the molecule;

Apparatus Effects:

5. the finite angular resolution of the detectors;
6. the quality of the polarizer;
7. the energy resolution of the analyzer (see Ch.4 for its details); and
8. the energy definition of the incoming beam.

The last four causes are experimental in nature and self explanatory. Effects (3) and (4) will be discussed in Sect. C.

In the example mentioned above, the He atom does not have fine structure since the spin angular momentum, S, is zero. However, if the 2p state of H is excited, then fine structure exists. In such a case L precesses around J with a period of 10^{-12} seconds.

Since the lifetime of this state is 1.6×10^{-9} seconds, the angular momentum carried off by the photon changes as the radiation is emitted. Thus, an average value of $L_\perp$ is measured and a depolarized intensity pattern occurs. The calculations of Macek and Jaecks (1971), and Fano and Macek (1973) show how to take this effect into account. Using their results, Mueller (1982) showed that the intensity of the emitted radiation from H(2p) can be expressed as

$$I(\alpha, 0^\circ, 0^\circ) \propto (5\sigma_0+4\sigma_1) + (6\sigma_1-3\sigma_0)\sin^2\alpha + (3\sqrt{2\sigma_1\sigma_0}\cos\Delta\zeta)\sin 2\alpha \qquad \text{(C.7a)}$$

Written in terms of cross sections the quantities, P_1 and P_2, are then expressed as

$$P_1 = \frac{3(\sigma_0-\sigma_1)}{7(\sigma_0+2\sigma_1)}, \qquad \text{(3.7b)}$$

$$P_2 = \frac{6(2\sigma_0\sigma_1)^{1/2}}{7(\sigma_0+2\sigma_1)}\cos\Delta\zeta, \qquad \text{(3.7c)}$$

Hyperfine structure contributes in a similar fashion, but its effect is very small. Thus, its contribution is neglected. Also, it is assumed that the total spin of both particles is conserved before and after the collision (Percival and Seaton 1958). Finally, cascade

effects (*e.g.* 3p-1s transitions *etc.*) are also be neglected because the resolving time of the apparatus is good enough to discriminate against the long-lived, high, lying levels of H.

3C. APPLICATIONS TO MOLECULES

3C.1 H(2P) PRODUCTION FROM H_2^+ DISSOCIATION

The excited p state of H can be populated into either the m=0, ± 1 magnetic sublevels where the quantization axis is chosen to be the internuclear axis of H_2^+. Furthermore, a knowledge of the relative populations of the atomic magnetic substates will yield information about the excited dissociative state of the molecule involved in the process. As an example, if the dominant contribution to the emitted light comes from the m=0 magnetic sublevel, then one can show that either all or some the $2s\sigma_g$, $3d\sigma_g$, $3p\sigma_u$, or the $4f\sigma_u$ molecular states contribute to the observed radiation. One can effectively determine which of the molecular states contributes to the observed radiation, if the center-of-mass energies of the H_2^+ fragments is known, and if the inelastic energy loss Q is precisely known. It should be noted, however, that even though the present experiment directly measures the time-averaged shape of the atomic charge cloud (and yields information about the relative contributions of the molecular states), it does not directly yield the time-averaged shape of the excited state of the molecular charge cloud projected onto the xz-plane. This will be discussed further in Ch. 6.

In the present experiment, the initial state of H_2^+ is a weighted sum over the vibrational and rotational states of the $1s\sigma_g$ orbital. Also, the excited dissociative state of the molecule will occur over a distribution of internuclear separations and relative H_2^+-He

orientations. Lastly, many impact parameters will contribute in the excitation process. Therefore, it is very likely that the H(2p) state is incoherently excited ($P_2=0$). In special cases one can also make inferences about the nascent charge cloud through symmetry arguments.

Consider a process where the instantaneous orientation that the of the H_2^+ molecule is parallel to the incident beam direction as shown in Fig. 3.5. Recall from Ch. 2 Sect. 2B that the instantaneous orientation is a valid concept because the molecule dissociates along the internuclear axis. Because of cylindrical symmetry, P_2 will always be zero (Greene 1981). Therefore, the measured charge cloud of H(2p) formed in the dissociation of such aligned H_2^+, as measured from a time-averaged polarization, will be aligned parallel or perpendicular to the beam axis. However, there is a plane of symmetry swept out by R, the center-of-mass to center-of-mass distance from the molecule to the target atom. Two of the infinitely possible planes are shown in Fig. 3.5. Because of the finite size of the detector, many such planes contribute to the observed process. Since the molecule is parallel to the beam axis, every symmetry plane intersects along the beam axis. This shows that there is cylindrical symmetry about the beam axis. One can then show that the Hamiltonian is a constant of the motion for reflections about each plane.

Consider the case when the symmetry plane is coincident with a particular xz-plane as shown in Fig. 3.5a. Using the geometry shown in Fig. 3.6, the Hamiltonian for the system is written as

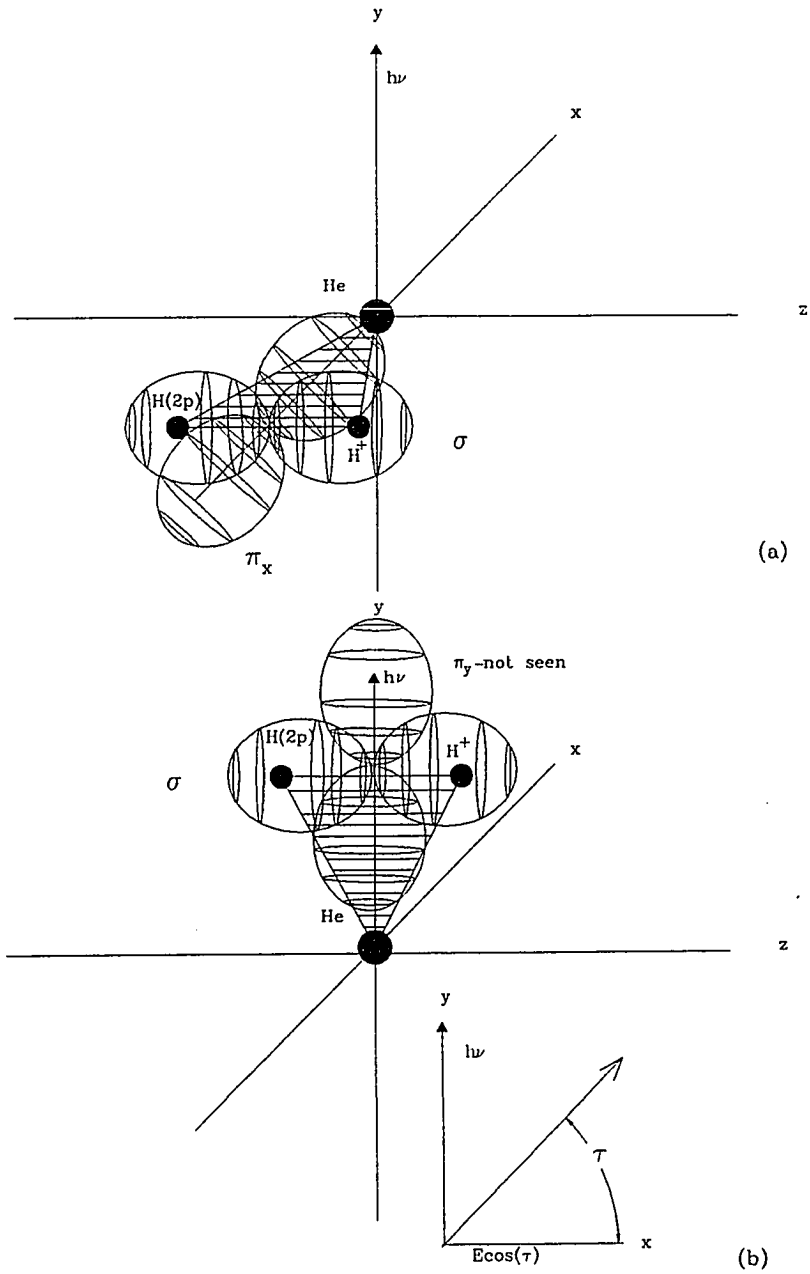

Figure 3.5: Illustration of symmetry planes when the molecule is oriented parallel to the incident beam velocity. Note that the full contribution of π_x–states ($2p_x$ states of the atom in the lab frame) are only seen when the plane of symmetry is parallel to the xz–plane. This is shown in (a). In (b), no π_x–states contribute to the observed process. In the configuration shown in (b), π_y–states are also possible. However, only a very small amount can be seen with the present experimental apparatus (see text). The inset in (b) shows a case when the symmetry plane is at an arbitrary angle (as viewed from the z–axis).

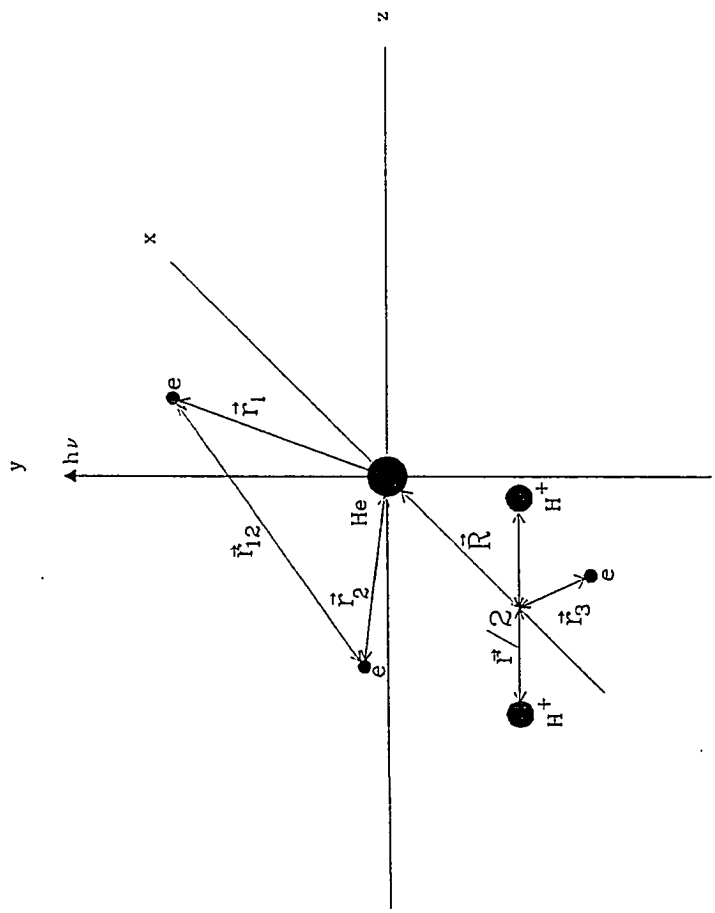

Figure 3.6: Geometry of the atom–molecule system when the molecule is oriented along the beam axis.

$$H = H_{KE} + \frac{1}{|\vec{R}+\frac{\vec{r}}{2}|} + \frac{1}{|\vec{R}-\frac{\vec{r}}{2}|} - \frac{1}{|\vec{r}_1|} - \frac{1}{|\vec{r}_2|} - \frac{1}{|\vec{R}+\vec{r}_3|} + \frac{1}{|\vec{r}_1-\vec{r}_2|} - \frac{1}{|\vec{R}+\frac{\vec{r}}{2}-\vec{r}_2|} + \frac{1}{|\vec{r}|} - \frac{1}{|\vec{R}-\frac{\vec{r}}{2}-\vec{r}_2|} + \frac{1}{|\vec{R}+\vec{r}_3-\vec{r}_2|} - \frac{1}{|\vec{R}-\frac{\vec{r}}{2}-\vec{r}_1|} - \frac{1}{|\vec{R}+\frac{\vec{r}}{2}-\vec{r}_1|} + \frac{1}{|\vec{R}+\vec{r}_3-\vec{r}_1|} - \frac{1}{|\vec{r}_3-\frac{\vec{r}}{2}|} \frac{1}{|\vec{r}_3+\frac{\vec{r}}{2}|}, \quad (3.8)$$

where H_{KE} represents the kinetic energy terms in the Hamiltonian. If this Hamiltonian is transformed via y→-y, one can easily show that equation (3.8) remains invariant under this transformation. Since all the planes of symmetry for this particular molecular orientation intersect along the z-axis, each symmetry plane can be replicated by rotating about the z-axis, the symmetry plane which is coincident with the xz-plane. As an example, Fig. 3.5(b) shows the symmetry plane of Fig. 3.5(a) rotated by 90° about the z-axis. If one denotes the rotated frame in terms of x', y' and z', then y'→-y' transformations of the Hamiltonian must be considered (in Fig 3.5a, a 90° rotation of the symmetry plane yielding Fig 3.5b would mean x→y', y→-x', and z'→z). Since the primed and unprimed coordinates are easily related by a rotation matrix, where the rotation angle is denoted by the dihedral angle τ formed by the xz-plane and the plane of symmetry itself, the Hamiltonian in the primed system can be easily expressed in terms of the unprimed system. Again, one can easily show that under y'→-y' transformations, the Hamiltonian remains unchanged. If the operator which transforms y'→-y' is denoted by

ϑ, then

$$[\hat{\vartheta}, H] = 0 . \qquad (3.9)$$

In many atom-atom or electron-atom collisions, the Hamiltonian has positive reflection symmetry about the scattering plane (see Sect. B.1); thus, states which do not have this reflection symmetry cannot be excited. Similarly, the present case suggests that excited states of negative reflection symmetry are not allowed. When the symmetry plane is parallel to the yz-plane (Fig. 3.5b) π_y and σ-states can be excited. However, since the photon detector is along the y-axis, π_y-states are not detected (in reality a very small amount of π_y can be detected due to fine structure), since one cannot detect radiation along the axis of the radiating dipole.

When the symmetry plane is parallel to the xz-plane (Fig 3.5a), then π_x and σ-states can be excited. As the symmetry plane rotates from the case where it is parallel to the yz-plane to the xz-plane, the contributions from the π_y-states (not seen) decrease while the contributions from the π_x-states increase, with ubiquitous contributions from σ-states. Since the all the reflection planes imply major contributions from σ-states, one can postulate that σ-states will always have larger contributions than π-states for the observed process. Thus, the charge cloud of the will in general be aligned along the beam axis. Although this symmetry argument shows that the nascent charge cloud of H(2p) should be aligned parallel to the initial beam axis, predictions of the relative contributions of the excited H_2^+ states require a comprehensive theoretical investigation which highlights the collision dynamics for the process.

If the instantaneous orientation of the H_2^+ molecule is perpendicular to the incident beam direction (see Fig. 3.7a and b), only two types of planes of reflection symmetry exist; one set is coincident with the xz-plane and the other is coincident with the yz-plane. If the plane of symmetry is parallel to the xz-plane (Fig. 3.7a), σ and π_x states contribute to the observed process. On the other hand, if the plane of symmetry is parallel to the yz-plane (Fig 3.7b), then π_x and π_y (not seen) contribute to the observed process. When the center-of-mass to center-of-mass distance from the molecule to the target atom R is neither parallel or perpendicular to the z or y-axis, no planes of symmetry exist. Predictions of the orientation of the charge cloud require a more rigorous analysis. In the present case, one can only say that the charge cloud will most likely only be parallel or perpendicular to the initial beam velocity, since neither the initial state nor the final state is pure. In the more general case where the instantaneous orientation of the H_2^+ molecule is ϕ, no planes of symmetry as described above exist. Again, one can only say that the nascent charge cloud is oriented parallel or perpendicular to the beam direction.

Since the above arguments show suggest P_1 will be the only non-zero Stokes' parameter, one can express the intensity of the emitted light as

$$I(\alpha, 0^o, 0^o) = \frac{I}{2}[1+P_1\cos 2\alpha] \qquad (3.10a)$$
$$= A+B\sin^2\alpha,$$

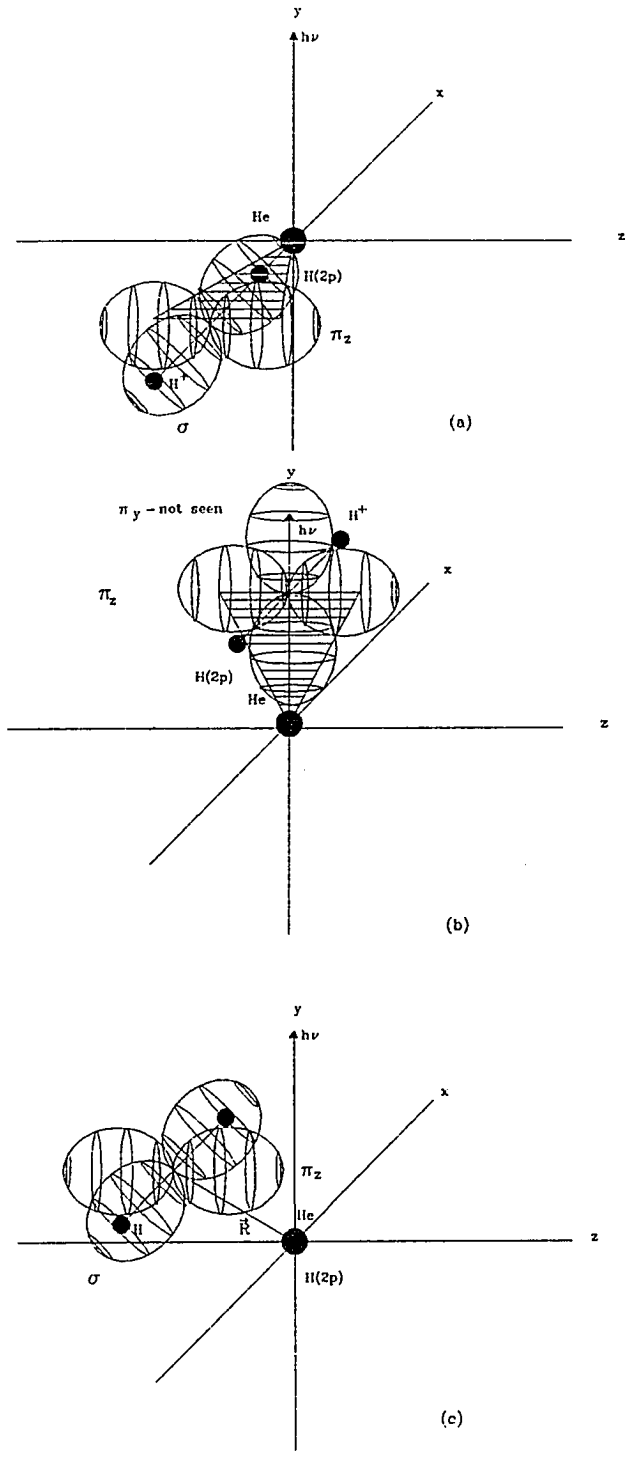

Figure 3.7: Illustration of the only two possible symmetry planes when the molecule is oriented perpendicular to the incident beam velocity. Note that the full contribution from σ-states ($2p_x$ states of the atom in the lab frame) are only seen when the plane of symmetry is parallel to the xz-plane. This is shown in (a). In (b), no σ-states contribute to the observed process. In the configuration shown in (b), π_y-states are also possible. However, only a very small contribution is seen with the present experimental apparatus (see text). In (c), no symmetry plane is swept out by $\vec{R}$.

where

$$P_1 = -\frac{B}{2A+B}. \qquad (3.10b)$$

The values of A and B are parameters which fit the data to the expected shape of the polarization pattern.

Since Montgomery (1982) studied coherent excitation of H_2, the results of this experiment cannot be expressed in terms of molecular excitation amplitudes. Consequently, the results of this work will be analyzed from a different point of view.

3C.2 EXTRACTION OF INFORMATION FROM H(2P) PRODUCTION

In the work of Fano and Macek (1973), the alignment and orientation parameters were introduced. These quantities hav helped many experimentalists identify excited magnetic substates from their polarization measurements (Anderson *et al* 1988). However, the alignment and orientation parameters of Fano and Macek (1973) do not take into account partially or totally incoherent processes. On the other hand, Blum and Kleinpoppen (1979) extended the results of Fano and Macek (1973) with a density matrix formalism (this accounts for states which are not pure; see Sect. 3B.2) to obtain the so called "integral alignment parameter"

$$A_{20} = \frac{6P_1}{P_1-3}. \qquad (3.11)$$

In terms of the magnetic substates this can be expressed as (Blum and Kleinpoppen 1979)

$$A_{20} = \frac{\sigma_0 - \sigma_1}{\sigma_0 + 2\sigma_1}, \qquad (3.12)$$

where σ_0 and σ_1 $(=\sigma_{-1})$ are the total cross sections for excitation into the $H(2p_0)$ and $H(2p_{\pm 1})$, respectively. It should be reiterated that A_{20} directly yields the total average alignment of the charge cloud of the excited atom averaged over all collisions. It is not necessarily true that this quantity yields the alignment of the charge cloud of the excited molecule (see Ch. 6).

Using equations (3.11) and (3.12) the ratio σ_0/σ_1 (atomic states) is determined by the expression

$$\frac{\sigma_0}{\sigma_1} = -\frac{11P_1+3}{7P_1+3} = \frac{3A-4B}{3A+5B}. \qquad (3.13)$$

This ratio yields qualitative information as to which molecular states dominate the excitation process. Depolarization effects due to fine-structure interaction are taken into account in this expression.

Since the quantization axis is the internuclear axis of the molecule, A_{20}, and P_1 must be written in the molecular frame. When the molecule is oriented at an angle ϕ relative to the beam axis, the ratio σ_0/σ_1 becomes

$$\frac{\sigma_0}{\sigma_1} = -\frac{11B\cos(2\phi) - 22\sqrt{A(A+B)}\sin(2\phi) + 3(2A+B)}{7B\cos(2\phi) - 14\sqrt{A(A+B)}\sin(2\phi) + 3(2A+B)} \quad (3.14)$$

The derivation of equation (3.12) is presented in Appendix D.

Due to the finite size of detectors, the orientation of the internuclear axis of the molecule is determined within $\Delta\phi$ relative to the incident projectile velocity. Since the internuclear axis acts as the quantization axis, it would seem that a smearing out of the polarization pattern will result. The resultant pattern is an incoherent sum (average) of intensities over all acceptable internuclear orientations $\pm\Delta\phi$. Compensation for this effect is difficult because one needs to know how the charge cloud varies over the acceptable internuclear orientations. Thus, one must limit as much as possible $\Delta\phi$ such that coincidences are still measurable within a reasonable time frame. Also, because the center-of-mass deflection is not determined in the present experiment, compensations due to this depolarization effect are impossible to consider. However, since it is assumed that the center-of-mass deflection is very small (see Appendix E), one can infer that this effect is very small.

CHAPTER 4

EXPERIMENTAL APPARATUS

4A. GENERAL DESCRIPTION

Fig. 4.1 shows a cross-sectional view of the experimental apparatus. A beam of charged particles is produced in a duoplasmatron source. Once extracted and accelerated, the particle beam is focused by an einzel lens system. H_2^+ ions are finally selected as the charged particle beam passes a momentum analyzer (analyzing magnet). Collimating apertures and two sets each of vertical and horizontal deflection plates further narrow the H_2^+ beam as it is directed towards a static cell. Details of the defining slits, deflection plates, and momentum analyzer are presented elsewhere (Martin 1975).

The differentially pumped static cell is the interaction region where the target gas is introduced via a stainless steel tube. Perpendicular to the collision plane (see Sect. 4C.1 for its definition), a L_α Brewster angle polarizer measures the linear polarization of the excited 2p state of H-atoms produced from the dissociation of H_2^+. Dimensional details of the static cell and photon detection system are presented in Appendix A.

Scattered protons are energy analyzed by a two stage parallel-plate analyzer (Calabrese *et al* 1993 and Wiese 1993). Proton signals are obtained by discrete anode

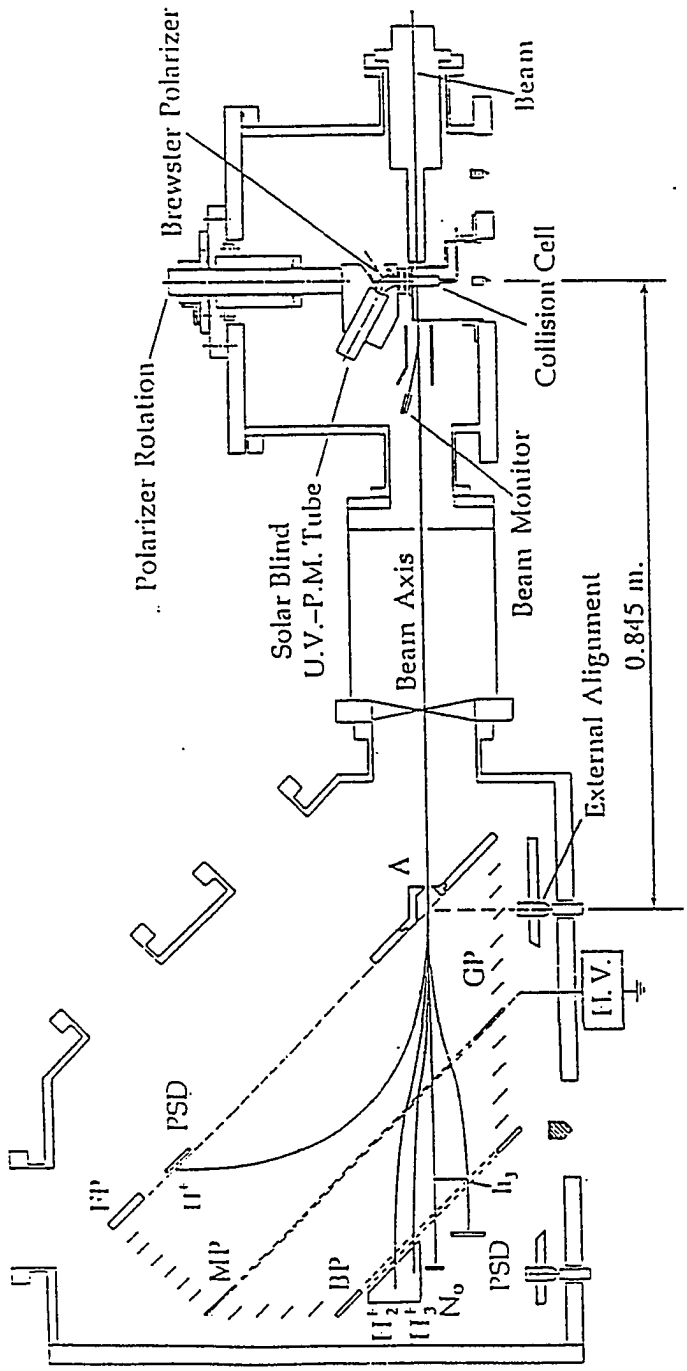

Figure 4.1: Cross sectional view of experimental apparatus; refer to text for details.

position sensitive detector consisting of microchannel plates (MCPs). Pulses from the MCPs are detected in delayed coincidence with pulses from the photomultiplier.

In the following sections of the chapter the details of the photon detection system, analyzer, and proton detector system will be discussed.

4B. COLLISION CHAMBER

The stainless steel chamber consists of three major elements: a collision cell (D of Fig. 4.2), a beam monitoring system (F and G of Fig. 4.2), and a photon detection system (H of Fig.4.2). High vacuum is achieved with three pumps: a diffusion pump for the static cell; and a diffusion and turbo-molecular pump for the rest of the chamber. Base pressures of 3.8×10^{-8} torr have been achieved.

4B.1 COLLISION CELL

As mentioned above the target gas is formed inside the differentially pumped collision cell (D). It is formed by a gas tube (0.125 in. o.d.) which is centered on the photon rotation axis and the H_2^+ beam axis. The intersection of the target axis, beam axis, and photon detection system rotation axis forms the collision center.

The diameter of the collision cell is 0.625 in. The beam enters the collision cell housing (refer to Fig.4.2 and Appendix A) through a circular aperture of 0.031 in., scatters in the static cell, and exits through a slit 0.580 in. wide. This allows for the detection of an angular spread of 7° for the dissociating exiting beam. Epoxied atop the static cell is a 1.00 in. diameter by 0.078 in. (2 mm) thick LiF crystal. It serves two purposes. First, it provides the seal for the differentially pumped region. Second, since LiF transmits a high percentage of vacuum ultraviolet radiation (Englehard Co.

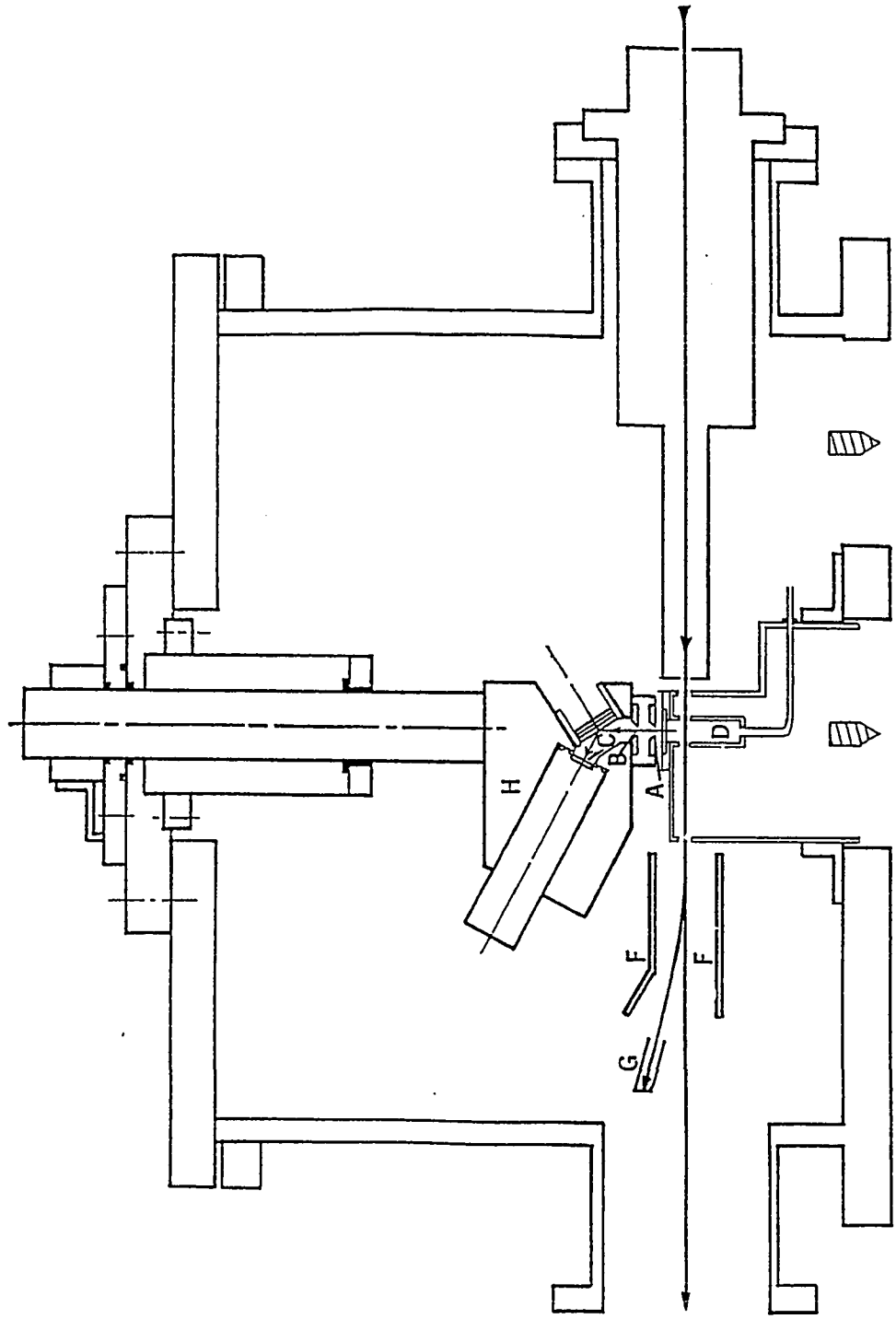

Figure 4.2: Close up view of collision chamber; refer to text for details.

guarantees at least 50% transmittance for crystals 2 mm thick), it lets light emitted from the excited 2p state of H pass through to the photon detection system.

4B.2 BEAM MONITORING SYSTEM

To monitor the ion beam current, a pair of deflector plates and a Faraday cup were installed (refer to F and G in Fig. 4.2 and Appendix A). The deflector plates (F) are separated by 1.375 in. Their lengths are 3.625 in. In between the deflector plates, a field straightening plate has been placed to keep the field uniform. The resistors which electrically connect this plate to the deflector plates keep the current flow below the power supply limit.

Potentials up to 2000 volts on one plate and -2000 volts on the other are supplied by a pair of Bertan power supplies. Because of the maximum potential difference of 4000 volts, ion beam currents are measurable for particle energies up to 15 KeV. One can approximate the distance that the particles are bent above or below the beam line with the equation

$$y = \frac{qV_{plates}}{4E_p}\frac{x_0^2}{d}, \qquad (4.1)$$

where V_{plates} is the potential difference between the plates; E_p, the energy of the incoming particle; d, the distance between the plates; x_0 the length of the plates; q, the charge of particle. Equation (4.1) was derived by elementary application of freshman physics to a pair of parallel plates. An exact solution of the trajectories for this particular plate

geometry was not possible due to the non-trivial nature of the coupled equations of motion. Equation (4.1) was used for design purposes only, since it overestimates y as a function of the plate voltage.

The Faraday cup (G) consists of three cylindrical electrodes. The outermost is grounded. This acts as a shield for the other two cups. Its length and diameter are 1.10 in. and 0.400 in., respectively. This short length is due to the limited available space inside the collision chamber. The inner two cups, however, are biased by a 67 volt battery. This is done to minimize the loss of secondary electron emission. All signal leads from the Faraday cup to the feedthrough flange are properly shielded.

To test the Faraday cup system, a beam of 4.0 keV H_3^+ was monitored for various plate voltages and cup bias voltages. The results are shown in Fig. 4.3. The proper operating conditions occur in the plateau regions of both graphs. In the present case of a 4.0 keV beam, a 950 V potential difference between the deflector plates and 67 V bias between the cups will suffice in sweeping the beam into the Faraday cup. Note that the plateau region begins near 900 V. This is near the calculated value of 840 V for a beam deflection of y=0.50".

4B.3 PHOTON DETECTOR SYSTEM

To improve the photon detection efficiency, moreover, to reduce data collection time, a new L_α photon detection system was built. This is shown as (H) in Fig. 4.2 (refer also to Appendix A). The crux of the apparatus consists of a pile of four 0.5 mm thick LiF crystals at Brewster's angle (58.6°), and an EMR photomultiplier tube with a quantum efficiency of 22.5%. All of the crystals are contained within a specially made

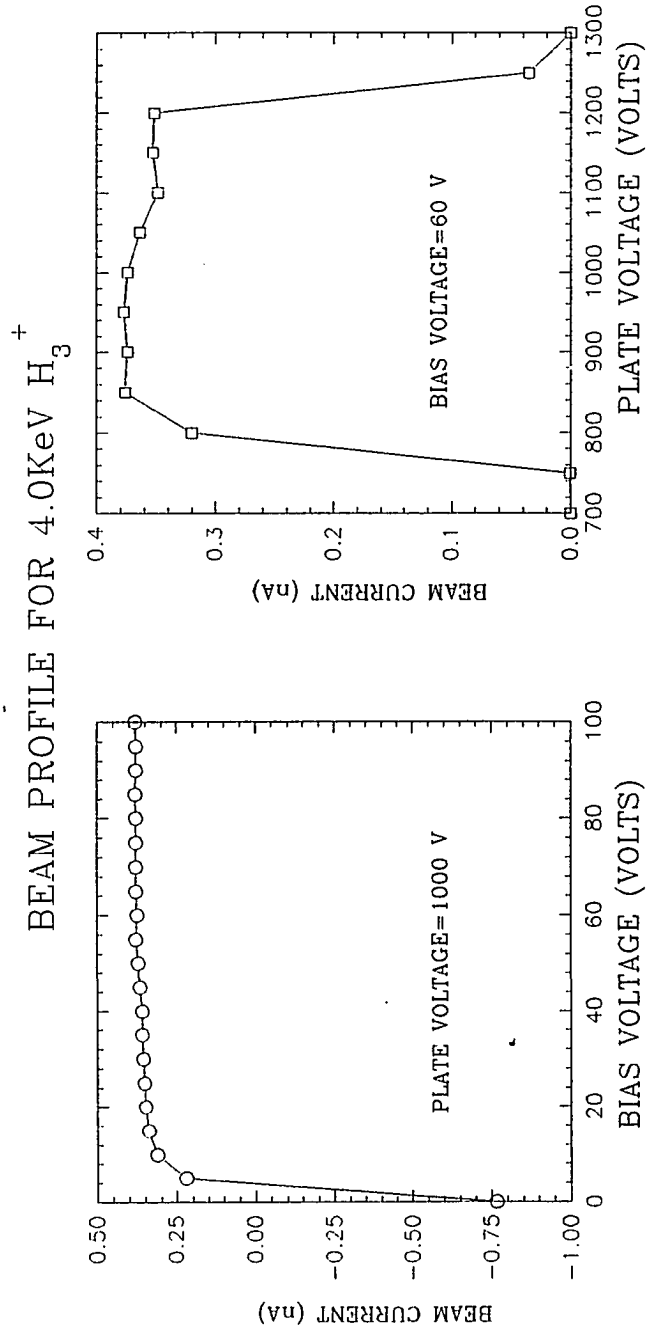

Figure 4.3: Faraday cup data

holder. Furthermore, the LiF holder, photomultiplier, and aperture holders are placed in or mounted to a machined aluminum block. The block is fastened to a stainless steel shaft which feeds through the chamber top. This shaft forms the polarizer rotation axis. A particular polarizer angle is chosen by manually rotating the system at the top of the collision chamber. Because of the double o-ring vacuum seal arrangement, care must be taken when rotating the system.

The basic design of the system is similar to that described by Mueller (1982), which used two 2 mm LiF crystals, except that: (1) the quantum efficiency of the new photomultiplier is greater by a factor of 3.20; (2) The calculated reflectance of the four 0.5 mm crystals (0.515) is greater by a factor of 2; and (3) the new vernier system on the chamber top enables one to read each polarization angle more easily. Points (1) and (2) are important because if one wants to increase coincidence rates, the detector efficiency and solid angle must also increase. Appendix A lists all the essential dimensions of the system. It should be noted that Mueller's system was used for the data presented in Section B.1 of chapter 6.

4B.3a DESIGN CRITERIA

An essential feature in designing a detection system is efficiency. In the present case one must consider the difficulties in detecting VUV radiation. Very few materials exist which are highly transparent to VUV. The best candidates are LiF and MgF_2. Although both crystals can serve equally well as Brewster angle polarizers, MgF_2 has an imaginary component of the refractive index k of 0.45 (Samson 1967); while LiF value is nearly transparent at photon energies below 11.8 eV (Kato 1961) with k of the order

of 10^{-6} (Palik 1985). A knowledge of k is important since the complex component of the refractive index leads to rapid absorption of the incident radiation and loss of transparency (opacity) of the material. The imaginary component of the index of refraction also inhibits the parallel component of the reflectance from attaining a value of zero at any angle of incidence (Hecht and Zajac 1979). This cannot occur if one is designing a Brewster angle polarizer. Therefore, LiF was chosen for the present experiment.

To properly calculate the reflectivity of a stack of nearly transparent crystals one must take into account multiple reflections, and loss of intensity due to scattering *etc.* This calculation was performed by Stokes (1862). The quantities which are needed for this calculation are: the absorption coefficient, the index of refraction (1.64), and the angle of incidence (about 58° 37'). The first quantity has been measured under a variety of conditions.

It has been shown by Schneider (1936) that the absorption coefficient, μ, for LiF varies significantly from crystal to crystal even though different slices of the same crystal show little variation. Impurities, poor polish, and layers of foreign material may all contribute to the reduction of transmission through the crystal. He measured μ to be 0.14/mm. If the crystal is grown in air, μ can be as high as 0.6/mm. Thus the value of the absorption coefficient will only be an approximation. The value of μ that is used is obtained from the measured transmittance of 70 percent at 121.6nm, at normal incidence, of Laufer *et.al.* (1965) at 26°C. The absorption coefficient is extracted from the equation $I=I_o e^{-\mu d}$, where d is the thickness of the crystal. This gives a value $\mu=0.23$/mm.

The results of the calculation for various numbers of plates are shown in Figs.

4.4-4.9. Its details are presented in Appendix B. Figures 4.4-4.7 show the reflectivties for various number of plates. One can easily notice that the degree of polarization curve becomes narrower as the number of plates increases. Thus, in order to keep the parallel component of the reflected light near zero, the angular acceptance of the incident light reaching the detection system must decrease as the number of plates increases. For, example, if one makes the very crude assumption that all the acceptable angles (the present system accepts an angular spread of $\pm 9.10^{o}$; note that this value vas chosen because it minimizes unwanted reflections off the walls of the machined aluminum block) of incidence are equally probable, one can show that the average polarization (averaged over all angles of incidence) for a pile of 4 plates is 90.9 percent. If one plate is used, the average polarization increases to 94.1 percent. In order to obtain the same average polarization with one plate, the angular acceptance must be about $\pm 13.2^{o}$. Therefore, a Brewster angle polarizer requires an optimization in the number of plates in the pile and in the detector solid angle. The polarizer also requires a minimization of unwanted reflections off the walls of the apparatus itself.

Finally, figures 4.8 and 4.9 show the affect of absorption on both $R_{\perp}$ and $R_{\parallel}$ as the number of plates in the pile increases.

4B.3b PHOTON DETECTOR ELECTRONICS

Although the details of the electronics are similar to those of Mueller (1982), the general features will be discussed to familiarize the reader with the signal processing. Fig. 4.10 shows photon detector electronics. The photomultiplier signal is fed into

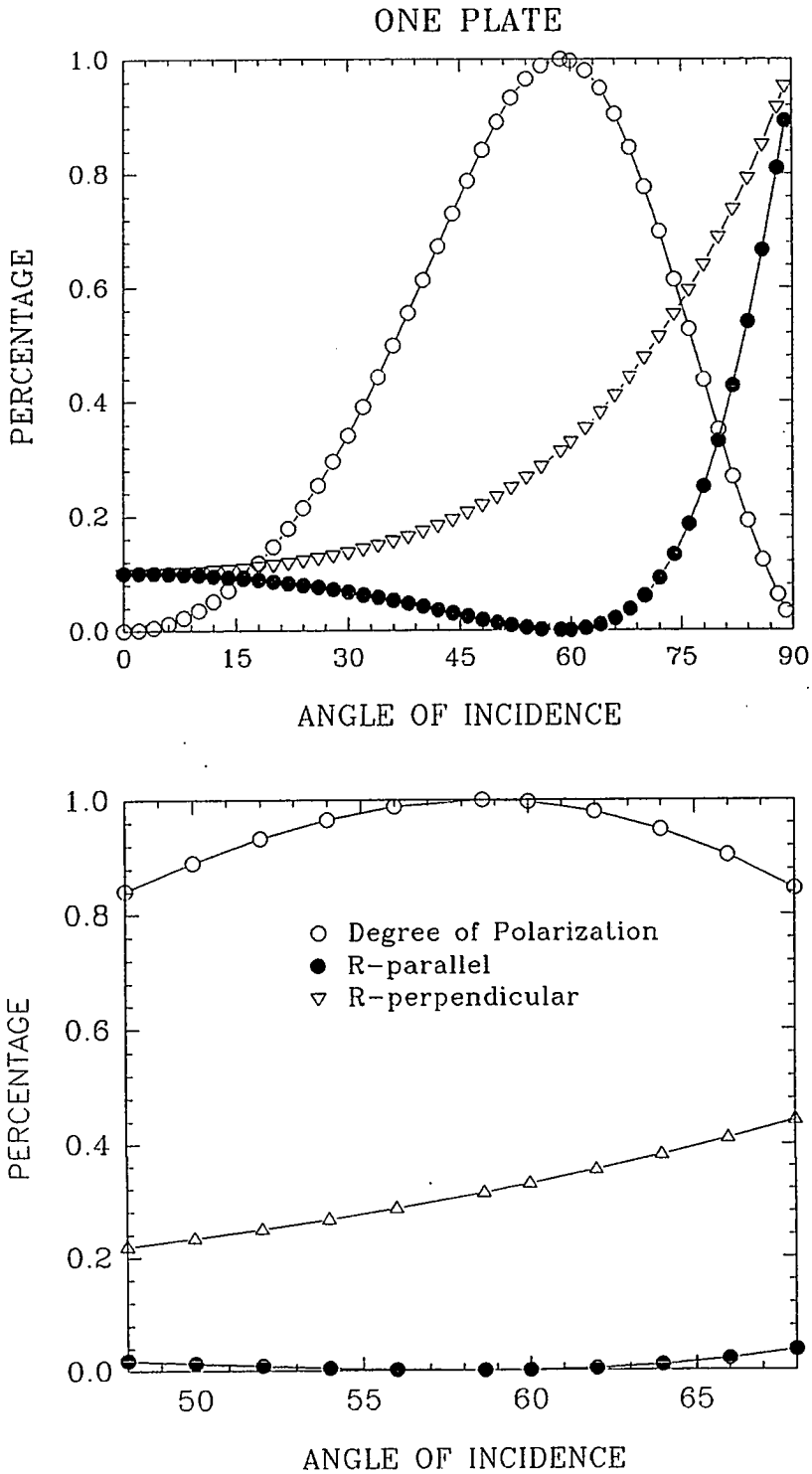

Figure 4.4; Reflectivity for one plate with absorption. The second plot shows the behavior of the curves near Brewster's angle. The legends are the same in both plots.

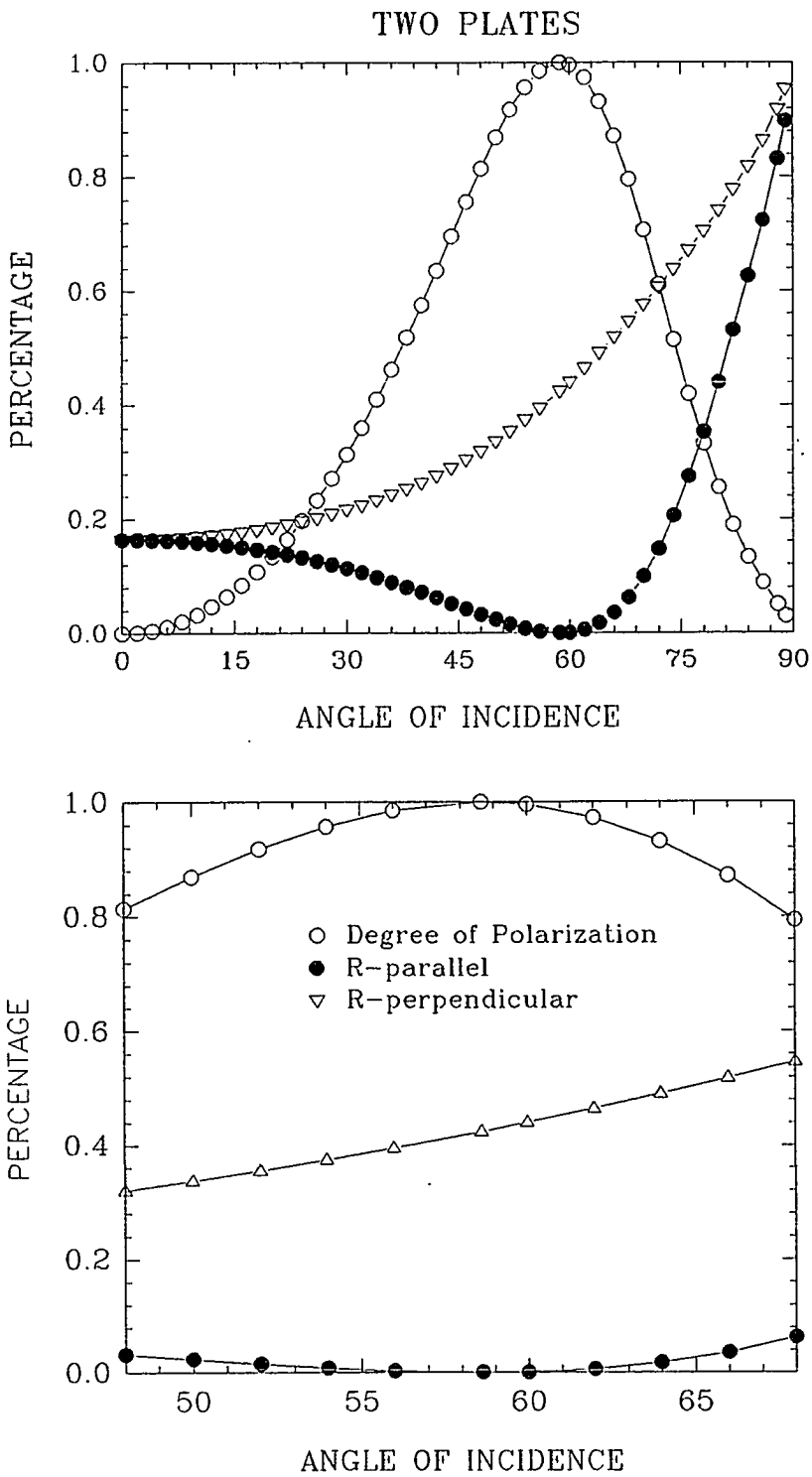

Figure 4.5; Reflectivity for two plates with absorption. The second plot shows the behavior of the curves near Brewster's angle. The legends are the same in both plots.

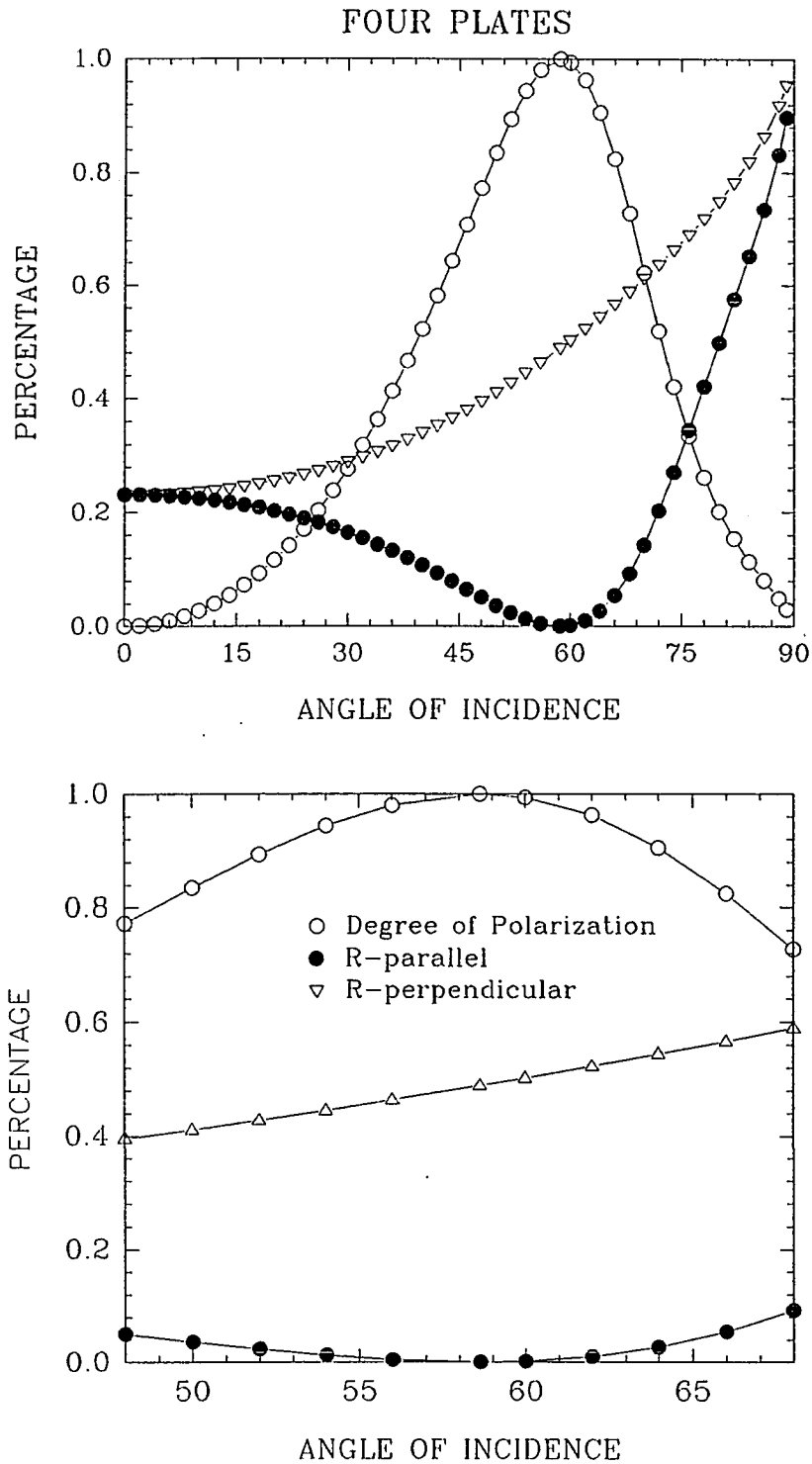

Figure 4.6; Reflectivity for four plates with absorption. The second plot shows the behavior of the curves near Brewster's angle. The legends are the same in both plots.

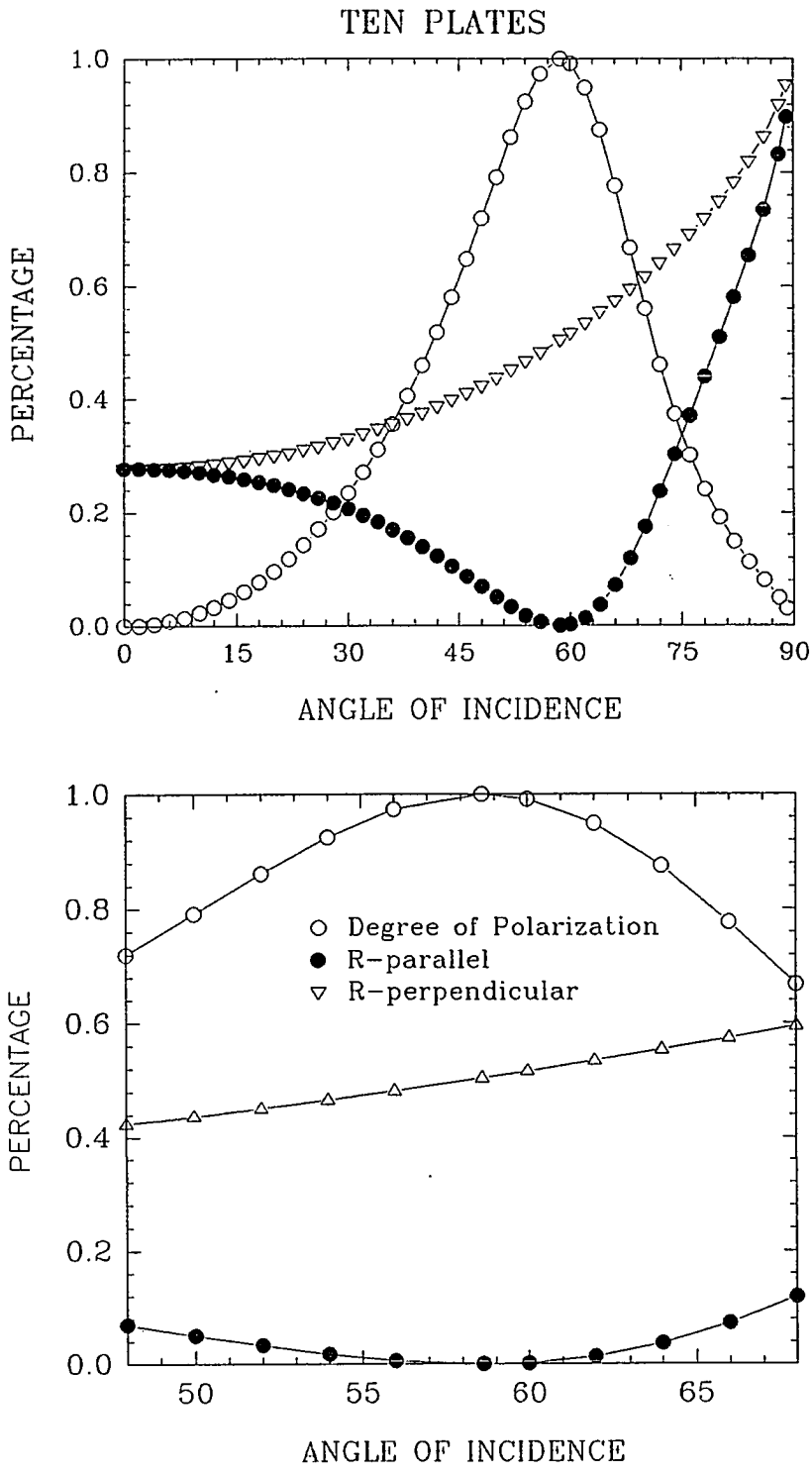

Figure 4.7; Reflectivity for ten plates with absorption. The second plot shows the behavior of the curves near Brewster's angle. The legends are the same in both plots.

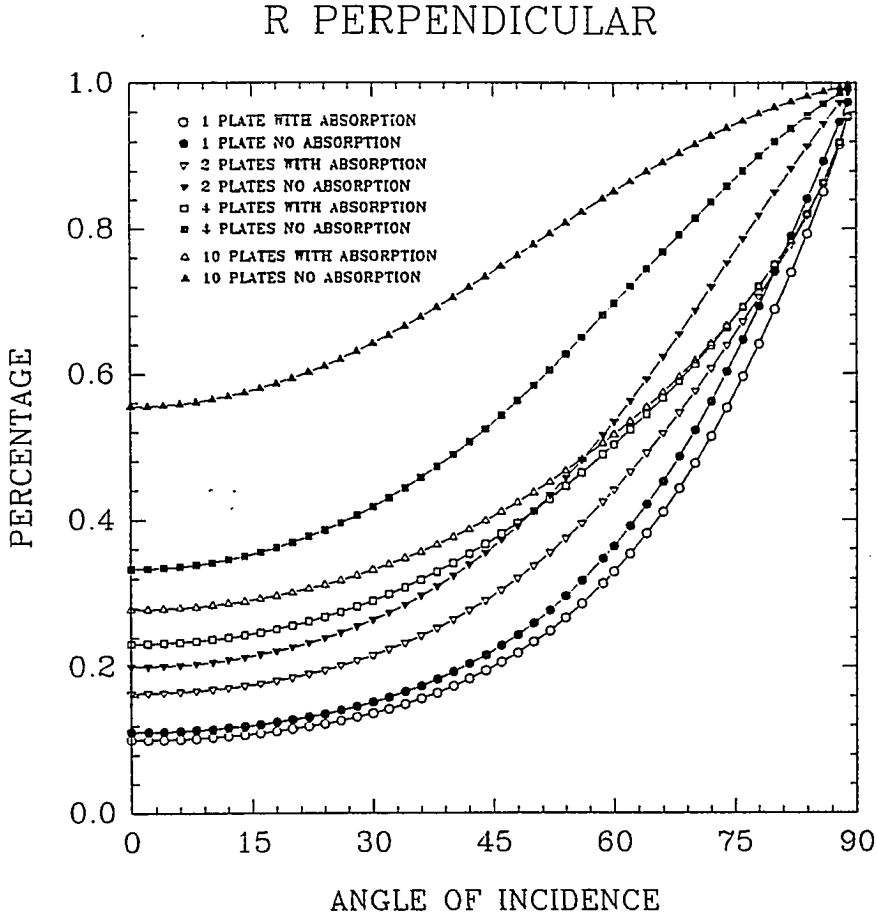

Figure 4.8: Comparisons of reflectivity perpendicular to the plane of incidence.

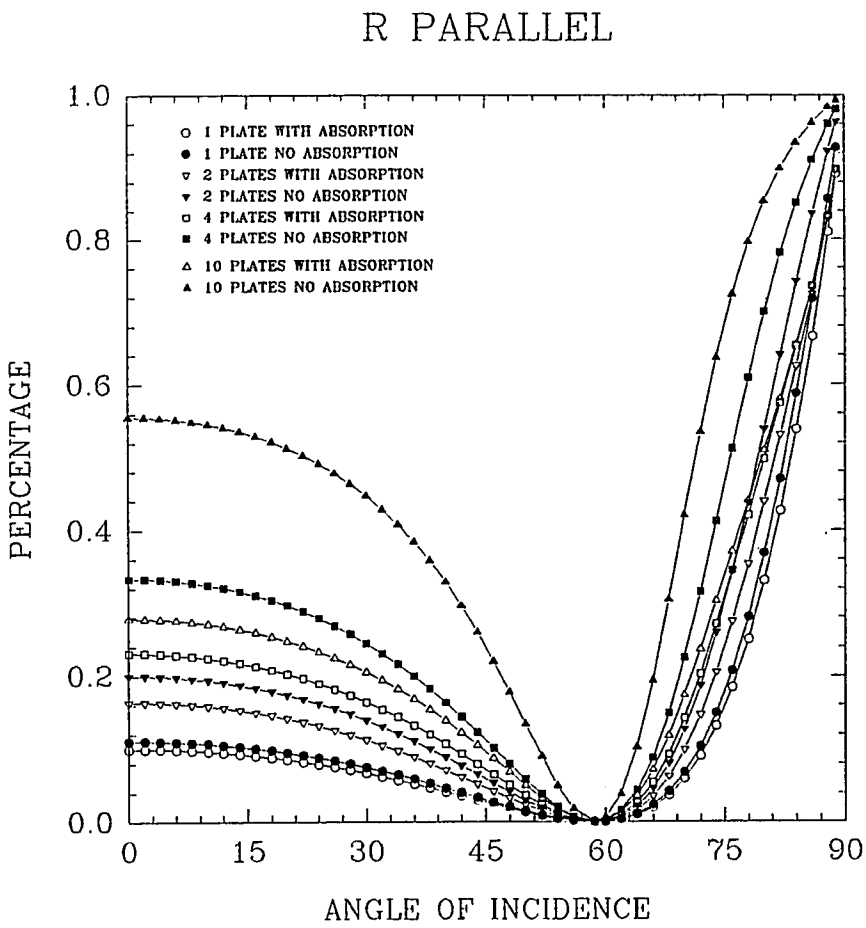

Figure 4.9: Comparisons of reflectivity parallel to the plane of incidence.

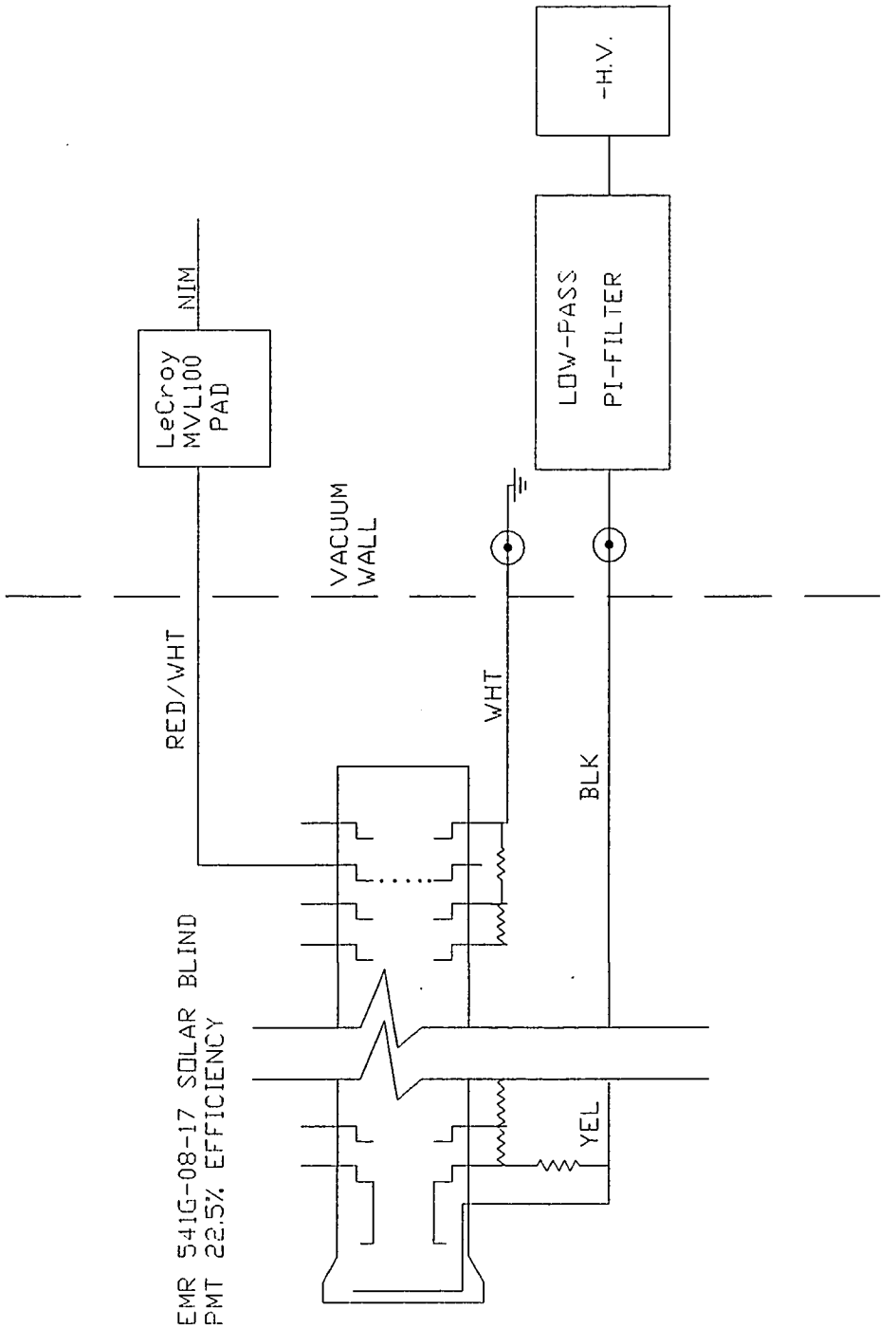

Figure 4.10: Photon detector electronics; power supply voltage=-3000V.

LeCroy MVL100TB preamplifier discriminator whose output is NIM. Good shielding and grounding techniques insure low noise signals. Furthermore, filtering of the photomultiplier's power supply reduced line noise to a minimal level. Dark counts are less than 0.8 Hz.

4B.3c ALIGNMENT OF THE PHOTON DETECTOR

With the propagation vector of the electromagnetic radiation perpendicular to the scattering plane, the two polarization vectors are in the scattering plane. Therefore, it is very important to align the photon detection system with one of the electric vectors. One choice is along the beam axis and the other, of course, 90° to the beam.

The photon detector system was first aligned along the beam axis by eye. Of course, the method is very crude, and a better method must be implemented.

The second method of alignment has been described in detail elsewhere (Wedding *et al* 1991). Briefly, one measures the uncorrelated photons produced in $A+B \rightarrow A^*+B$ as a function of polarization angle. Equation (3.2) applies with $P_2=0$, due to cylindrical symmetry.

Two measurements were performed. In the first case, the process $H^+ + Xe \rightarrow H(2p) + Xe^+$ was examined for 5.5 keV H^+. The polarization plot is shown in Fig. 4.11 in both polar and Cartesian coordinates. The quantity β describes the angular displacement of the polarization axis from the beam axis. Because Xe and Xe^+ have many lines in VUV, another measurement was performed for verification. This time the process $H^+ + Ar \rightarrow H(2p) + Ar^+$ was examined for 5.5 keV protons. In this case Teubner *et al* (1970) showed that the linear polarization P_1 is near zero. The results are shown in

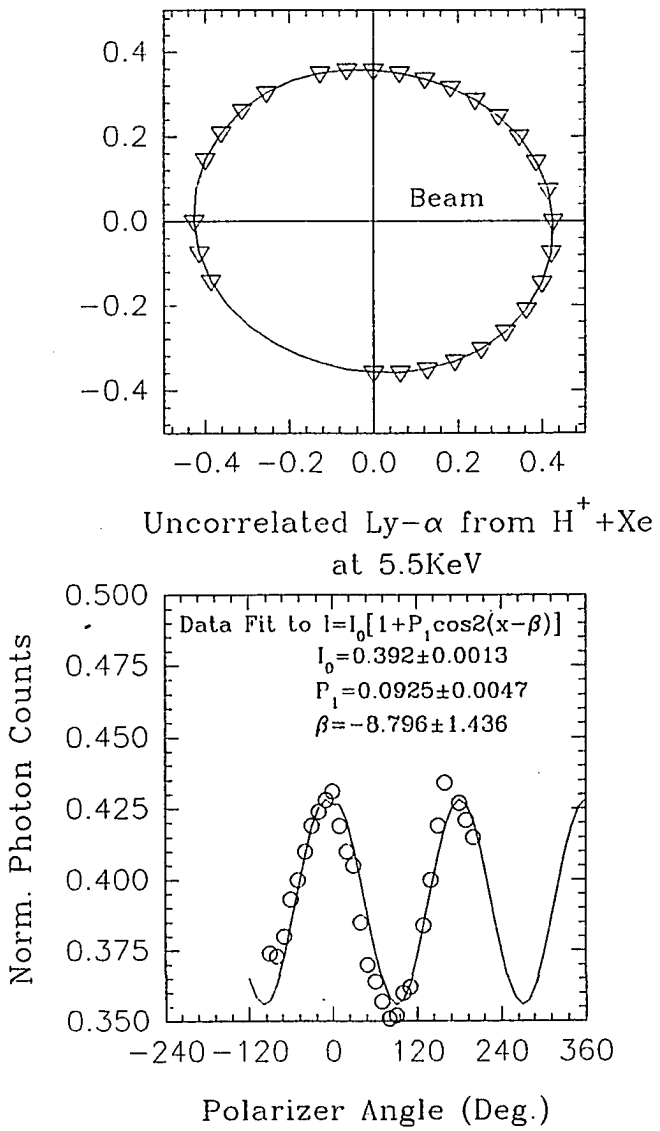

Figure 4.11: H^++Xe−H(2p)+Xe^+ alignment data

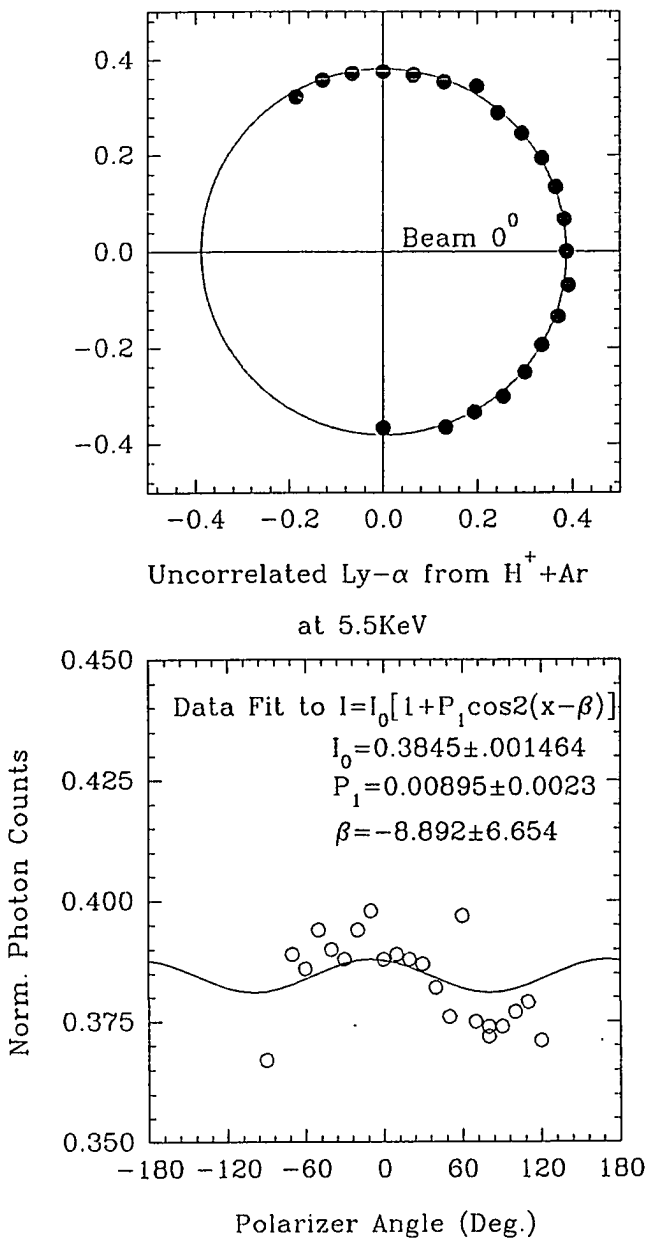

Figure 4.12: H^++Ar−H(2p)+Ar^+ alignment data

Fig. 4.12. The present measurement of P_1 agrees very well with the Teubner *et al* (1970) measurement. Also, β agrees very well with the first measurement.

4C. ION ENERGY ANALYZER

The proton energy analyzer consists of three parallel plates at 45° with respect to the incident beam. This is shown in Fig. 4.1. The mid plate is at a high positive potential. The front and back plates are at ground potential. The system has the capability of measuring particles with high resolution over a variety of laboratory angles and energies. This allows analysis of several particles in coincidence from the same collision. Details pertinent to the present experiment will be presented. For further details of the system see Calabrese *et al* (1993).

4C.1. DESCRIPTION OF THE ENERGY ANALYZER

The entire analyzer, which is shielded from magnetic fields by Conetics μ-metal, rests on three alignment pins placed at the base of its stainless steel chamber (refer to Fig. 4.1). This enables one to level and align the analyzer relative to the initial ion beam. Five vacuum sealed screw mechanisms outside the chamber are used for alignment when the system is under vacuum. The front pin is fixed directly below the front plate slit opening, and permits adjustments in the vertical direction. The two back pins allow the motion in the horizontal and vertical directions with the front pin as the pivot. Provisions have been made so that the analyzer may be removed and reinstalled without disturbing its alignment with respect to the initial ion beam.

The defining entrance slit on the front plate has a width (the dimension perpendicular to the plane of Fig. 4.1) of 10.375 in. The slit opening, defined by the

vertical distance A in Fig. 4.1 (in the plane of Fig. 4.1 and perpendicular to the beam axis), is adjustable and currently set at 0.0558 ± 0.0001 in. As measured from the center of our collision cell, the width is large enough to accept particles scattered as much as 5° in the laboratory frame. The scattering plane is defined by the triangle formed by the collision center and the line bisecting the slit opening horizontally. In Fig. 4.13 this is shown as the plane RPV.

The front plate of the analyzer has dimensions 20.500 in. x 12.000 in. on which one can place several detectors. Because the area is large, several detectors can be used to simultaneously measure several particle energies and scattering angles, relative to the collision center. The large area also allows for easy repositioning of the detectors.

The mid plate, which is 6.997 in. behind the analyzer front, consists mostly of a 96% transmission wire mesh (see dashed line in Fig. 4.1). The mesh is hand wound in only one direction, parallel to the projection of the initial beam direction onto the plate, with 0.005 in. diameter wire. The wires are spaced 0.25 in. apart. The mesh helps keep the field uniform while allowing particles to pass through the mid plate and reach their respective detectors. In addition, its small size minimizes the possibility of particles hitting it and scattering into the detectors on the front plate.

For a primary H_3^+ beam and a suitable positive voltage on the mid plate, protons are deflected away from the beam toward the front plate; particles such as H and H_2 (shown as neutrals N_0 in Fig. 4.1), H_2^+, H_3^+, and H^- reach their detectors behind the back plate. Therefore, it is possible to measure the energy distributions of several dissociation fragments of various charges and masses at one time.

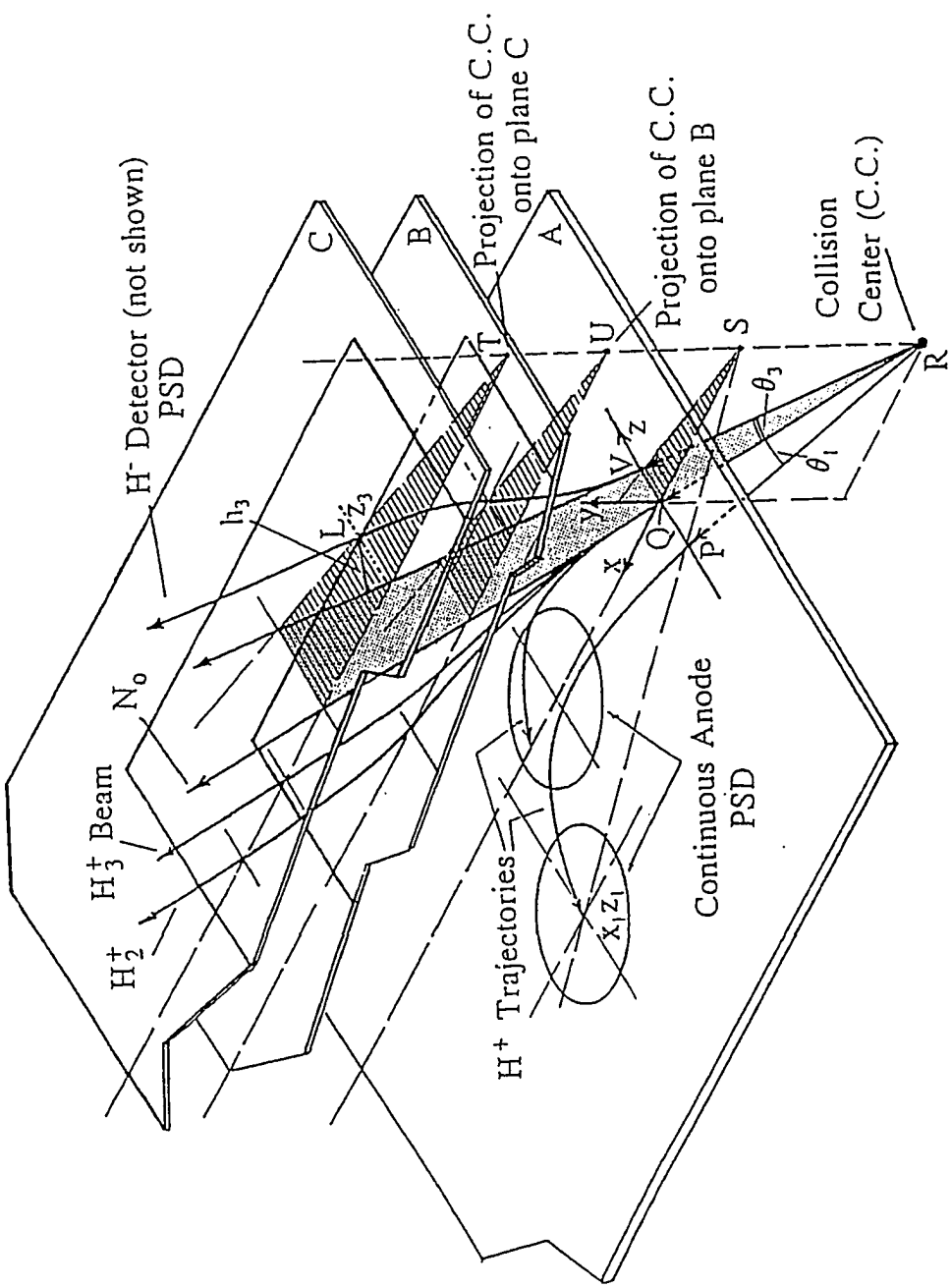

Figure 4.13: Analyzer geometry

In between each stage of the analyzer, 0.0625 in. thick guard plates have been placed to help keep the fields uniform (see Fig. 4.1). Each plate, including the front, back and mid plates, is electrically connected to the preceding plate by a 3.0 MΩ precision resistor, forming a voltage divider network between the mid plate and the front plate, and between the mid plate and the back plate. The resistors are inside the vacuum chamber and have matched temperature coefficients of 15 ppm/°C (parts per million per °C). The center-to-center spacing between plates in the front stage is 1.000 in.; whereas, in the back stage it is 1.04 in. The first guard plate (behind the front plate), has inner and outer dimensions 15.125 in. x 28.000 in. and 18.125 in. x 31.000 in., respectively. Furthermore, the height of each successive plate decreases gradually to make the analyzer fit in the vacuum chamber at 45° (see Fig. 4.1).

Finally, the stainless steel vessel is pumped by two 345 liter per. sec. (for N_2) Leybold-Heraeus turbomolecular pumps. Pressures of 3.0×10^{-8} torr have been achieved.

In the following analysis the equations will be derived for an idealized case. Inhomogeneic effects due to meshes and guard plates will be neglected.

4C.2 DESIGN CRITERIA

It is well known that the optimum conditions for first order focus and resolution are the same: particles must enter the analyzer at 45° with respect to the plates. Fig. 4.13 shows the front (plane A), the mid (plane B), and back (plane C) plates along with representative trajectories for H^+, H_2^+, H_3^+, H^-, and neutrals (H or H_2, represented by N_0). R denotes the collision center and S is its projection onto the plane A (front plate's plane). The projections of the collision center onto the plane B and C are shown by U

and T respectively. Note that these intersections are out of the plates, since the plates do not extend to the line passing through the collision center and S. Each trajectory with its corresponding laboratory scattering angle defines a plane that is perpendicular to the analyzer's plates. For example, particles scattered at 0° and at θ_3 are confined to the plane RQS and RVS, respectively. We define a right-handed rectangular coordinate system with its x-axis in the front plate's plane (plane A), parallel to the projection of the beam direction onto the plane A, as shown in Fig. 4.13. The y-axis of this coordinate system is perpendicular to the plane A, directed from plane A to plane B. The z-axis is also in the plane A and perpendicular to both x- and y- axes. Thus, the acceleration in the analyzer is confined to the y-direction. The origin of the coordinate system is at the geometrical center of the entrance slit (point Q in Fig. 4.13).

For the various charged particles entering the analyzer, the initial velocity components along the directions x, y, and z are

$$V_{ox} = V_o \cos\theta \cos\alpha \qquad (4.2a)$$

$$V_{oy} = V_o \cos\theta \sin\alpha = V_o \sin\gamma \qquad (4.2b)$$

$$V_{oz} = V_o \sin\theta, \qquad (4.2c)$$

where θ is the laboratory scattering angle; γ, the injection angle for a laboratory scattering angle of θ; and $\alpha=\pi/4$, the injection angle at $\theta=0°$. Due to the finite entrance slit dimensions, there is an uncertainty $\Delta\alpha$ in the angle α.

For a positively charged particle landing on the front plate (plane A, Fig. 4.13), the range of its parabolic path is

$$R = R_o \sin 2\gamma = 2R_o \sin\gamma \cos\gamma \qquad (4.3a)$$

where

$$R_o = \frac{2E_+ d_1}{qV_{an}} \qquad (4.3b)$$

Using equation (4.2b), one obtains

$$R = 2R_o \sin\alpha \cos\theta_1 \sqrt{1-\sin^2\alpha \cos^2\theta_1} \qquad (4.3c)$$

where E_+ is the laboratory energy of the positively charged particle produced in the collision cell; V_{an}, the potential applied to the analyzer; q, the charge; d_1, the distance between the mid plate and the front plate; and θ_1, the laboratory scattering angle. The present slit opening yields a $\Delta\alpha$ of $\pm 0.051°$ as measured from the center of the collision cell. In that case, using equation (4.3a), the departure from first-order focusing ($\theta_1 = 0$ and $\alpha = 45°$) is $1.586 \times 10^{-6} R_0$ (Yarnold and Bolton 1949). Combining equations (4.3b) and (4.3c), one gets

$$E_+ = \frac{R\, q\, V_{an}}{4d_1 \sin\alpha \cos\theta_1 \sqrt{1-\sin^2\alpha \cos^2\theta_1}} \qquad (4.3d)$$

The analyzer resolution can be computed by applying standard error analysis techniques to equation (4.3d). For α=45°, the full width at half maximum (FWHM) resolution is

$$\left(\frac{\Delta E_+}{E_+}\right)_{FWHM} = \frac{1}{2}\left[\left(\frac{\Delta V_{an}}{V_{an}}\right)^2+\left(\frac{\Delta d_1}{d_1}\right)^2+\left(\frac{\Delta R}{R}\right)^2+\left(\tan\theta_1-\frac{\sin(2\theta_1)}{2(2-\cos^2\theta_1)}\right)^2(\Delta\theta_1)^2+\left(\frac{2\sin^2\theta_1}{\cos^2\theta_1-2}\right)^2(\Delta\alpha)^2\right]^{\frac{1}{2}} \quad (4.4)$$

where ΔR is the sum of entrance slit opening and the image resolution of the positive particle detector. The main contribution to the resolution comes from the $\Delta R/R$ term. The contributions to the resolution from the angular terms are estimated to be about 0.001% for θ_1 as large as 5°.

4C.3 PROTON DETECTORS

The detector assembly is actually seven detectors in one housing. It is a novel design and deserves some discussion. Each of the seven detectors consists of a pair of 25 mm MCPs and a pair of large anodes; thus, the name discrete anode position sensitive detector (DAPSD).

All the anodes are printed on one circuit board (PCB) which was manufactured by Metro Circuits Inc. (refer to Fig. 4.14). The PCB is double-sided with one side consisting of the signal electrodes and the other, the anodes. Each pair of anodes is

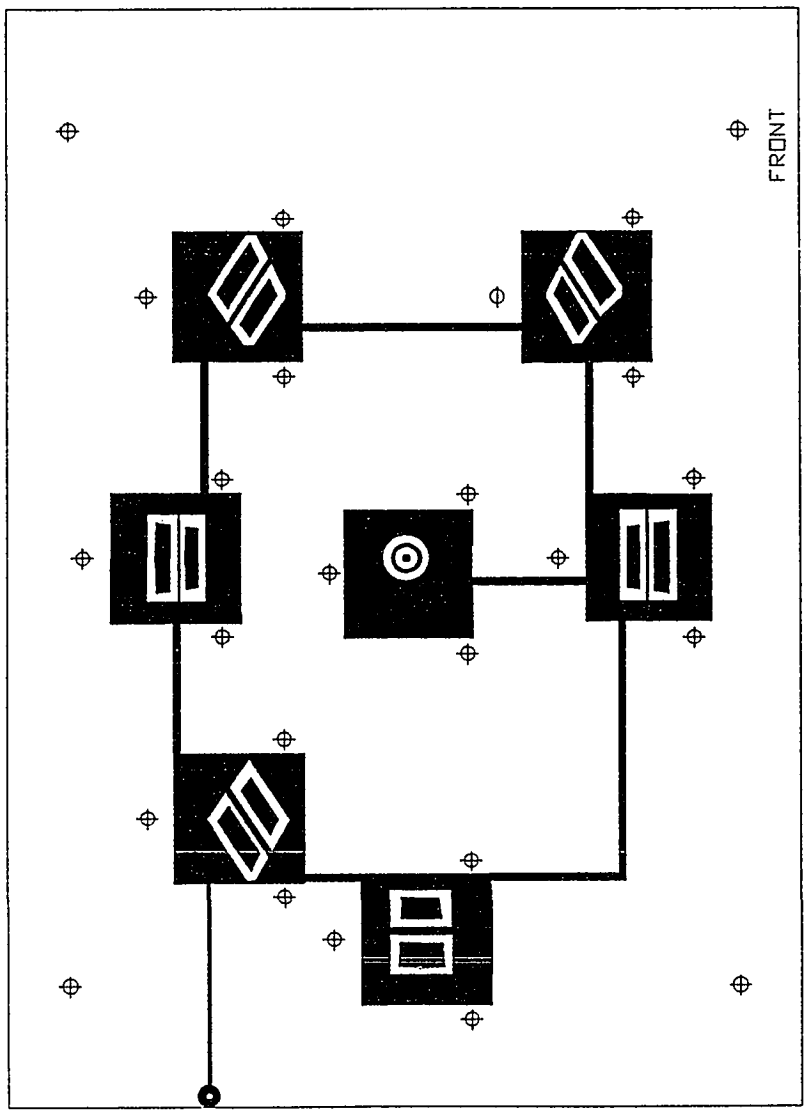

Figure 4.14: Front side of printed circuit board. The holes forming equilateral triangles are the mounting holes for the MCP holders. The anodes are inside the dark regions which are used to reduce the non-conducting regions (see text). The actual size of the board is 9.000" x 6.500".

surrounded by an electrode (high-voltage plane) to reduce the non-conducting PCB region. Such regions charge up leading to electric fields which could distort the electron's path from the MCP to the anode. The center anode, which is 0.06 in., is specifically used to calibrate the energy analyzer. Because the center of the PCB must be well known, it was determined by a high-precision travelling microscope.

In designing the anode configuration, the kinematic equation for H_2^+ dissociation (equation 2.2), and the equations for the protons's parabolic trajectory (equation 4.3) for various inelastic energy loss, Q and proton center-of-mass energies and angles, ϵ and ϕ were implemented. A graph pinpointing the coordinates for protons landing on the front plate of the analyzer is shown in Fig. 4.15. The calculation assumes a constant analyzer voltage. Therefore, all trajectories are referenced with respect to one path. In this case, the reference trajectory has Q=23.4 eV, ϕ=0, and the range is 21 in.

The trajectories for Q=23.4 eV and Q=21.6 eV, and ϕ=0°, $\pm$45°,90°, -135°,180° were chosen. There are two reasons for this decision:(1) the size limitations of the analyzer and MCPs; and (2) the inelastic energy losses lie in the Franck-Condon region of the H_2^+ potential energy curves.

The sizes of the anodes were determined by letting the uncertainty in the center-of-mass angle to be 5° and $\Delta\epsilon/\epsilon$=19%. This yields an approximate anode size of 0.13 in. x 0.50 in. which is 28 times as large as in previous experiments (Yenen *et al* 1990). This will increase the coincidence rate with the consequence of decreased energy resolution. The energy resolution (see equation 4.4) and laboratory acceptance angles for all the anodes are tabulated in Appendix C.

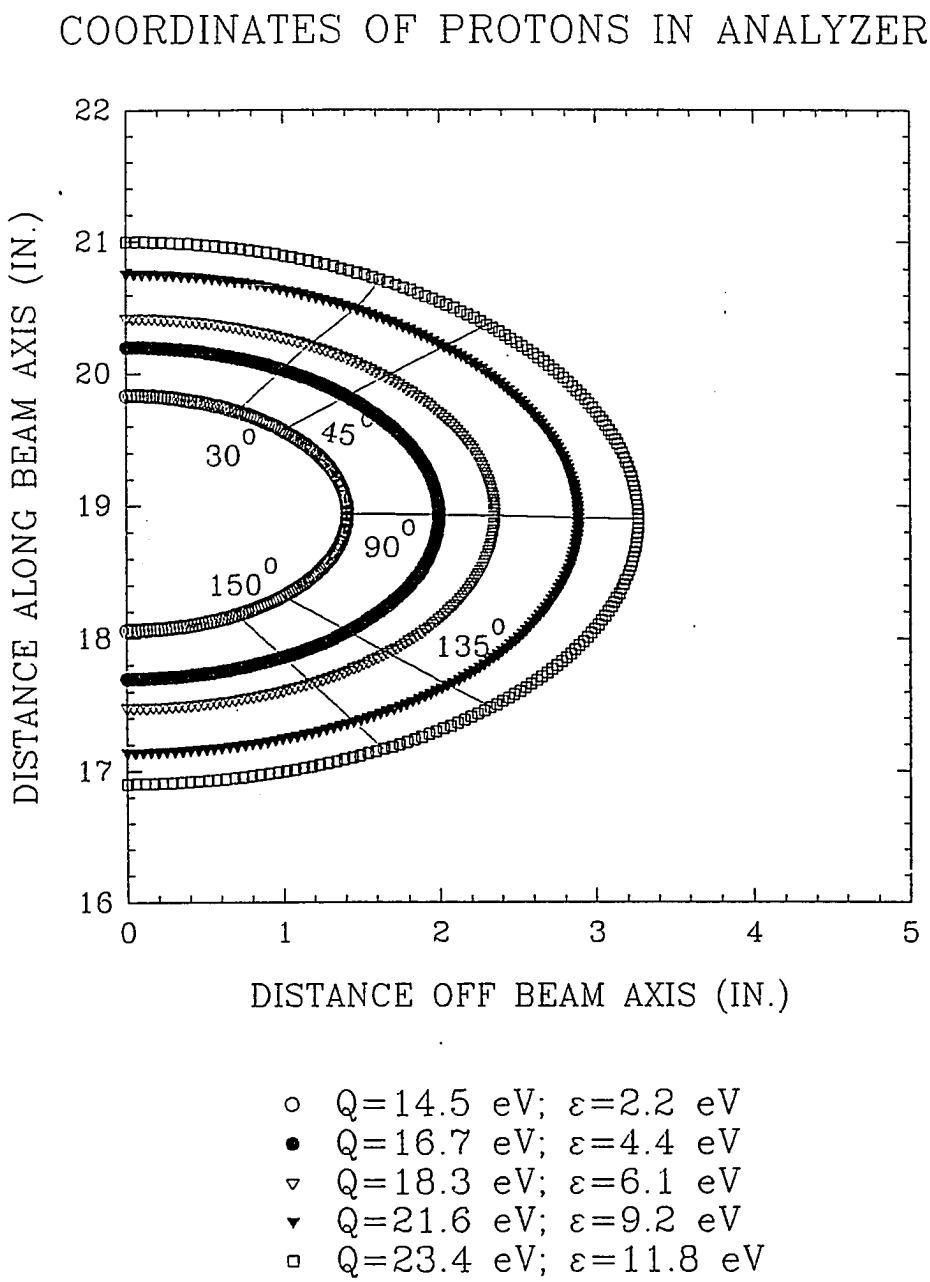

Figure 4.15: Coordinates of protons in the analyzer as a function of internuclear orientation; entrance slit is parallel to the abscissa. Note that the greater the Q value, the greater the maximum range and the lesser minimum range.

The MCPs are placed in specially machined holders and mounted to the PCB (see Fig. 4.16). Each pair of MCPs has its own power supply to reduce the nasty problem of anode-to-anode cross-talk.

4C.3a PROTON DETECTOR ELECTRONICS

One extracts the proton signal with the proper detector circuit and shielding. In the present experiment the MCPs run in the pulse counting mode. The details of the detector electronics will be presented to familiarize the reader with the signal processing.

The detector circuit is shown in Fig. 4.17. The circuit is designed such that each MCP has the same bias voltage (900-1000 V). This establishes a maximal gain for each MCP. To satisfy operating requirements, current limiting resistors of 9.4 megohms reduce current flow through each MCP to 120 μA. The capacitors which are parallel to these resistors provide a short for any voltage transients which may occur.

When the electron charge cloud hits the anode, it possesses a certain diameter. However, to improve the image resolution, the diameter of the charge cloud must be reduced. Wiza (1977) has done this by biasing the second MCP with respect to the anode. In the present detector this is accomplished by placing a 1.0 megohm resistor between the anode and the MCP. The electric field which is produced by this resistor also helps direct the electrons toward the anode. However, the electric field is restricted to approximately 2000 V/cm to reduce any space charge effects.

The signal is finally coupled to a LeCroy 7790 preamplifier via a 100pf blocking capacitor. The LeCroy preamplifier's threshold is helpful in reducing crosstalk. The presence of the 0.1 megohm resistor allows the capacitor to discharge through the power

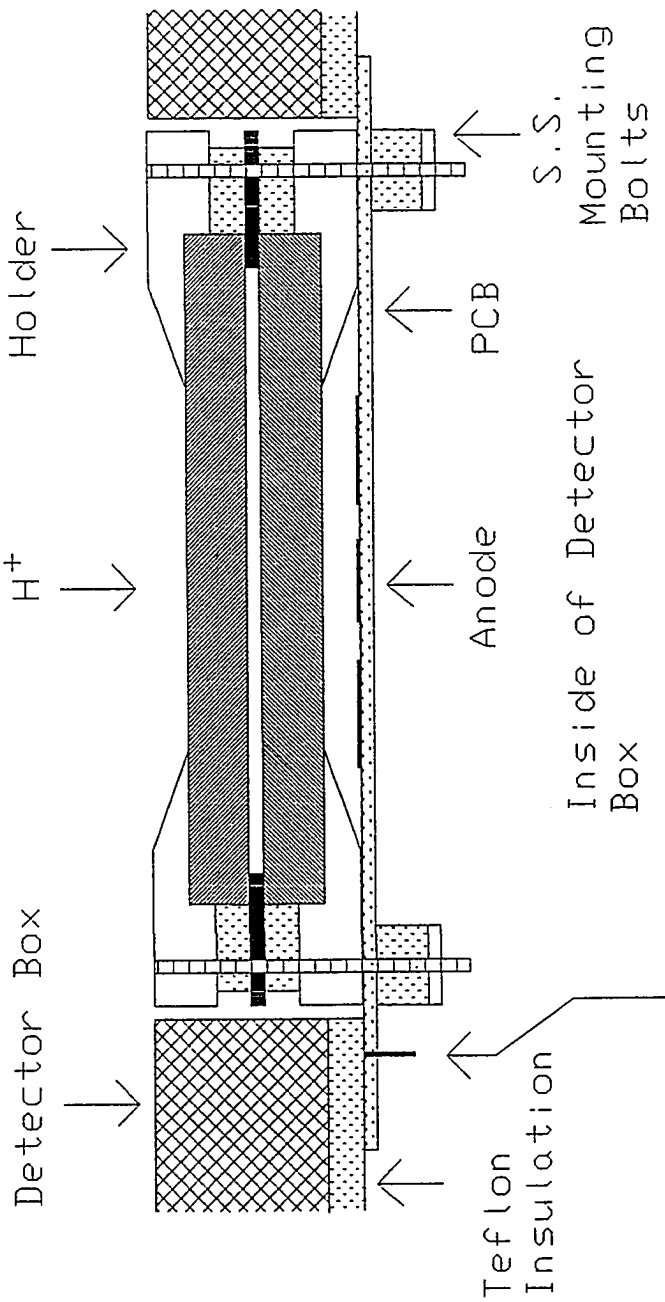

Figure 4.16: Side view of MCP holder. The figure also shows how the detector is mounted. Note that the MCP holders are mounted directly to the PCB. The cross-hatched area denotes the aluminum detector box (housing). Insulating beads around the mounting screws are not shown (for clarity). The stainless steel holders (unshaded areas) are 0.036 in. thick. The CuBe tab (dark area) is 0.005 in. thick. The insulators (dotted areas) between the tab and the stainless steel holders are 0.007 in. thick. The thickness of the MCPs (hatched areas) are 0.017 in. Finally, the diameters of the tabs and MCP holders are 1.690 in.

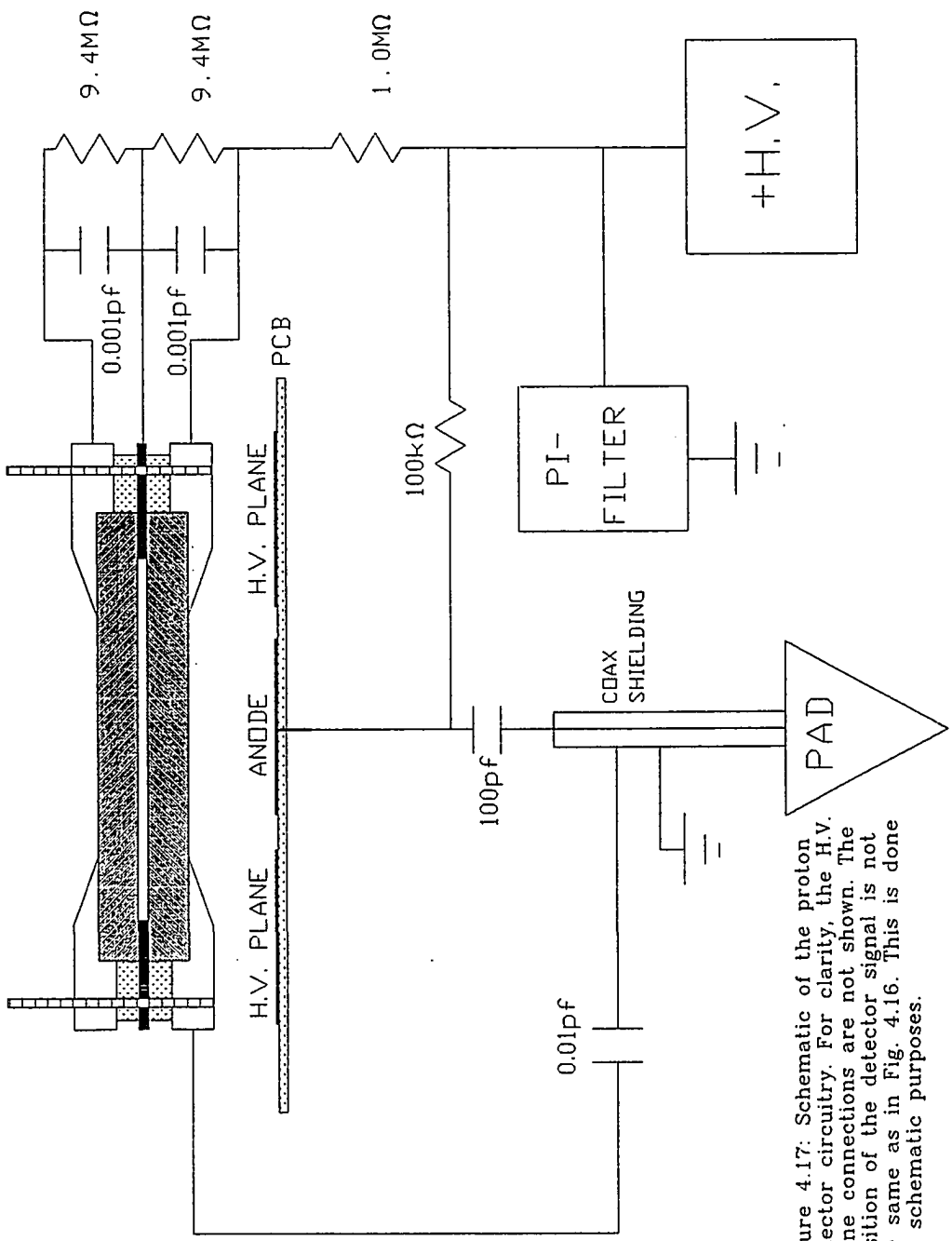

Figure 4.17: Schematic of the proton detector circuitry. For clarity, the H.V. plane connections are not shown. The position of the detector signal is not the same as in Fig. 4.16. This is done for schematic purposes.

supply.

Signals on the high-voltage plane are coupled to ground via a 0.001 μf capacitor. A final capacitor, 0.01 μf, completes the a.c. part of the circuit.

CHAPTER 5

EXPERIMENTAL PROCEDURE

5A. INTRODUCTION

A complete description of the laboratory and center-of-mass velocities of the colliding particles requires knowledge of the nine velocity components of the three particles. Because of conservation of energy and momentum, the number of unknowns reduces to five. With the approximation that the total loss of the projectile's kinetic energy is incurred because of its excitation, the number of unknowns reduces further to four. In this experiment, however, only two of these unknowns will be measured, namely $\bar{V}_1$ and θ_1 (refer to Fig. 2.3). Since polarized L_α radiation is detected in coincidence with the scattered proton, one can extricate details of the excitation processes which produce $H^+ + H(2p)$ from the collision induced dissociation of H_2^+. Moreover, the data acquired in the present experiment yields information about the relative populations of the excited molecular states of H_2^+ as a function of internuclear separation and orientation of the parent molecule, and the center-of-mass energy ϵ_+ of the fragment particles. This chapter describes experimental procedure for data accumulation and their analysis.

5B. DETERMINATION OF ϵ_+ AND ϕ

To perform the present experiment, a knowledge of the laboratory and center-of-

mass energies of the scattered protons are required. This section presents the methods used in determining the center-of-mass energies and angles of the positively charged fragment. Various aspects of the laboratory frame energy distributions for protons scattered at 0°, 1.88°, and 2.12° will be discussed.

Before performing any energy loss measurement the energy analyzer must be calibrated. Details of the calibration procedure were described at great length by Wiese (1993). Her analysis suggest that the analyzer constant is best determined when the analyzer is calibrated for the particular particle energy to be used in the experiment. The analyzer constants for the anodes at 0° (R=21.000"), +1.88°, and +2.12° are presented in caption of Figs. 5.1-3. These are averages of several runs at 4.0 keV.

The laboratory energy distributions of the protons produced at the three laboratory angles are shown in Figs. 5.1-3. Each of these spectra are obtained with the new proton detector system which is described in Ch. 4 Sect. 4B.3a. Also, each spectrum is normalized to the total L_α counts which are simultaneously monitored during the 10s. data accumulation time. Since the L_α count rate was about 50-60 Hz, this introduced an error of about 5 percent in the normalization process. This accounts for the observed fluctuations in the laboratory energy spectra.

The details of proton spectra collected along the beam axis have been discussed at great length elsewhere (Yenen *et al* 1990). The central peak refers to protons with near-zero center-of-mass energy. Because all internuclear orientations are possible, the detector is most efficient in collecting particles of this energy. The two side-peaks (Aston bands) shown in Fig. 5.1 represent protons scattered in the forward and backward

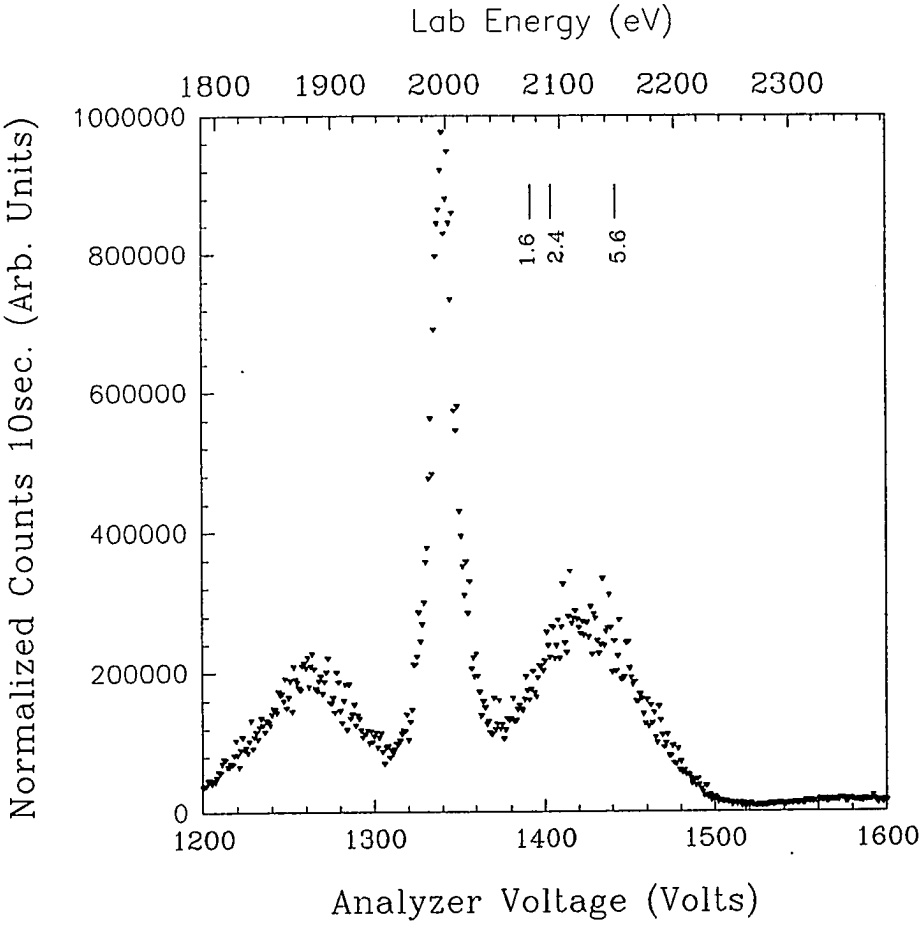

Figure 5.1: Laboratory energy distribution of protons from 4.0 keV H_2^+ incident on He. The protons are collected along the beam axis (R=21.000 in.). The experimentally determined analyzer constant for this R is 1.4922. The peak of this spectrum occurs at 1339 V. Also shown are the non-zero center-of-mass energies $2\varepsilon_+$ of the protons which are detected in coincidence with the photons in the present experiment. These are denoted by the vertical lines. This data is obtained with the detector described in Ch. 4 Sect. 4C.3. The data are normalized to the total L_α counts for the 10s. counting time (see text).

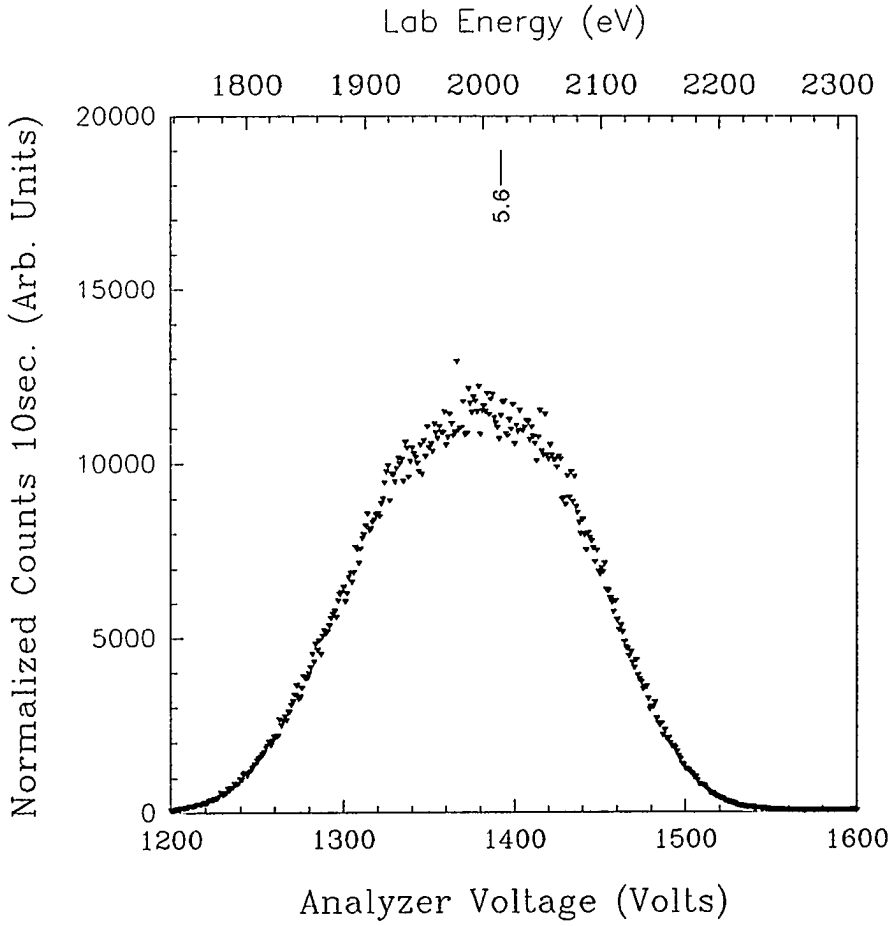

Figure 5.2: Laboratory energy distribution of protons from 4.0 keV H_2^+ incident on He. The protons are collected at 2.12° in the lab frame (R=20.397 in.). The experimentally determined analyzer constant for this R is 1.4472. The peak of this spectrum occurs at 1382 V. Also shown are the center-of-mass energies $2\varepsilon_+$ for the protons which are detected in coincidence with the photons in the present experiment. These are denoted by the vertical lines. This data is obtained with the detector described in Ch.4 Sect. 4C.3. The data are normalized to the total L_α counts for the 10s. counting time (see text).

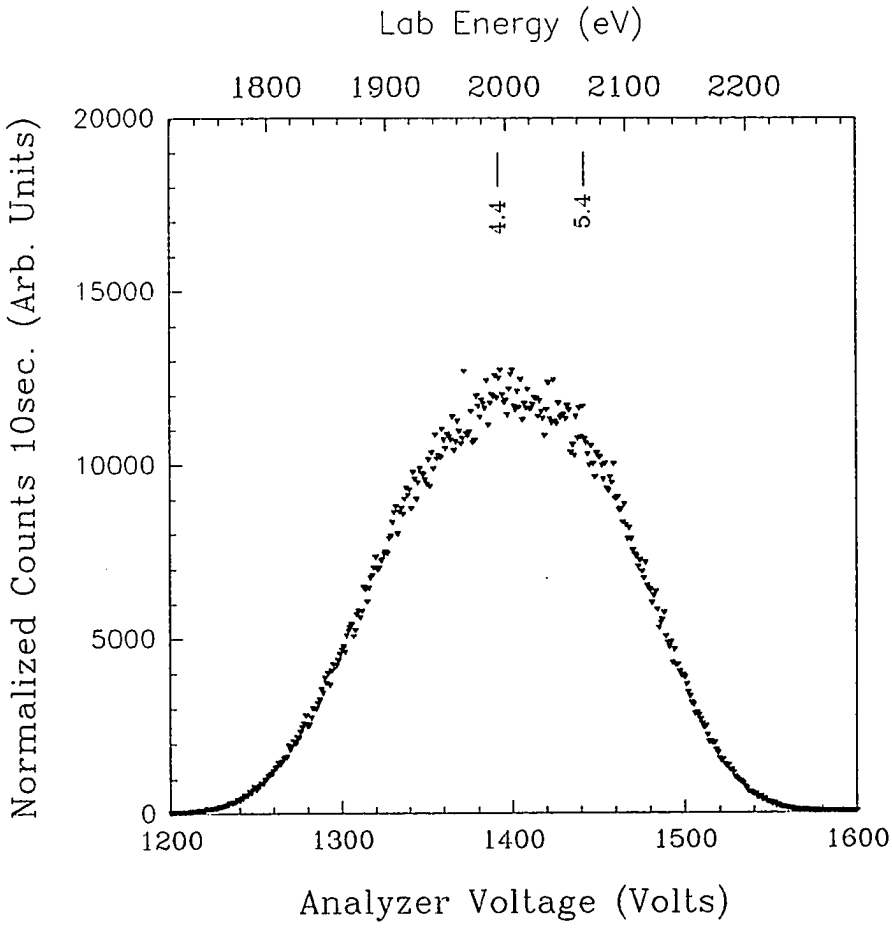

Figure 5.3: Laboratory energy distribution of protons from 4.0 keV H_2^+ incident on He. The protons are collected at 1.88° in the lab frame (R=20.224" in.). The experimentally determined analyzer constant for this R is 1.4349. The peak of this spectrum occurs at 1397 V. Also shown are the center-of-mass energies $2\varepsilon_+$ for the protons which are detected in coincidence with the photons in the present experiment. These are denoted by the vertical lines. This data is obtained with the detector described in Ch.4 Sect. 4C.3. The data are normalized to the total L_α counts for the 10s. counting time (see text).

directions in the center-of-mass frame. Their broad nature is due to the superposition of many Qs and ϵs produced by many different mechanisms (Yenen *et al* 1990).

Particles scattered in the forward direction are more efficiently collected. Since the detector has a finite size, there is a finite acceptance range of the laboratory scattering angle and the instantaneous center-of-mass angle of the parent molecule. Note from equation (2.3) that $E_{1\pm}$ varies very slowly with ϵ_+. If ϵ_+ doubles, $E_{1\pm}$ will not. Moreover, for increasing ϵ_+ equation (C.5) predicts that ϕ increases as E_{1+} (forward scattering) increases and decreases as E_{1-}(backward scattering) decreases. The converse is true if ϵ_+ decreases. This means that the detector subtends a larger solid angle for protons scattered in the forward directions, meaning that more particles are collected.

After colliding with the target, the velocity and energy of the center-of-mass of H_2^+ are V_o and $E=(E_o-Q)/2$ (see Fig. 2.3). Therefore one can estimate the center-of-mass energy of the proton at any point of the laboratory energy distribution by

$$\epsilon_+ = E+E_1-2\sqrt{EE_1} \qquad (5.1)$$

For protons scattered at non-zero laboratory angles, the spectra appear different than those of $\theta_1=0°$. The question remains, "What do the peaks in these two spectra mean?" One must first try to estimate ϵ_+ and ϕ before attempting any explanation. Equation (5.1) can be generalized to any laboratory angle by (see Appendix C.3)

$$\epsilon_+ = E+E_1-2\sqrt{EE_1}\cos\theta_1 . \qquad (5.2)$$

Therefore, the instantaneous orientation of the parent molecule (relative to the beam axis) just before dissociation is written as (see Appendix C.3)

$$\phi = \arccos\left[\frac{E_1 - E - \epsilon_+}{2\sqrt{E_1 \epsilon_+}}\right]. \qquad (5.3)$$

To calculate the corresponding ϕ of each peak, one must first calculate ϵ_+ with equation (5.2). Its result is then implemented in equation (5.3). The results of these calculations show that the peak of each laboratory spectrum corresponds to an instantaneous internuclear orientation of 90° relative to the beam axis. The uncertainty in this value is $\pm 12.4°$ for protons collected at a laboratory angle of 1.88° and $\pm 9.5°$ for protons collected at a laboratory angle of 2.12° (see Appendix C for more details).

As shown in Fig. 1.1, a particular value of ϵ_+ can encompass many excited states of H_2^+. However, the alignment of the charge cloud will give further information about the six excited states producing $H^+ + H(2p)$. For example, if the charge cloud is oriented perpendicular to the quantization axis, then the $2p\pi_u$ and $3d\pi_g$ states dominate the excitation process. Fig. 1.1 also shows that the $2p\pi_u$ and $3d\pi_g$ states come from different vibrational states of the $1s\sigma_g$ orbital. Thus, from the Franck-Condon vibrational population factors (see Ch. 2), one can infer which of the two molecular orbitals contributes the greatest.

5C. DATA COLLECTION

The coincidence electronics are shown in Fig. 5.4. Only one of the five multichannel analyzers (3 are Ortec 916A MCAs and 2 are Canberra Omega-1 MCAs) are shown in the block diagram. This was done for clarity. The coincidence unit is used as a fanout for the photon signals. A typical time spectrum is shown in Fig. 5.5. Data accumulation times vary from 24 to 170 hours. Since data accumulation times are so long, the ion source must be monitored closely at all times.

The number of coincidences are obtained in the following manner. First, the number of accidental coincidences (or background) must be determined. The accidentals are shown in Fig. 5.5 as regions A and C. These regions encompass n and p channels respectively. One then sums over these regions and divides by the total number of channels to obtain the number of accidental coincidences per channel. The peak region B which consists of both real and accidental coincidences span q channels. One multiplies the number of channels in this region by the average number of accidentals per channel to obtain the number of background counts in this region. Thus, the number of real coincidences are written as

$$N_c = B - \frac{q}{p+n}(A+C) = N_{CA} - \frac{q}{p+n}N_A, \qquad (5.4)$$

where N_{CA} denotes the number of real plus accidental counts in region B; and N_A, denotes the number of accidentals in regions A and C. The statistical uncertainty in N_C

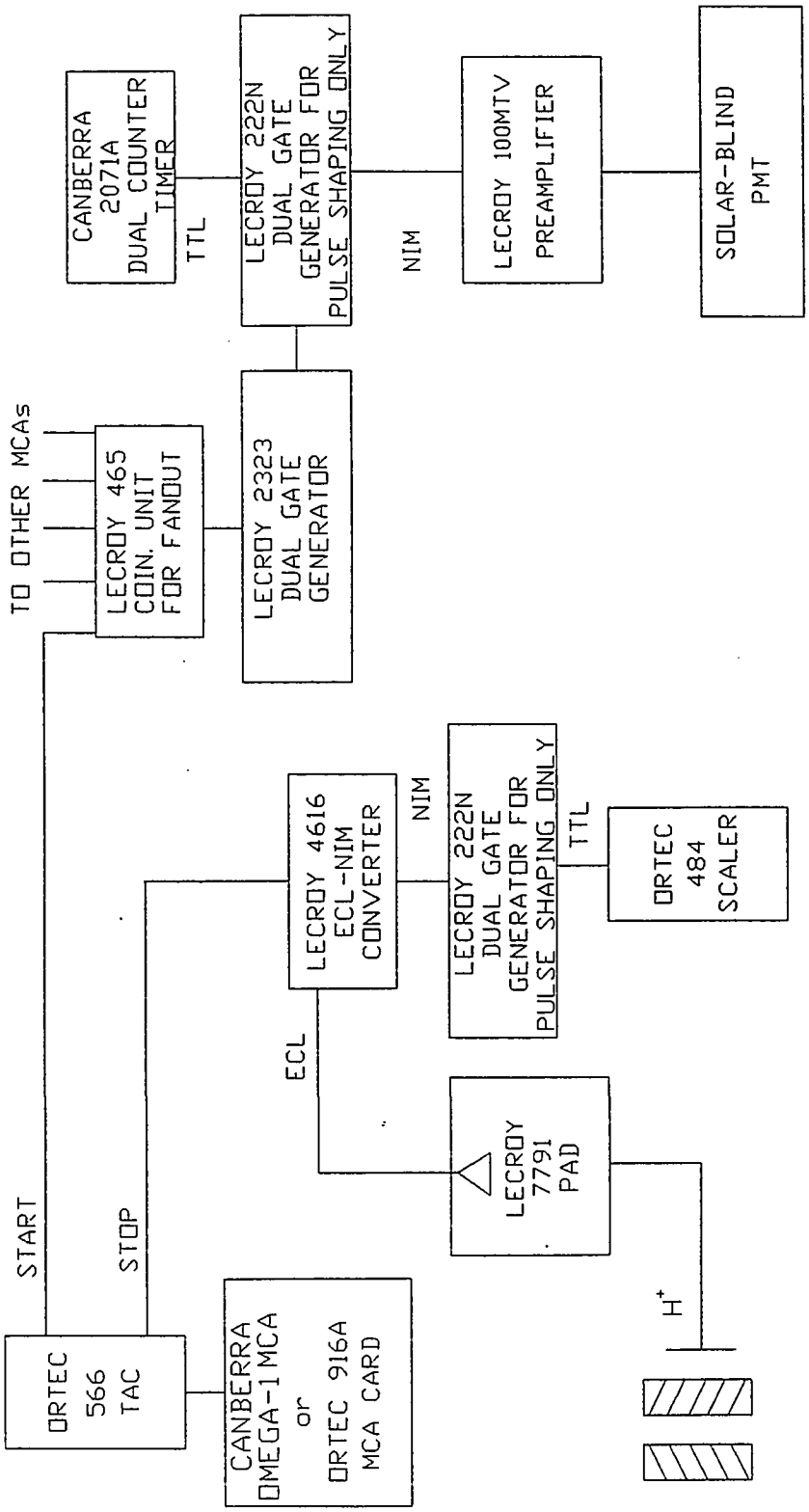

Figure 5.4: Coincidence electronics.

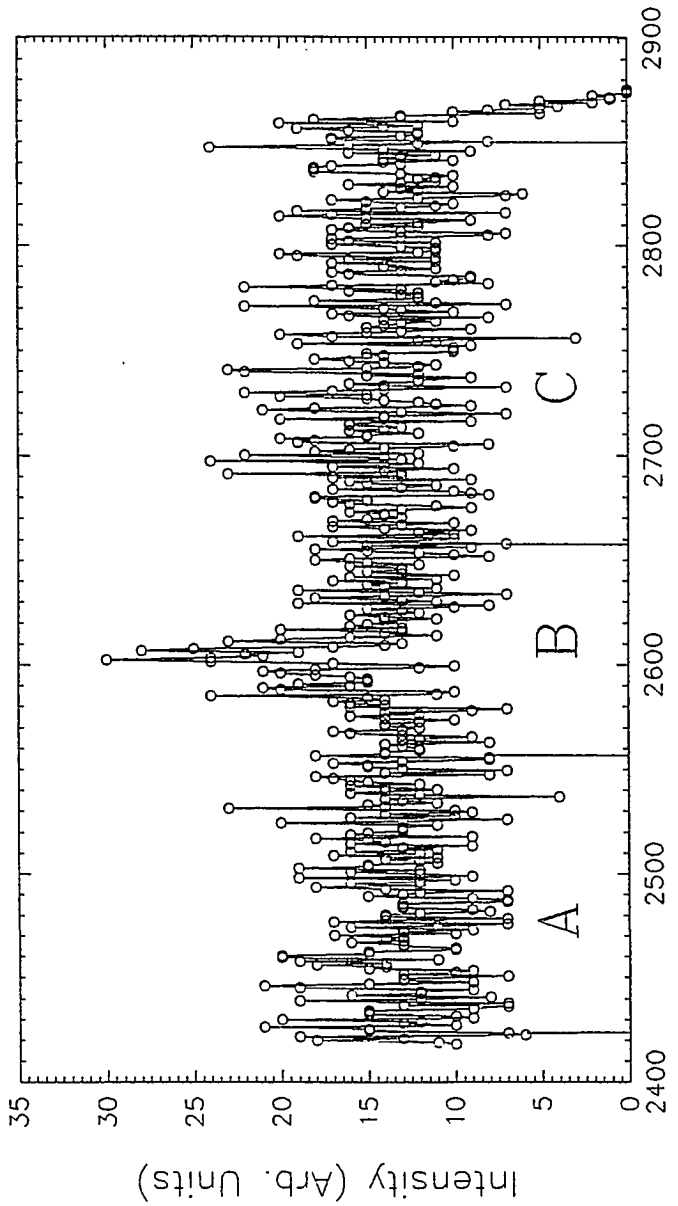

Figure 5.5: Sample time spectrum for the present experiment.

is therefore,

$$\Delta N_C = \sqrt{B+\left(\frac{q}{p+n}\right)^2 (A+C)} = \sqrt{N_{CA}+\left(\frac{q}{p+n}\right)^2 N_A}\,. \qquad (5.5)$$

Because the count rate of the stop signal (proton signal) varies from 5 to 20 kHz, the loss of true events caused by MCA dead times are neglected since such effects do not become important until the stop count rates are above 200 kHz (Hoffman *et al* 1982). Also, since the count rate is small, the time spectra do not assume the characteristic Poisson shape (Hoffman *et al* 1982 and Fornari 1981).

The number of coincidences which are extracted from each time spectum are normalized to the number of proton counts N_+. Note that N_C and N_+ depend upon the detector efficiency (shown below). This means that the detector efficiency dependence drops out in the normalization process.

Some insight into the target pressure and beam current dependence of N_C can be obtained if one examines equation (5.3) more closely. As discussed by Dupre *et al* (1991), the number of accidental and real coincidences can be written as $N_A=K_A(nI)^2t$ and $N_C=K_C(nI)t$, respectively, where n is the target density; I, the beam current;t, the data accumulation time; and K_A and K_C, constants which depend on products of detector efficiencies, angular and energy resolutions and cross sections. After putting these results into equation (5.5), one obtains

$$\frac{\Delta N_C}{N_C} = \frac{1}{\sqrt{t}}\left[\frac{1}{K_C(nI)} + \frac{K_A}{K_C^2}\left(\frac{q}{n+p}\right)\left(1+\left(\frac{q}{n+p}\right)\right)\right]^{\frac{1}{2}} . \quad (5.6)$$

When the number of accidentals is much greater than the number of real coincidences, the first term in the above expression can be neglected. This is the case in the present experiment.

Finally, the results for each set of polarization data are fitted to equation (3.8b). The results of each set of polarization data are discussed in the following chapter.

5D. PRELIMINARY RESULTS

To determine the feasibility of the present experiment, L_α were detected in coincidence with protons scattered along the beam axis for a polarizer setting of 45°. The number of coincidences were measured as a function of laboratory energy (analyzer voltage). Note that the particle and photon detection systems described by Yenen *et al* (1990), Jaecks *et al* (1990), and Mueller (1982) were employed. The results are shown in Fig. 5.6. The large peak refers to nears-zero energy projectile frame protons. This large peak is due to the high collection efficiency for near-zero energy protons. The nominal number of coincidences at larger analyzer voltages shows that one can obtain results within a reasonable time. Notice how rapidly N_C varies around the peak. Since the analyzer voltage is known within one volt, it seems very difficult to resolve the peak. However, if this spectrum is transformed into the center-of-mass frame of the proton,

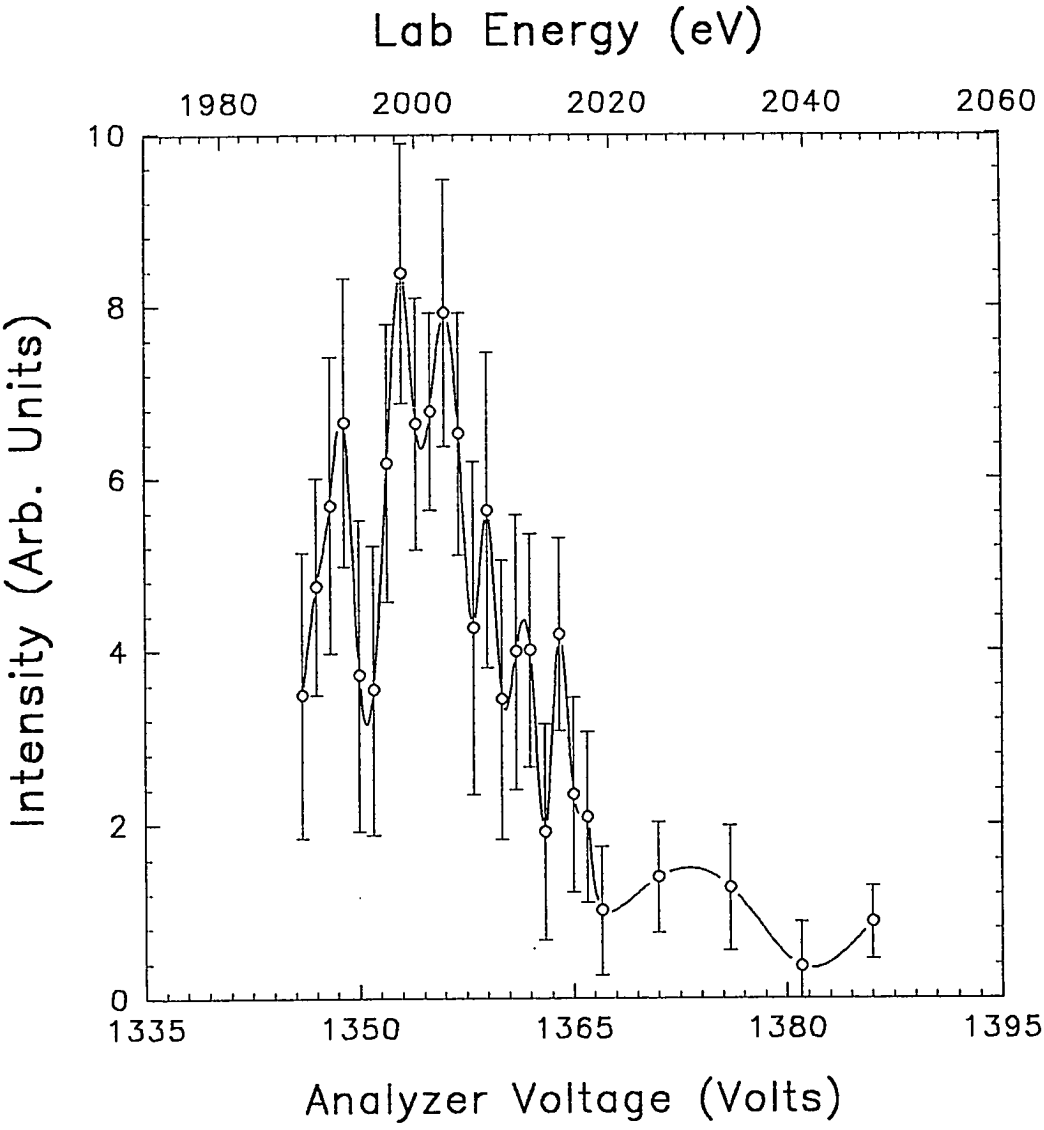

Figure 5.6: Laboratory energy distribution of protons collected (along the beam axis) in coincidence with L_{α}. The polarizer is set to $\alpha=45^{\circ}$. This data was obtained with the apparatus described by Yenen et al (1990). The range of the proton in the analyzer was R=20.648 in. The number of coincidences are normalized to the total photon counts.

then it is possible to determine the exact position of the peak. The results are shown in Fig. 5.7. The transformation technique has been discussed extensively by Wiese (1993). It assumes an isotropic projectile frame distribution of protons. Since the number of protons that reach the detector is independent of the reference frame, the ratio of the number of protons collected by the detector to the to the total number scattered in 4π is equal to the ratio of the detector solid angle to 4π. The detector solid angle is related to the laboratory acceptance angle of the detector. Furthermore, the laboratory acceptance angle is related to the center-of-mass acceptance angle of the detector through equation (C.5) of Appendix C. Since these two angles are related through the laboratory energy of the proton E_1, the transformation will depend on the value of Q (see equation 2.2). One then finds the optimal value of Q when the distribution of protons in the forward directions matches the distribution of protons in the backward direction. From this transformation the peak of the laboratory spectrum occurs at 1350.5 V, yielding a Q value of 10.0 eV. The question remains,"How does this distribution compare with the center-of-mass distribution for total proton production?"

The center-of-mass distribution is obtained by transforming the laboratory spectrum of Jaecks *et al* (1990; see also Appendix E). The results are shown in Fig. 5.8. The optimal value of the inelastic energy loss was determined to be Q=26.6 eV. Since the most probable center-of-mass energy occurs at approximately 2.8 eV, and since excitation of the molecular states producing H(2p) only add 10.2 eV to the total inelastic energy loss, then target excitation must occur. This is reasonable since the results of Russek and Furlan (1989) also predict target excitation in H_2^++He collisions. However,

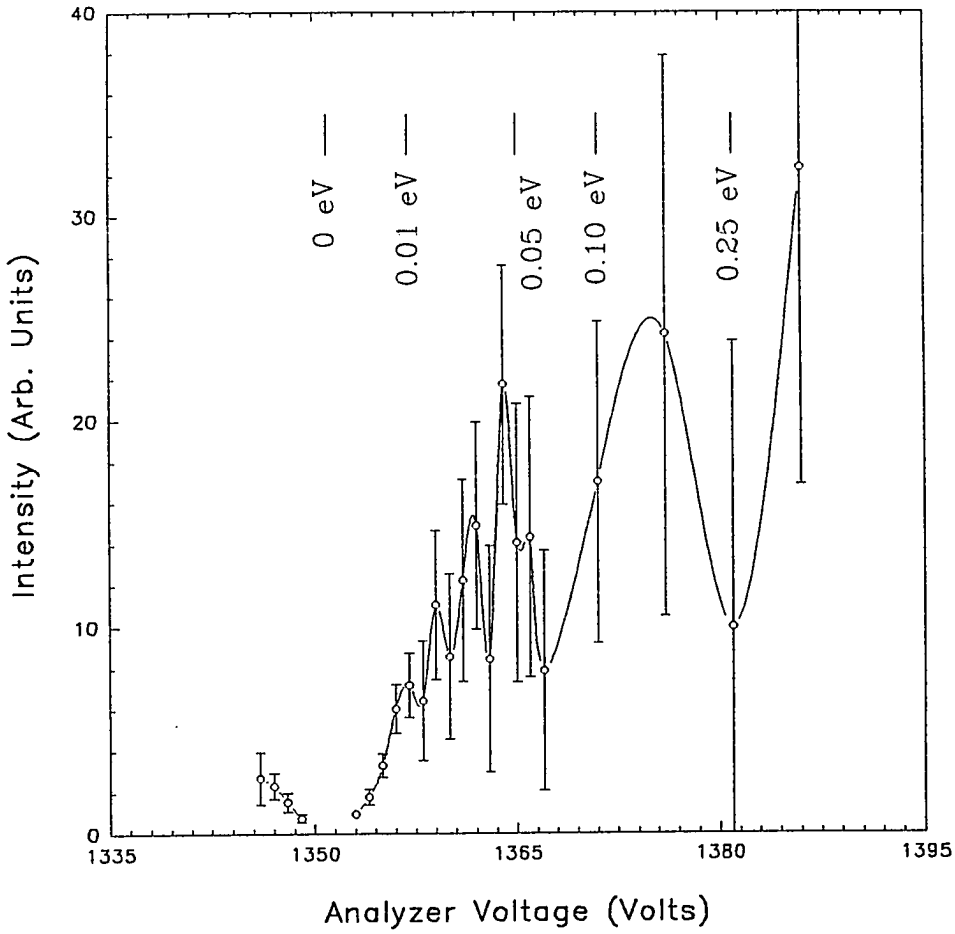

Figure 5.7: Center-of-mass energy distribution of protons collected (along the beam axis) in coincidence with L_α. The polarizer is set to $\alpha=45^\circ$. The peak occurs at an analyzer voltage of 1350.5 V, yielding a Q of 10.0 eV. This data was obtained with the apparatus described by Yenen et al (1990). The range of the proton in the analyzer was R=20.648 in.

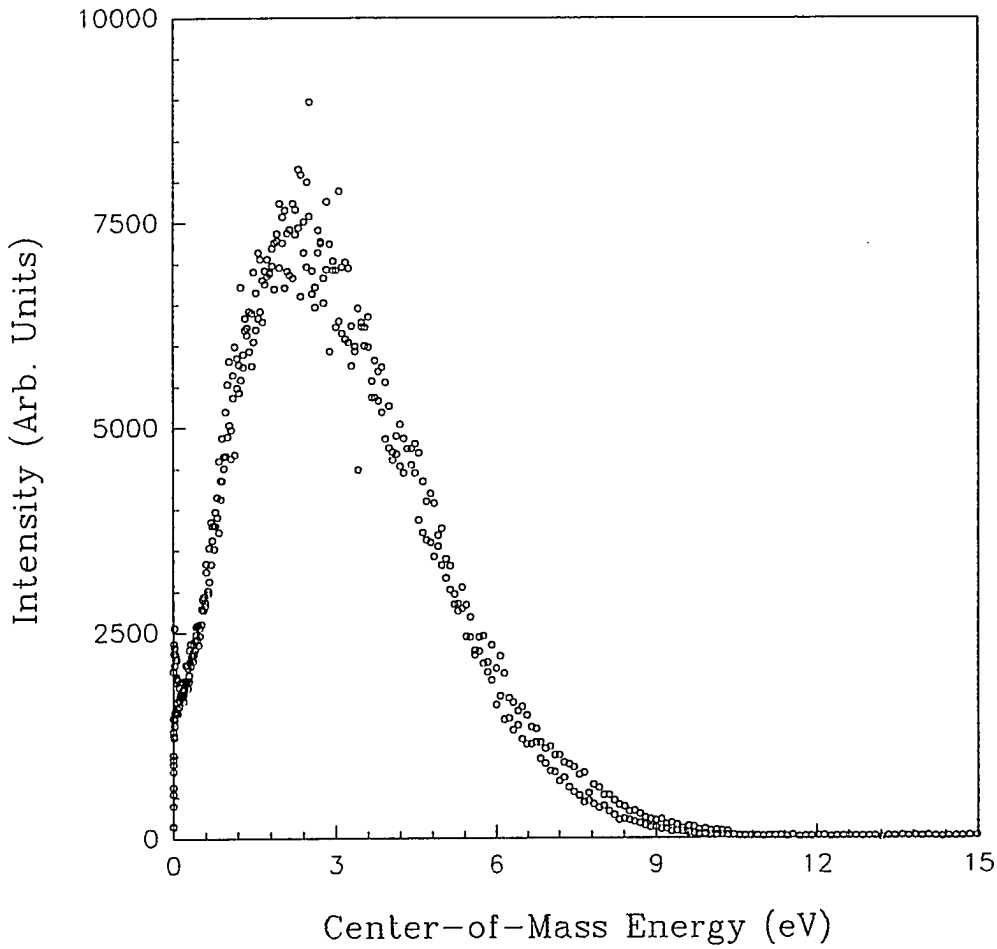

Figure 5.8: Center-of-mass energy distribution of protons from 4.0keV H_2^+ incident on He. The protons are collected along the beam axis. (R=20.648 in.). The best Q for the fit is 26.6 eV.

since near-zero energy projectile frame protons result from a Q of 11.6 eV, as measured from the laboratory spectrum of Jaecks *et al* (1990), the value of Q obtained from the center-of-mass transformation must agree reasonably well with this result at near-zero center-of-mass energy. The results of the transformation are shown in Fig. 5.9. The Q-value of 12.6 eV agrees well with the value obtained from the center-of-mass transformation. It also agrees reasonably well with the Q obtained from the center-of-mass transformation of the H^+-L_α coincidences of Fig. 5.6 (see Fig. 5.7). These transformations illustrate the number of Qs which can occur in collisions involving molecular excitation.

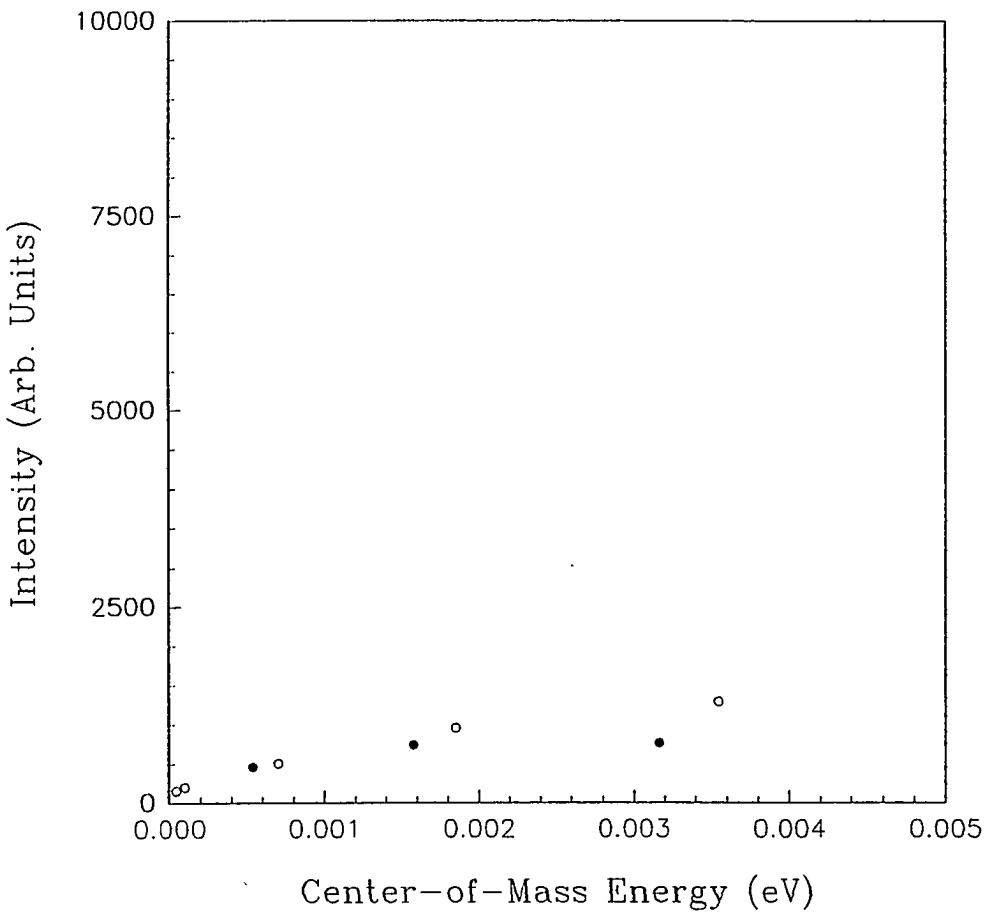

Figure 5.9: Center-of-mass distribution of near-zero protons from 4.0keV H_2^+ incident on He. The protons are collected along the beam axis. (R=20.648 in.). The best Q for the fit fit is 12.6 eV. The filled in circles represent protons in the forward direction. The open circles represent protons in the backward direction.

CHAPTER 6

RESULTS AND DISCUSSION

The results of several experimental runs are presented and discussed in this chapter. The results of all the runs are presented in Figs. 6.1-7. They are discussed below. Each of the four data points which are normalized to the total number of proton counts are a weighted average of several measurements. The statistical error on each data point varies from 9-22 percent. The error bars are calculated with equation (5.5). Since typical proton counts are $\sim 10^9$ for each run, this incurs a statistical error $\sim 10^{-3}$ percent. Therefore, statistical errors due to the normalization by the total proton counts are not included in this calculation.

Finally, each of the observed transitions are shown in Fig. 6.8.

6A. COINCIDENCES AT $\phi=0^o$

In the following sections polarization data for H_2^+ oriented along the beam axis is presented and discussed for four proton center-of-mass energies.

6A.1 $\epsilon_+=0.06$ eV

Figure 6.1 shows the polarization plot for $H^+ + L_\alpha$ coincidences when the center-of-mass energy of the proton is 0.06 eV. This particular energy was chosen since it is near the central peak of the proton laboratory energy distribution (see Fig. 5.1). This means that the observed protons occur near the $2p\pi_u$-$3d\sigma_g$ crossing of H_2^+ at 2.5-3 times the equilibrium separation of the molecule (see Ch. 1). One could not pick the peak of

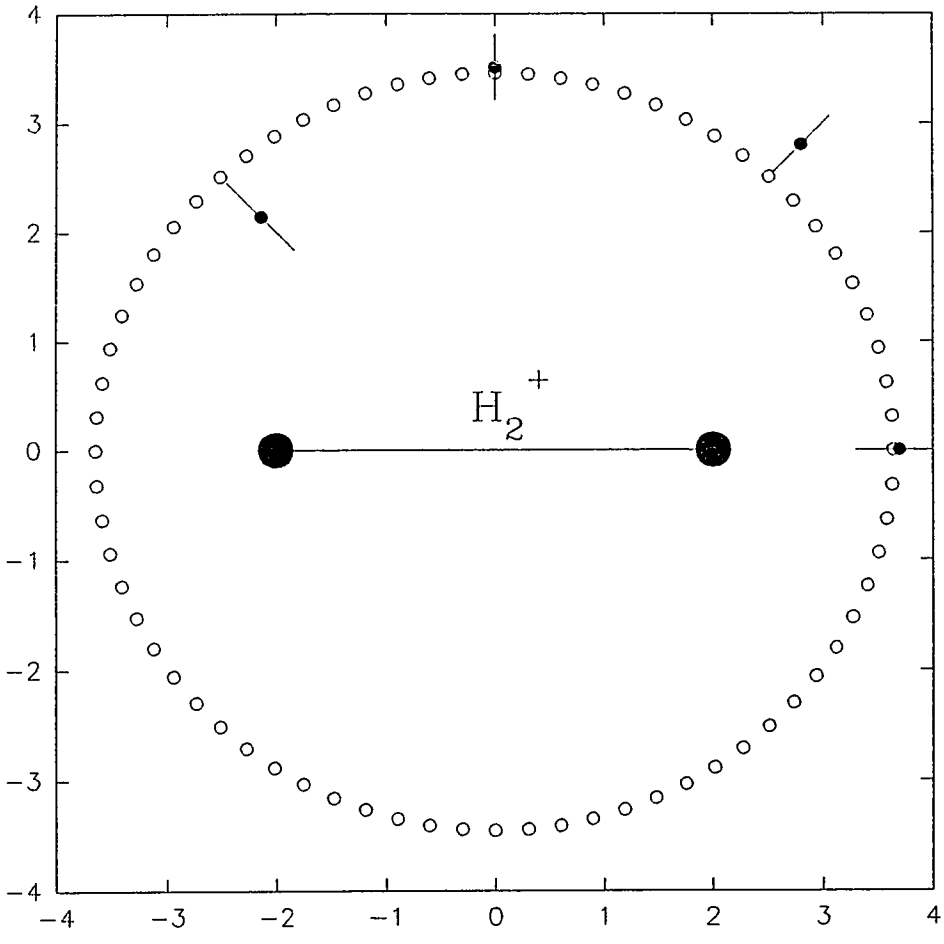

Figure 6.1: Polar plot of H^+-L_α coincidences for $\phi=0^\circ$ and $\varepsilon_+=0.06$ eV. The small filled circles represent the data. The open circles represent the fit to the data. In this case $P_1=0.027\pm0.097$ and $\sigma_0/\sigma_1=1.2\pm0.7$. Note that P_1 is written in the laboratory frame. The abscissa is parallel to the incident beam direction. The orientation of the molecule is also shown.

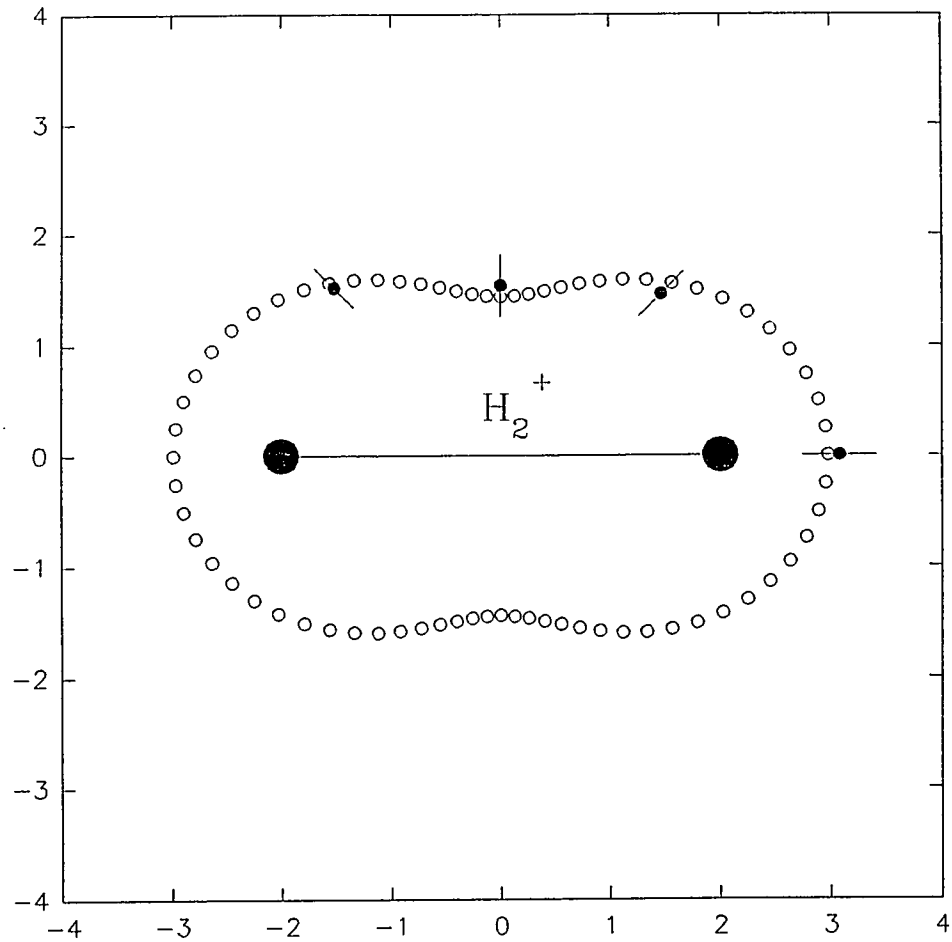

Figure 6.2: Polar plot of H^+-L_α coincidences for $\phi=0^\circ$ and $\varepsilon_+=0.78$ eV. The small filled circles represent the data. The open circles represent the fit to the data. In this case $P_1=0.348\pm0.066$ and $\sigma_0/\sigma_1=12.5\pm11.2$. Note that P_1 is written in the laboratory frame. The abscissa is parallel to the incident beam direction. The orientation of the molecule is also shown.

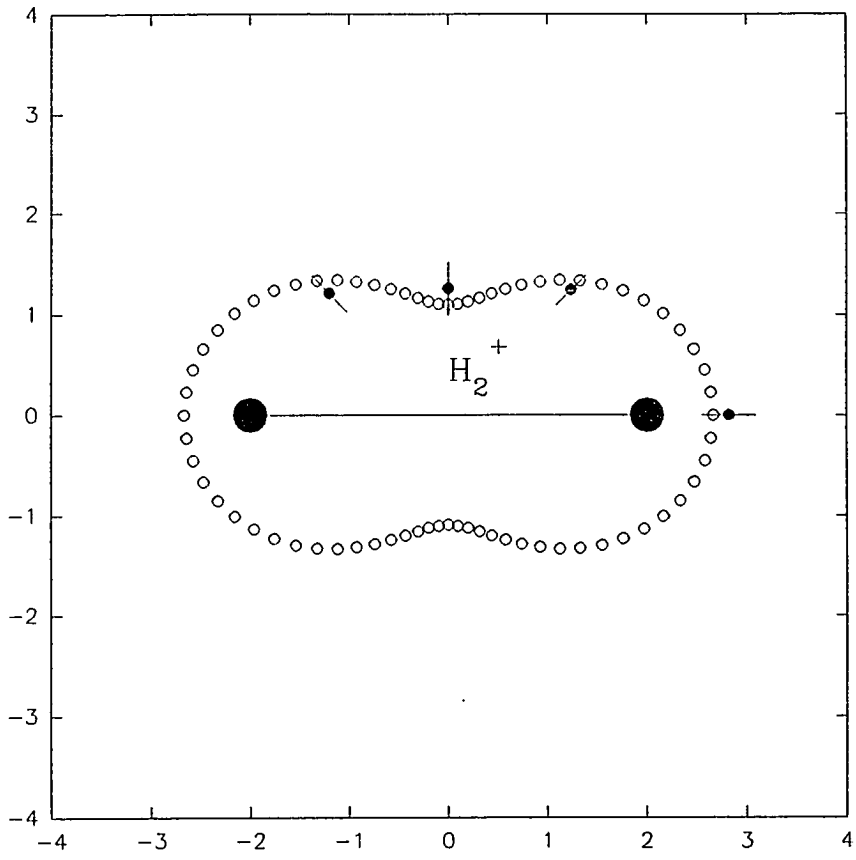

Figure 6.3: Polar plot of H^+-L_α coincidences for $\phi=0^\circ$ and $\varepsilon_+=1.2$ eV. The small filled circles represent the data. The open circles represent the fit to the data. In this case $P_1=0.418\pm0.123$ and $\sigma_0/\sigma_1=103\pm1331$. Note that P_1 is written in the laboratory frame. The abscissa is parallel to the incident beam direction. The orientation molecule is also shown.

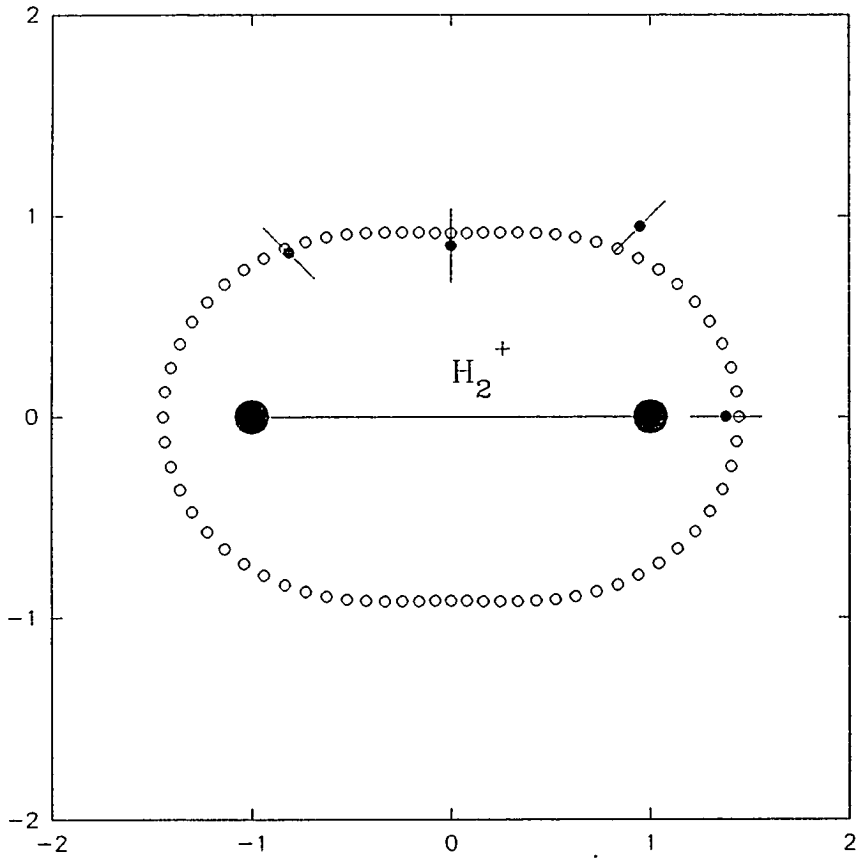

Figure 6.4: Polar plot of H^+-L_α coincidences for $\phi=0^\circ$ and $\varepsilon_+=2.8$ eV. The small filled circles represent the data. The open circles represent the fit to the data. In this case $P_1=0.225\pm0.099$ and $\sigma_0/\sigma_1=3.8\pm2.7$. Note that P_1 is written in the laboratory frame. The abscissa is parallel to the incident beam direction. The orientation molecule is also shown.

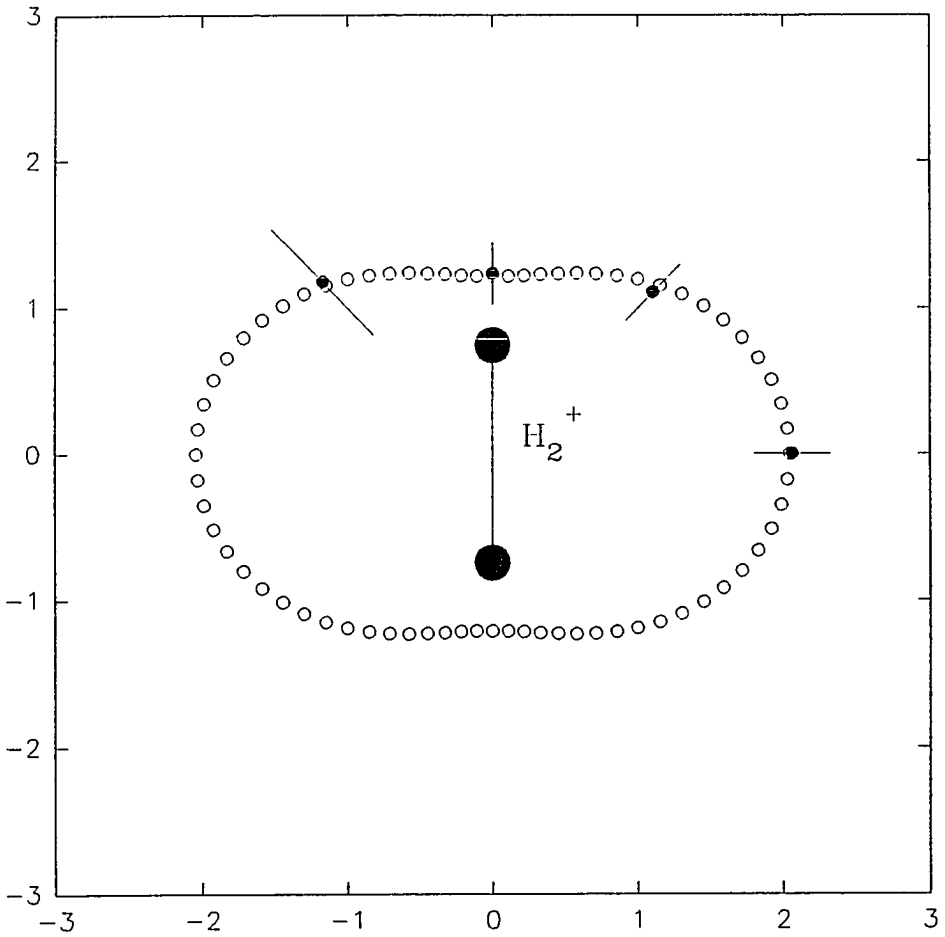

Figure 6.5: Polar plot of H^+-L_α coincidences for $\phi=90^\circ$ and $\varepsilon_+=2.20$ eV. The small filled circles represent the data. The open circles represent the fit to the data. In this case $P_1=0.255\pm0.031$ and $\sigma_0/\sigma_1=0.040\pm0.073$. Note that P_1 is written in the laboratory frame. The abscissa is parallel to the incident beam direction. The orientation of the molecule is also shown.

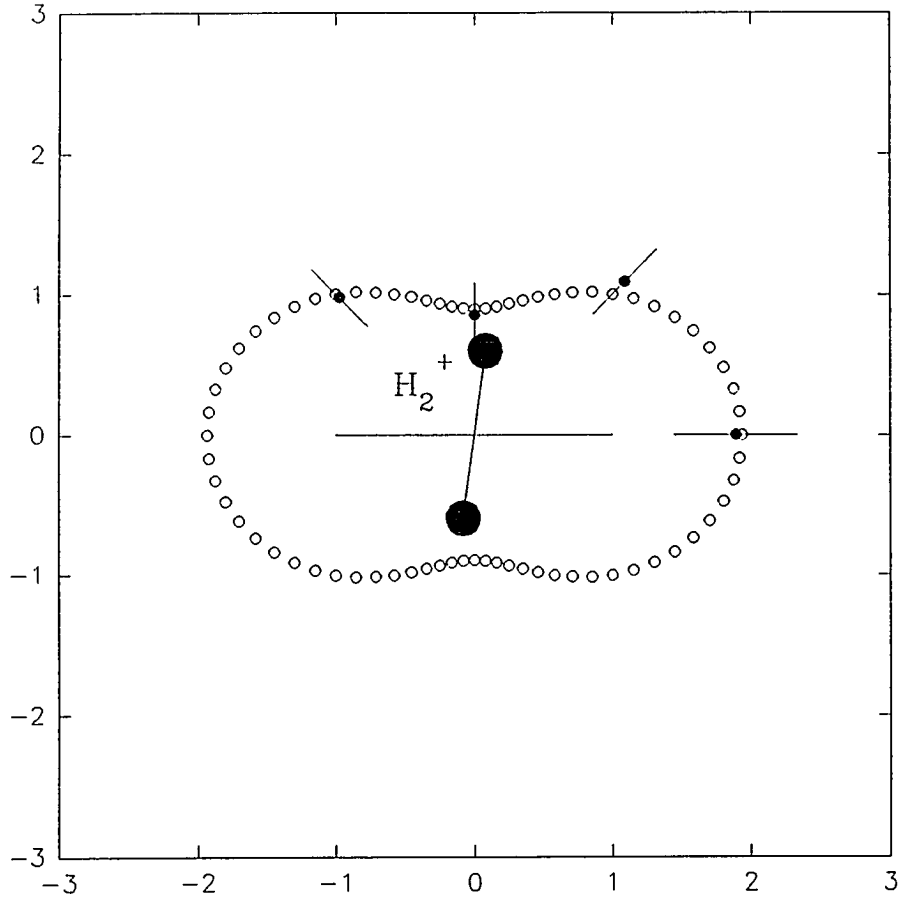

Figure 6.6: Polar plot of H^+-L_α coincidences for $\phi=83^0$ and $\varepsilon_+=2.80$ eV. The small filled circles represent the data. The open circles represent the fit to the data. In this case $P_1=0.367\pm0.073$ and $\sigma_0/\sigma_1=0.41\pm 0.40$. Note that P_1 is written in the laboratory frame. The abscissa is parallel to the incident beam direction. The orientation of the molecule is also shown.

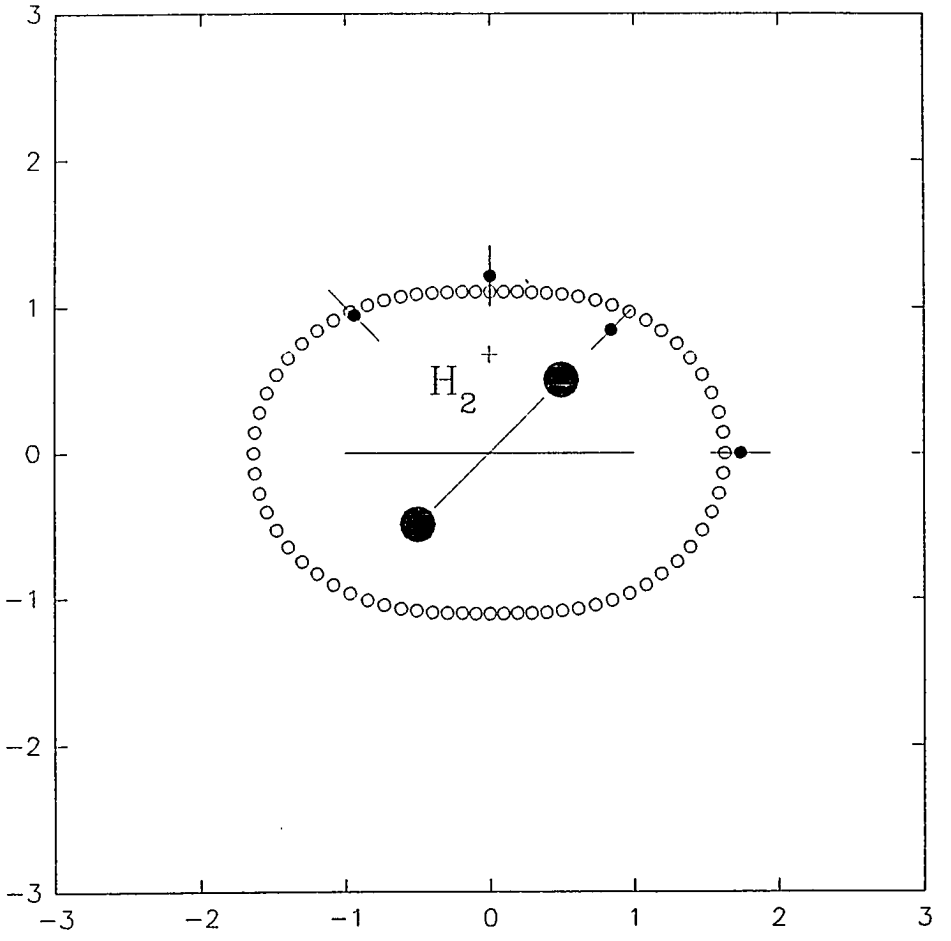

Figure 6.7: Polar plot of $H^+ - L_\alpha$ coincidences for $\phi=61^\circ$ and $\varepsilon_+=2.70$ eV. The small filled circles represent the data. The open circles represent the fit to the data. In this case $P_1=0.194\pm0.083$ and $\sigma_0/\sigma_1=5.2\pm3.3$. Note that P_1 is written in the laboratory frame. The abscissa is parallel to the incident beam direction. The orientation of the molecule is also shown.

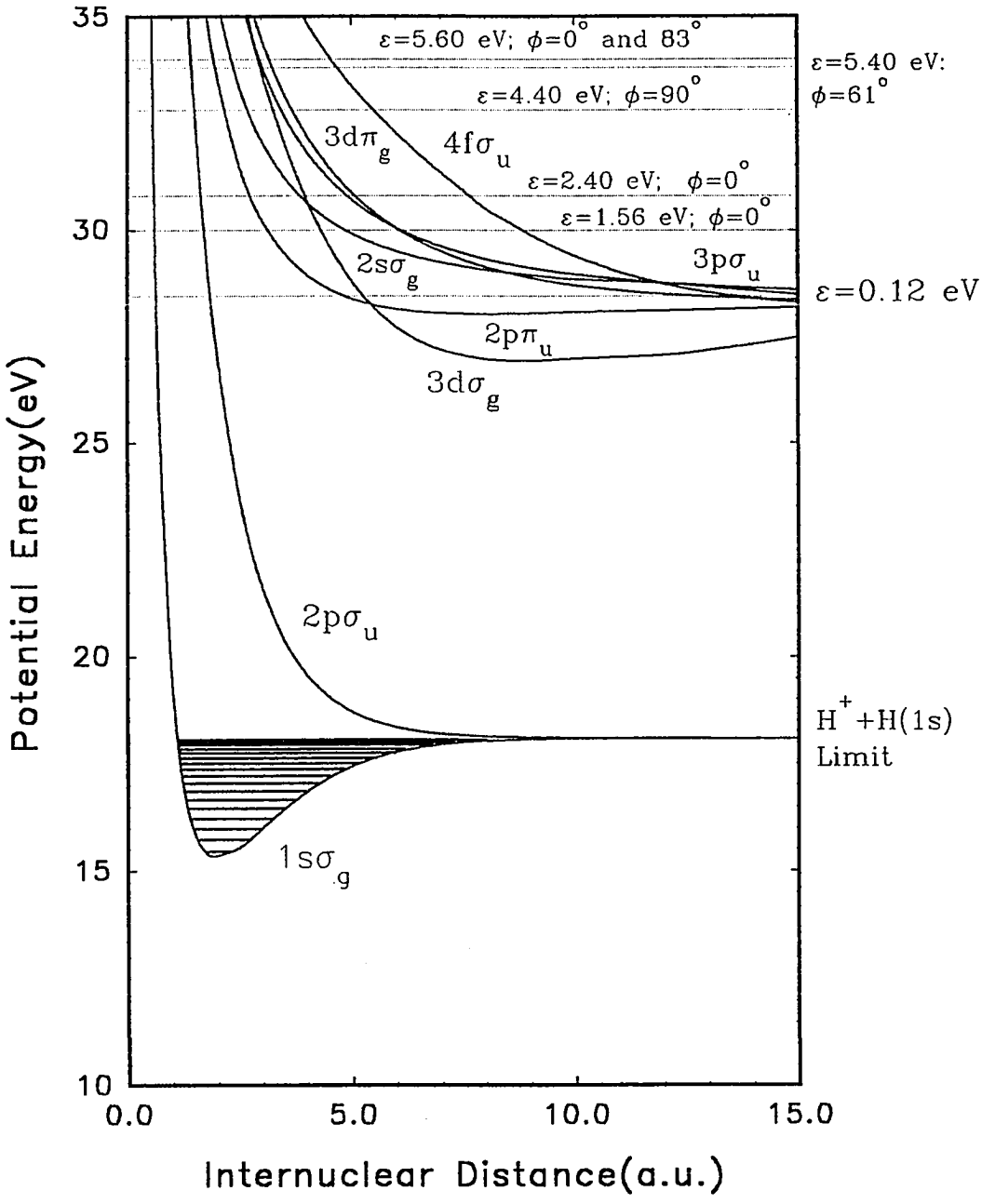

Figure 6.8: H_2^+ energy curves which show the center-of-mass energies of the protons observed in the present experiment. Data for the plots are obtained from Bates et al (1953), and Madsen and Peek (1971).

the laboratory energy distribution of the protons, since that would mean that all molecular orientations are accepted by the detector. As mentioned in Ch.4, the proton and photon detectors discussed by Yenen *et al* (1990) and Mueller (1982), respectively, are employed in this measurement. The proton detector electronics are very similar to the system described in Ch.4 Sect. C.3. The size of the anode pin was 0.06 in. in diameter. Therefore, the orientation of the internuclear axis relative to the beam axis is known to within $\pm 4.4°$. The small size of the proton detector coupled with a lower photon detection efficiency (Mueller's system used two 2 mm thick LiF crystals with a PMT having 7.5 percent quantum efficiency) increased the data accumulation time substantially. The entire data set was collected within three months.

The observed polar plot clearly shows that both $H(2p_0)$ and $H(2p_{\pm 1})$ contribute equally to the observed radiation. Although the results show that the electron charge cloud is not aligned along the beam axis, it does not contradict the hypothesis discussed in Sect. 3C.1 of Ch. 3. Recall that as the molecule dissociates into $H^+ + H(2p_0)$, Stark mixing causes the $m_l=0$ states of the n=2 level of H to become degenerate with equal contributions from H(2s) and $H(2p_0)$. Thus, the $3d\sigma_g$ state dissociates equally into $H^+ + H(2p_0)$ and $H^+ + H(2s)$. In order to obtain an equal amount of $H(2p_0)$ and $H(2p_{\pm 1})$, the $3d\sigma_g$ must contribute twice as much as the $2p\pi_u$ state to the observed protons. Thus, the electronic charge cloud associated with the molecule haHxa greater alignment than the observed charge cloud of the excited atom.

Figure 6.9 shows the charge cloud of the excited molecule for this process as a function of internuclear separation. Each plot in Fig. 6.9 is obtained by incoherently

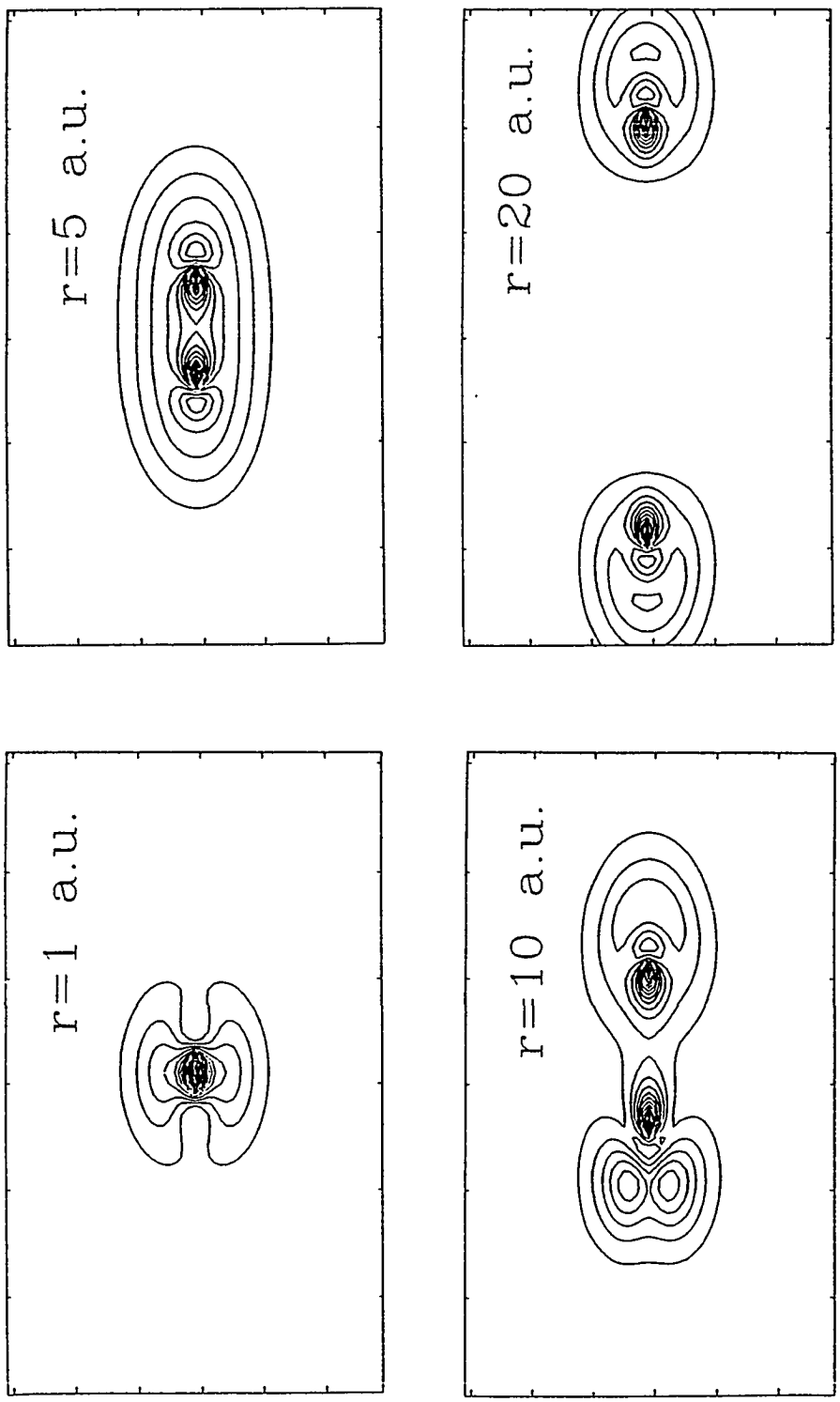

Figure 6.9: Shape of the electron charge cloud of excited H_2^+ when the molecule is aligned along the beam axis. In this case the contributions are an incoherent superposition of 1 part $2p\pi_u$ and 2 parts $3d\sigma_g$. Note the alignment of the charge cloud as a function of internuclear separation.

summing the contributions from the $2p\pi_u$ and $3d\sigma_g$ states. The molecular states are approximated by linear combinations of atomic orbitals (Fano and Fano 1970). One can conclude that the electronic charge cloud of the excited H_2^+ molecule will have a greater alignment than the nascent charge cloud of the neutral atom when σ-states contribute to an observed process.

6A.2 $\epsilon_+ = 0.78$ eV

The second set of data for this particular orientation are shown in Fig. 6.2. In this case the center-of-mass energy of the proton was 0.78 ± 0.27 eV. The internuclear orientation is known within $\pm 13.5°$. Data accumulation time was approximately two weeks for the entire data set. This decrease in accumulation time illustrates the increased efficiency of the new detector systems. It is clear from Fig. 6.8 that in this region only the $2p\pi_u$, $3d\sigma_g$, and $2s\sigma_g$ states can contribute to the observed process. The other states which can produce $H^+ + H(2p)$ at this center-of-mass energy seem unlikely since such transitions would occur at large internuclear separations and high vibrational states of the $1s\sigma_g$ orbital (see Fig. 2.2). The results show that $H(2p_0)$ is populated 13 times as much as $H(2p_{\pm 1})$. Thus, σ-states (by a factor of 26 because of Stark mixing; see above discussion) dominate the excitation process. From Fig. 1.1 one can estimate the inelastic energy loss Q of the process. For transitions to the $3d\sigma_g$ state, the inelastic energy loss is estimated to be $Q = 12.9$ eV where the initial vibrational state of the $1s\sigma_g$ orbital is $\nu = 7$. This vibrational state is chosen since the transition would occur at its classical turning point. However, it should be noted that transitions will also occur at other internuclear separations. If a transition occurs from the $1s\sigma_g$ state to the $2s\sigma_g$ state, then

the inelastic energy loss incurred in the process would be Q=12.4 eV where the initial vibrational state of the $1s\sigma_g$ orbital is $\nu=10$. Since $\nu=7$ state is more (by more than a factor of two) populated than the $\nu=10$ state, one can infer that the $3d\sigma_g$ gives the largest contribution to the observed process. To precisely determine which of these two molecular states contributes the greatest, one must perform an experiment where Q is measured very precisely. This might be possible if the two fragment particles and the emitted photon are all detected in coincidence. Any optical measurement between a photon and one fragment cannot distinguish between the two states, since they lead to the same m_l value.

6A.3 $\epsilon_+ = 1.20$ eV

Figure 6.3 shows the polarization data for $\epsilon_+ = 1.20 \pm 0.33$ eV. The internuclear orientation is known within $\pm 10.9°$. This value was chosen because it includes the $2s\sigma_g$-$3d\sigma_g$ crossing of the H_2^+ curves (see Fig. 1.1). The results show that the electron charge cloud is highly aligned along the beam axis. Thus, both states enhance $H^+ + H(2p_0)$ production. The value of P_1 is near the maximum allowed by atomic precession (see equation 3.14). The estimated inelastic energy loss for this process is 13.8 eV ($\nu=6$).

The cross-section ratio σ_0/σ_1 for this process is approximately 102. The error for this result is very large. This occurs because the denominator in equation (3.13) tends to zero very rapidly as the value of P_1 nears its maximum allowed value. Thus, the large error in σ_0/σ_1 is mathematical in nature. It does not negate the fact that the number of coincidences at $\alpha=0°$ is much greater than the number of coincidences at $\alpha=90°$.

6A.4 $\epsilon_+ = 2.8$ eV

The last set of data for this particular orientation are shown in Fig. 6.4. In this case $\epsilon_+ = 2.8 \pm 0.56$ eV and $\phi = 0° \pm 7.2°$. The fit shows that $P_1 = 0.225 \pm 0.07$. This means that the electron charge cloud is slightly aligned along the beam axis. Since the ratio of σ_0/σ_1 is much smaller than the previous two cases, the contributions from the π_x molecular states become more significant. From Fig. 1.1, one can see that all six states can contribute to the observed protons. Contributions from the $4f\sigma_u$ state are considered to be small, since this transition would occur at very large internuclear separations. Note that in the present case the $3d\sigma_g$ and $3p\sigma_u$ states cross. The $3d\pi_g$ is almost degenerate with these two states. Transitions to these states would originate from the classical turning points of the $v=3,4$ vibrational states of the $1s\sigma_g$ orbital. Since these transitions are the only processes which originate from classical turning points of the ground vibrational states, it would seem fair to say that these three states contribute the greatest to the observed protons (recall that transitions can occur at other internuclear separations). However, contributions from the $2p\pi_u$ and $2s\sigma_g$ are also significant. Again, a more precise measurement of the relative contributions would require a very precise measurement of Q.

6B. COINCIDENCES AT $\phi = 90°$

6B.1 $\epsilon_+ = 2.20$ eV

Figure 6.5 shows the polarization data for $\phi = 90° \pm 12.4°$ and $\epsilon_+ = 2.20 \pm 0.65$ eV. In this case the laboratory scattering angle is 1.88° (see caption of Fig.5.3). Again, the

electron cloud is aligned along the beam axis. However, the quantization axis is perpendicular to the beam axis. The cross section ratio shows that π molecular states clearly dominate the excitation process. The only such states are $3d\pi_g$ and $2p\pi_u$ orbitals. If one applies the logic that Franck-Condon transitions from classical turning points are most probable, it would seem that the $3d\pi_g$ ($\nu=5$) state gives the largest contributions of two π-states, since this is the only transition which can originate from a classical turning point.

6C. OTHER MOLECULAR ORIENTATIONS

6C.1 $\epsilon_+ = 2.8$ eV

Figure 6.6 shows the polarization data for $\phi=83°\pm8.7°$ and $\epsilon_+=2.8\pm0.85$ eV. In this case the laboratory scattering angle is 2.12° (see caption of Fig.5.2). The electron cloud is aligned along the beam axis. However, the quantization axis is nearly perpendicular to the beam axis. Again, the cross section ratio shows that π molecular states clearly dominate the excitation process. The only such states are $3d\pi_g$ and $2p\pi_u$ orbitals. If one applies the logic that Franck-Condon transitions from classical turning points are most probable, it would seem that the $3d\pi_g$ ($\nu=4$) state gives the largest contributions of two π-states.

6C.2 $\epsilon_+ = 2.70$ eV

The last set of data (Fig.6.7) shows the observed polarization for protons of energy 2.70 ± 1.10 eV in the center-of-mass, emanating from H_2^+ oriented at $61°\pm11.7°$ relative to the incident beam axis. The cross section ratio shows that the dominant

contributions in this process come from σ-states. From Fig. 6.8 the dominant contributions come from the $2s\sigma_g$ and $3d\sigma_g$ molecular states.

6D. DISCUSSION

Two mechanisms which are used to qualitatively describe excitation processes through correlation diagrams are rotational (Coriolis) and translational coupling (Bates and McCarroll 1962 and Heinrich 1968). However, in atom-diatom collisions these two mechanisms are viewed in a different manner as opposed to the atom (ion)-atom case.

In atom-atom collisions, rotational coupling arises when the electron cloud of the system cannot perfectly follow the rotation of the internuclear axis formed by the two atomic constituents participating in the collision process. As the rate of rotation of the internuclear axis increases, the coupling mechanism becomes stronger. The coupling strength is greatest at small distances of approach. This mechanism leads to σ to π and π to σ transitions of the temporary molecule.

However, in atom-diatom collisions, Sidis and Dowek (1984) have prescribed that this mechanism arises when the electon cloud of the complex lags behind the rotation of the plane containing the three nuclei of the atom-diatom complex (see Fig. 6.10). Again, this coupling mechanism is strongest at small distances of approach. Sidis and Dowek (1984) further explain that transitions will occur between closely lying states which are symmetric and anti-symmetric with respect to the plane containing the nuclei.

In atom-atom collisions, the second mechanism, translational coupling is due to the electron cloud's inability to cope with sudden changes of the internuclear separation of the two atom system. This leads to excitation of states (of the temporary molecule) of

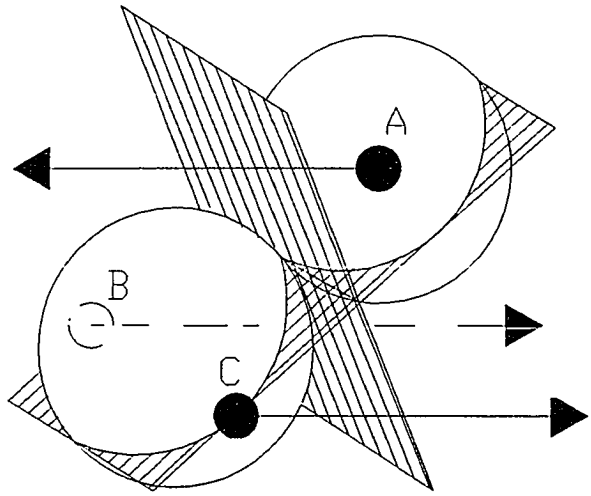

Figure 6.10: Rotational coupling for a triatom system (from Sidis and Dowek 1984). This is illustrated by the two positions of the plane containing the three nuclei at two instants of the encounter. The coupling is greatest at close distances of approach.

the same symmetry. In atom-diatom collisions, this mechanism is attributed to variations of the nuclear coordinates within the plane containing the three nuclei (Sidis and Dowek 1984). This mechanism is responsible for transitions to states of the same symmetry.

Both of these mechanisms are qualitatively distinguished through the quasidiatomic and triatomic schemes described in Ch. 2. Therefore, it is appropriate at this point to attempt to discuss the experimental results in terms of these models.

It has been stated in Ch. 2 Sect. 2D that the present experiment will severely test the quasidiatomic model. For each of the processes observed in this work, the data suggest that the charge cloud of $(H_2^+)^*$ is aligned parallel to the incident beam velocity. This agrees very well with the prediction of Jaecks *et al* (1983) which stated that the dominant excited $(H_2^+)^*$ state for this particular collision complex will be aligned along the beam axis. From their observations, Jaecks *et al* (1983) concluded that, at distances of closest approach, when the internuclear axis of H_2^+ is nearly perpendicular to the beam axis, rotational coupling produces a final π-like state quasidiatomic state. As the excited H_2^+ recedes from the target, it is assumed that this excited state remains "frozen or locked" onto the molecule's internuclear axis. It is this assumption that enables one to apply the quasidiatomic model to this collision complex. For arbitrary orientations of the internuclear axis, the final quasidiatomic state is a linear combination of σ-like and π-like states and still remains secured to the alignment produced at distances of closest approach. Once the alignment of the molecular charge cloud is determined by the collision dynamics, the excited states of H_2^+ are determined from the orientation of its internuclear axis relative to the incident beam velocity. Thus, Jaecks *et al* (1983)

concluded that the $2p\pi_u$ state should be the dominant excitation channel when the molecular ion is oriented perpendicular to the incident beam direction, while the $2p\sigma_u$ state dominates when the molecular ion is oriented along the beam axis. The data shown in Fig. 6.5 where the $2p\pi_u$ state contributes significantly to the observed protons agree very well with this statement, since the molecular ion's excitation can be easily described by the rotational coupling between the $2pq\sigma$ and the $2pq\pi$ quasidiatomic states. However, details of the other processes observed in this work require knowledge of the transitions from the $2pq\pi$ state to higher lying states. One should also note that this model works well for transitions which occur at small internuclear separations of H_2^+. However, as stated in Ch. 2 Sect. 2D, this model might not be applicable for transitions which occur at large internuclear separations of H_2^+. As will be shown below, the details of the transitions remain sketchy.

Since six states produce the $H^+ + H(2p)$ channels, one needs to include all of these channels in Fig. 2.6. One can easily draw the missing channels which emanate from the higher lying orbitals of the united atom limit. However, because of the uncertainty principle, the levels at the separation limit are known to within a few eV. This is the reason for the gray box in Fig. 2.6.

Consider the $3d\sigma_g$ state of H_2^+ which contributed significantly to all of the observed processes at $\phi=0°$. Because of the uncertainty principle, this state could be correlated to the 3d, 4f, or 5g united atom limit. This is also true for the $2s\sigma_g$ state. Thus, excitation mechanisms are very difficult to qualitatively assess unless one performs a calculation for the $(HeH_2)^+$ complex within the quasidiatomic model. On the other

hand, it is obvious that if excitation to any of the six channels is to occur, this model suggests that the $2pq\sigma$ and $2pq\pi$ quasidiatomic states (shown in Fig. 2.6) must rotationally couple.

Finally, because of its simplicity, the quasidiatomic model does not allow one to predict processes which occur at specific internuclear separations (and thus fragment energies) of the diatom. Thus, one needs a more complex model in order to better evaluate the mechanisms for the processes observed in this work.

A more complex model, namely, the triatomic model of Dowek *et al* (1982) was briefly discussed in Ch. 2 Sect. 2C. The construction of a cubic correlation diagram which includes the six channels producing $H^+ + H(2p)$ would involve at least eight interwoven potential energy surfaces (this includes the excited states of H_2^+ which produce L_α and the states producing neutral H in the ground state) for each molecular orientation studied. This would make the excitation mechanisms extremely difficult to evaluate. If one wants to interpret the results of this work in terms of cylindrical correlation diagrams, one must construct a diagram for each observed r (see Fig. 2.5). However, in this case, the visual interpolation of the potential energy surfaces from the $C_{\infty v}$ to C_{2v} conformations would require a great deal of intuition about the $(HeH_2)^+$ complex. One needs to understand the results of some theoretical investigations involving this system in order to develop this intuition.

Because of the lack of theoretical work on the $(HeH_2)^+$ complex one needs to develop a very simple approach in order to gain further understanding of this system. This type of approach was implemented in Ch. 3 Sect. 3C.1. From symmetry arguments,

it was shown that σ-states will always dominate in the production of $H^+ + H(2p)$ from the six aforementioned dissociative channels of H_2^+, when the instantaneous orientation of the molecule is parallel to the incident beam velocity. This agrees very well with the results presented in Sects. 6A.1-4.

On the other hand, it was shown that only two symmetry planes (Fig. 3.7) exist when the instantaneous orientation of the molecule is perpendicular to the incident beam velocity. In these two cases, π-states were said to dominate. This seems to agree with the results of Fig. 6.5. However, because the detector accepts a finite range of H_2^+ internuclear orientations, one cannot use this symmetry argument unless one knows that all acceptable orientations of H_2^+ correspond to conformations which are near to those shown in Fig. 3.7.

Finally, because of lack of symmetry, the results of Figs. 6.6 and 6.7 cannot be understood in terms of these arguments. In these cases one needs the results of a theoretical investigation.

6E. EPILOGUE

The alignment measurements performed in this work will easily test the results of any theoretical investigation involving the production of L_α from H_2^+. However, in some cases a very precise measurement of Q could become very important (see Sect 6A.2). In such a case one would need to perform a triple coincidence measurement between the fragments and the L_α photon. With the implementation of wedge-and-strip anodes to detect the fragments (Siegmund *et al* 1986), one could not only precisely determine the center-of-mass deflection of H_2^+, but also precisely determine all the

kinematic parameters associated with each fragment particle.

The triple coincidence measurement applied in this fashion could also determine the of the relationship between the angular distribution of the dissociation products and the degree of polarization of the excited atomic fragments. Van Brunt and Zare (1968) have shown that the anisotropic fluorescence from excited atomic fragments occur if the spatial distribution of the dissociation products is anisotropic and if there is preferred population of the magnetic sublevels of the atomic fragment. Their work also relates the anisotropy of the electron charge cloud to the anisotropy of the dissociation fragments.

APPENDIX A

COLLISION CHAMBER DETAILS

A.1 PHOTON DETECTION SYSTEM INFORMATION

This section presents details of the photon detection system discussed in Ch.4. A close up drawing of the photon detection system are shown in Figs. A.1-2. The next section presents some important dimensions not shown in Fig. A.1.

The entire system moves around its rotation axis. This is done by manually applying a force which is perpendicular to the direction of the rotation lever and the plane of Fig. A.1. The shaft support, flanges, and shaft are made by machined stainless steel. In Fig. A.1, they are denoted by the hatched regions. The block containing the PMT, LiF holder, and apertures is made from machined aluminum. In Fig. A.1, this is denoted by the cross-hatched region. The vernier shown in the figure is made of machined brass.

The top 0.500" of the 1.500" shaft (not shown in Fig A.1 for clarity) is threaded for two machined brass bolts. This forms the suspension mechanism of the entire apparatus.

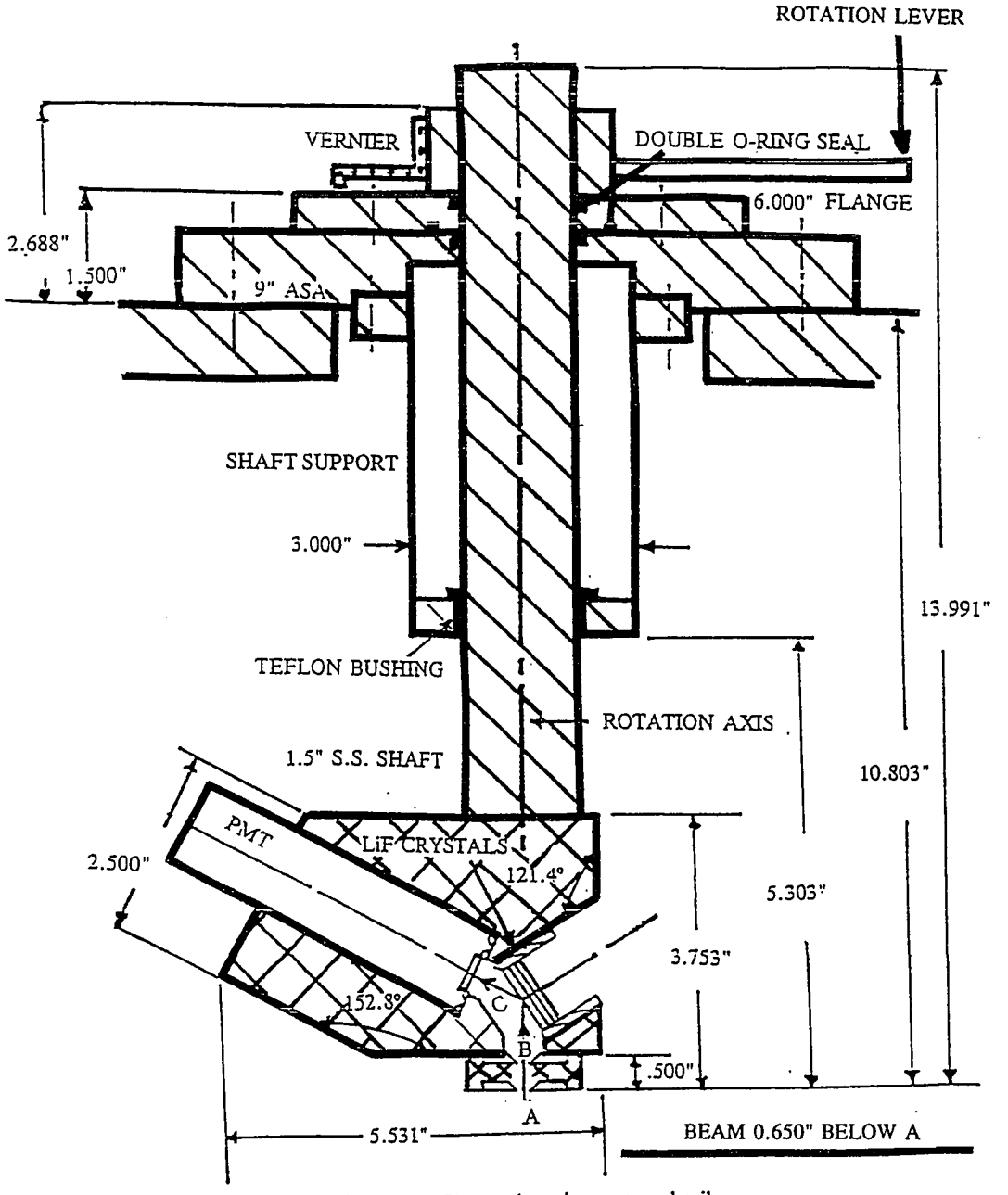

Figure A.1: Photon detection system details.

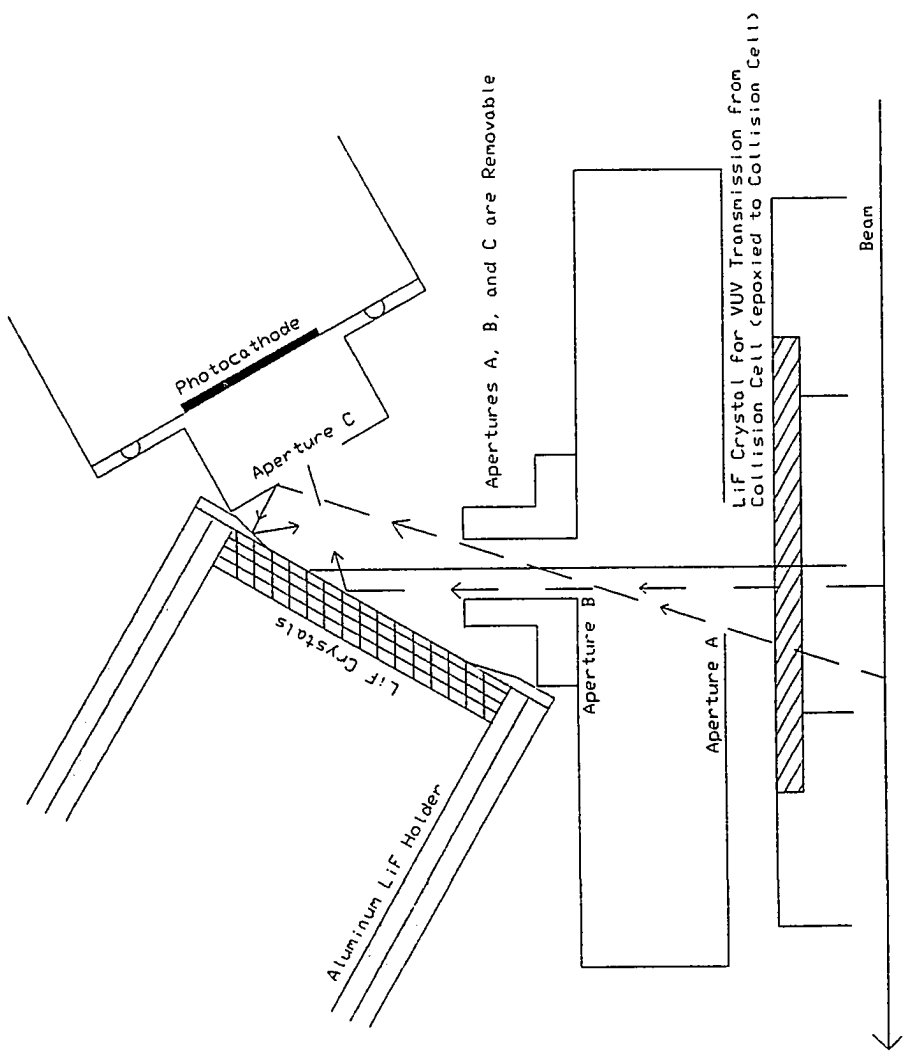

Figure A.2: Expanded view of the photon detection system apertures. Two typical light rays are shown; one which is accepted by the PMT and one which is not accepted by it.

A.2 PHOTON DETECTION SYSTEM DIMENSIONS

Distance from c.c. to 1st aperture*	0.650±0.005
Distance from c.c. to 2nd aperture	1.556±0.005
Distance form c.c. to 1st crystal	1.806±0.005
Distance from 1st crystal to PMT	0.765±0.005
Diameter of 1st aperture (A)	0.250±0.001
Diameter of 2nd aperture (B)	0.125±0.001
Diameter of PMT aperture (C)	0.250±0.001
Acceptance angle between (A) and (B)	22.0°
Acceptance angle between (A) and (C)	9.10°
Diameter of PMT	1.260±0.002
Outer diameter of LiF holder	1.250±0.002

*All length measurements are in inches

A.3 COLLISION CELL AND FARADAY CUP DETAILS

This section presents details of the apparatus discussed in Ch.4 Sect. B.1 and B.2. A close up view of the collision cell and beam monitoring system is shown in Fig. A.3. The chamber base, deflection plates, collision cell housing, and collision cell, are made from machined stainless steel. In Fig. A.3 they are denoted by the hatched regions. All

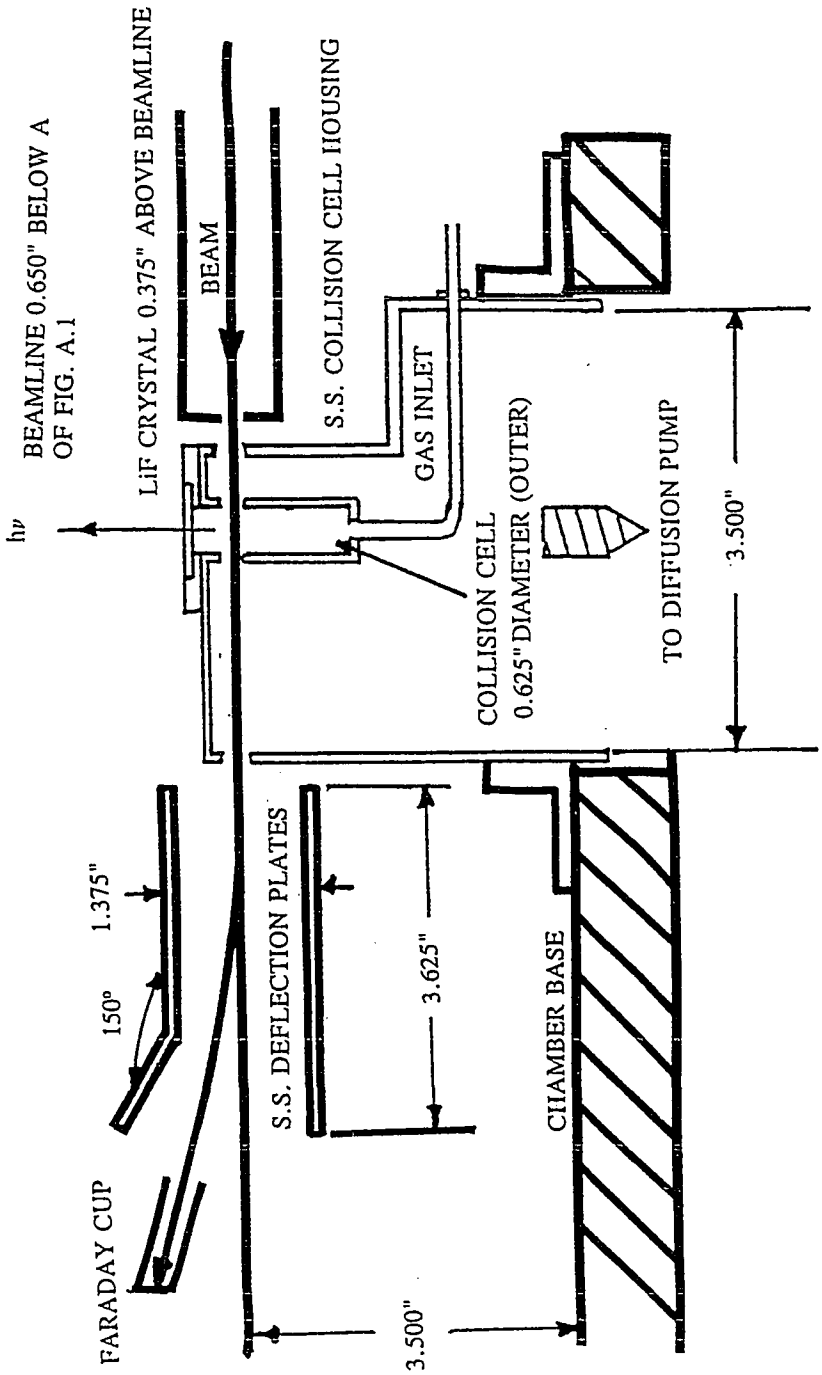

Figure A.3: Collision cell and beam monitoring system details.

pertinent dimensions are shown in the figure.

APPENDIX B

REFLECTIVTY CALCULATIONS

In this section the method of calculating the reflectivities parallel and perpendicular to the plane of incidence for a pile of plates is presented.

For one plate and one reflection the reflectance parallel and perpendicular to the plane of incidence are (Hecht and Zajac 1979)

$$\rho_{\perp} = \frac{\sin^2(\theta_i - \theta_t)}{\sin^2(\theta_i + \theta_t)} \qquad \text{(B.1)}$$

and

$$\rho_{\parallel} = \frac{\tan^2(\theta_i - \theta_t)}{\tan^2(\theta_i + \theta_t)}, \qquad \text{(B.2)}$$

where θ_i and θ_t are the angle of incidence and angle of refraction, respectively.

If the contributions from multiple reflections are included in the calculation, the reflectance perpendicular to the plane of incidence becomes

$$r_{\perp} = \frac{2\rho_{\perp}^{2}g^{2}(1-\cos\delta)}{(1+\rho_{\perp}^{4}g^{4})-2\rho_{\perp}^{2}g^{2}\cos\delta} \qquad \text{(B.3)}$$

where δ is the phase between the incident wave and reflected wave, and $g=e^{-\mu d\sec(\theta)}$ (Stokes 1862 and MacLeod 1969). The latter quantity (as described in ch.4 sect. B.3) describes the loss of light as it travels through the medium. Hecht and Zajac (1979) also show how to calculate the transmittance in a similar fashion.

The quantity δ depends on the thickness of the crystal and the wavelength of the electromagnetic radiation. Because the thickness of the LiF plate (and its variation in flatness) is much much greater than the observed wavelength, fringes will be too dense to be detected by the present detection system. Therefore, the average of equation (B.3) is used. This means that the intensities parallel and perpendicular to the plane of incidence represent an incoherent sum of multiply reflected and transmitted electric fields which are parallel and perpendicular to the plane of incidence, respectively. Thus, one can write the reflectance and transmittance perpendicular and parallel to the plane of incidence as

$$r_{\perp} = \rho_{\perp} + \frac{(1-\rho_{\perp})^{2}\rho_{\perp}g^{2}}{1-\rho_{\perp}^{2}g^{2}}, \qquad \text{(B.4)}$$

$$r_{\parallel} = \rho_{\parallel} + \frac{(1-\rho_{\parallel})^2 \rho_{\parallel} g^2}{1-\rho_{\parallel}^2 g^2}, \qquad \text{(B.5)}$$

$$t_{\perp} = \frac{(1-\rho_{\perp})^2 g}{1-\rho_{\perp}^2 g^2}, \qquad \text{(B.6)}$$

$$t_{\parallel} = \frac{(1-\rho_{\parallel})^2 g}{1-\rho_{\parallel}^2 g^2}, \qquad \text{(B.7)}$$

respectively.

Now, if more than one plate is used the situation is further complicated. The reflectance perpendicular and parallel to the plane of incidence was first derived by Stokes (1862). His results are presented here. If m is the number of plates in the pile, and if the quantities the reflectivities are written as

$$R_{\perp} = \frac{b_{\perp}^{m} - b_{\perp}^{-m}}{a_{\perp} b_{\perp}^{m} - a_{\perp}^{-1} b_{\perp}^{-m}} \qquad \text{(B.8)}$$

and

$$R_{\parallel} = \frac{b_{\parallel}^{m} - b_{\parallel}^{-1}}{a_{\parallel} b_{\parallel}^{m} - a_{\parallel}^{-1} b_{\parallel}^{-m}}, \qquad \text{(B.9)}$$

where

$$a_{\perp} = \frac{1}{2r_{\perp}} (1 + r_{\perp}^{2} - t_{\perp}^{2} + \Delta_{\perp}), \qquad \text{(B.10)}$$

$$a_{\parallel} = \frac{1}{2r_{\parallel}} (1 + r_{\parallel}^{2} - t_{\parallel}^{2} + \Delta_{\parallel}), \qquad \text{(B.11)}$$

$$b_{\perp} = \frac{1}{2t_{\perp}} (1 + t_{\perp}^{2} - r_{\perp}^{2} + \Delta_{\perp}), \qquad \text{(B.12)}$$

$$b_{\parallel} = \frac{1}{2t_{\parallel}} (1 + t_{\parallel}^{2} - r_{\parallel}^{2} + \Delta_{\parallel}), \qquad \text{(B.13)}$$

$$\Delta_{\perp} = \sqrt{(1 + r_{\perp} + t_{\perp})(1 + r_{\perp} - t_{\perp})(1 - r_{\perp} + t_{\perp})(1 - r_{\perp} - t_{\perp})}, \qquad \text{(B.14)}$$

and

$$\Delta_{\|} = \sqrt{(1+r_{\|}+t_{\|})\,(1+r_{\|}-t_{\|})\,(1-r_{\|}+t_{\|})\,(1-r_{\|}-t_{\|})}\,. \quad \text{(B.15)}$$

As previously mentioned $\mu=0.230$ and the index of refraction for 121.6 nm light is 1.64. The angle of incidence is 58° 38'. The angle of refraction (transmission angle) is easily calculated from Snell's law.

The calculation is easily performed in Lotus 2.1. Figures 4.4-4.9 were obtained with Sigmaplot 5.0.

APPENDIX C

H_2^+ KINEMATICS

C.1 TRAJECTORY CALCULATIONS FOR THE PROTON DETECTOR

Consider the geometry of the analyzer shown in Fig. 4.3. The quantity, r=QR, is the distance form c.c. to the entrance slit. On the other hand, rsin(45°) is the projection of the distance from the c.c. to the entrance onto the front plate (23.510 in.). Unless otherwise stated, the notation of Ch. 4 Sect. C.2 will be used throughout. Recalling from equation (4.2b) that $\gamma = \arcsin(\cos\theta_1 \sin\alpha)$ the distance PS is given by

$$\overline{PS} = r\sqrt{0.5+\tan^2\theta_1}\,. \qquad (C.1)$$

The total distance from the point S to a point on the detector is

$$L = [R + r\sqrt{(0.5+\tan^2\theta_1)}]\,. \qquad (C.2)$$

Thus, the x and z coordinates are

$$x = L\cos(\tan^{-1}(\sqrt{2}\tan\theta_1)) - r\sin\alpha \qquad (C.3)$$

and

$$z = L\sin(\tan^{-1}(\sqrt{2}\tan\theta_1)) . \qquad (C.4)$$

However, if the anode of the detector is receded behind the front plate, the total range becomes R'=R+ncot(γ), where n is the distance the anode is recessed behind the front plate.

To complete the calculation some equations on the kinematics of H_2^+ dissociation must be presented. To do this, one must recall Fig. 2.3 and equation (2.2). From Fig. 2.3 the laboratory scattering angle is written as

$$\sin\theta_1 = \sqrt{\frac{V_+}{V_+}}\sin\phi = \sqrt{\frac{\epsilon_+}{E_+}}\sin\phi . \qquad (C.5)$$

Using the values of Q and ϵ_+ given in the text for $\Delta\phi$=5°, the trajectories can be easily calculated. Fig. 4.15 shows the trajectories in question plus some others to give the reader a flavor for the trajectories of the protons. The section below presents the positions of the anodes for the present experiment.

C.2 RESULTS OF CALCULATION

RANGE (in.)	LAB ANGLE θ (deg.)	$\Delta\theta$ (deg.)	ENERGY RES.(FWHM %)
21.001	0.00	0.26	0.48
20.756	0.00	0.24	0.41
20.397	$\pm$2.12	0.32	1.00
20.224	$\pm$1.88	0.28	0.90
18.943	3.12	0.12	1.30
18.940	2.75	0.11	1.12
17.487	2.29	0.34	1.28
17.654	2.02	0.30	1.07
16.885	0.00	0.30	0.59
17.122	0.00	0.26	0.50
19.001	0.00	0.03	0.37

Note that the $\pm$ refers to the fact that there are anodes to the left and right of the beam axis. For the Qs and ϵs mentioned in the text, this corresponds to $\phi = \pm 45°$ in the center-of-mass. The large scattering angles would correspond to $\phi = 90°$, for the Qs and ϵs mentioned in the text.

C.3 CALCULATION OF ϵ_+ AND ϕ

When an H_2^+ dissociates along the beam axis, the inelastic energy loss Q of the proton's laboratory velocity spectrum can be easily determined. The energy of the

particles at the central peak is $E=(E_o-Q)/2$, since the center-of-mass energy of the protons is zero (refer to equation 2.2 and Fig. 5.1). If the analyzer voltage at the central peak is known, and if the analyzer constant and molecule's initial energy is known, then Q is easily calculated (Jaecks *et al* 1990 and Yenen *et al* 1990).

Away from the central peak of Fig. 5.1, ϵ_+ is not zero. One needs a way to estimate this. From Fig. 2.3, the laboratory velocity of a particle with center-of-mass velocity v is written as

$$\vec{V}_1 = \vec{V}_o + \vec{v}. \qquad (C.6)$$

Solving for v and squaring, one obtains

$$v^2 = V_o^2 + V_1^2 - 2V_oV_1. \qquad (C.7a)$$

By multiplying on both sides by the mass of the proton one obtains the center of mass energy of the proton,

$$\epsilon_+ = \frac{1}{2}mv^2 = E + E_1 - 2\sqrt{EE_1}. \qquad (C.8a)$$

However, it is more difficult to determine the center-of-mass energy and internuclear orientation relative to the beam axis from a proton distribution for particles scattered at non-zero angles. Therefore one must attempt to estimate the center-of-mass energy of particles scattered at non-zero angles. Consider the energy distribution shown

in Fig.5.3 (note θ=1.88). Its only peak occurs at 1392 V. Assume now that a detector is placed at zero degrees so that the central peak of the proton's laboratory energy spectrum occurs at 1392 V. The velocity of the particle corresponds to the velocity of the H_2^+ center-of-mass after excitation (see Fig. 2.2). The inelastic energy loss Q is of course 11.6 eV. For the particle scattered at θ=1.88°, its velocity is

$$\vec{V}_1 = \vec{V}_o + \vec{v}. \qquad (C.6)$$

Solving for v and squaring, one obtains

$$v^2 = V_o^2 + V_1^2 - 2V_oV_1\cos\theta_1. \qquad (C.7b)$$

In this case the angle between V_1 and V_o is not zero. Again by multiplying on both sides by the mass of the proton one obtains the center of mass energy of the proton,

$$\epsilon_+ = \frac{1}{2}mv^2 = E + E_1 - 2\sqrt{EE_1}\cos\theta_1. \qquad (C.8b)$$

Thus, if the analyzer constant for the trajectory is known, the center of mass can be easily calculated. This is just the generalized form of equation (C.8a). With this equation it is now possible to estimate the center-of-mass energy of the proton for any point on the laboratory energy distribution.

Using standard error analysis techniques the uncertainty in ϵ is

$$\Delta\epsilon_+ = [(1-\sqrt{\frac{E}{E_1}}\cos\theta_1)^2(\Delta E_1)^2+(1-\sqrt{\frac{E_1}{E}}\cos\theta_1)^2(\Delta E)^2 +4EE_1\sin^2\theta_1(\Delta\theta_1)^2]^{\frac{1}{2}} \quad (C.9)$$

where the Δs represent the uncertainties in the measured quantities. The largest contribution to this quantity comes from the last term.

Since all the quantities in equation (C.6) are known, one can easily determine the internuclear orientation relative to the beam axis. Note that this is the instantaneous orientation just before the molecule dissociates. First, one must solve equation (C.6) for one of the other variables; then square it, multiply by one-half the proton mass, and solve for ϕ. After rearrangement, one obtains

$$\phi = \arccos\left[\frac{E_1-E-\epsilon_+}{2\sqrt{E_1\epsilon_+}}\right]. \quad (C.10)$$

Because the equation for $\Delta\phi$ is extremely cumbersome, it will not be presented here. Using standard error analysis techniques, one can calculate this quantity with software program Derive.

C.4 MORE KINEMATIC EQUATIONS

In this section some other equations for H_2^+ dissociation kinematics are presented

(refer to Fig. 2.3). For the sake of brevity the equations will not be derived.

One can relate the velocity components along the beam axis. One possibility is

$$V_1\cos\theta_1 = V_o + v\cos\phi . \qquad (C.10)$$

In terms of the neutral scattered particles with velocity V_2 and laboratory angle θ_2 one obtains

$$V_o = \frac{V_1\cos\theta_1 + V_2\cos\theta_2}{2} \qquad (C.11)$$

or

$$v\cos\phi = \frac{V_1\cos\theta_1 - V_2\cos\theta_2}{2} . \qquad (C.12)$$

One can also calculate the orientation of the molecule in the center-of-mass. Solving for ϕ, one obtains

$$\tan\phi = \frac{2\sin\theta_1}{\cos\theta_2 - \sin\theta_1\cot\theta_2} . \qquad (C.13)$$

In a two particle coincidence experiment between the proton and the hydrogen atom, one can determine most of the kinematics of both particles. However, knowledge of polarized

L_α production cannot be obtained. A triple coincidence experiment which measures both fragments and the photon will uniquely specify the scattering angles of the two particles with the advantage of collecting information about polarized L_α production. One can effectively "pin down" all the kinematics and also the center-of-mass deflection of the molecule for the process studied in this work.

APPENDIX D

TRANSFORMATION OF P_1 TO THE MOLECULAR FRAME

In Ch.3, the ratio σ_0/σ_1 was related to the integral alignment parameter A_{20} . However A_{20} was related to P_1. If the internuclear axis of the parent molecule is oriented at an angle ϕ with respect to the beam axis, then it is more convenient to write P_1 in the molecular frame in order to calculate σ_0/σ_1.

Note that I(0°,0°,0°) is proportional to $|E_z|^2$ and I(90°,0°,0°) is proportional to $|E_x|^2$, where E_z and E_x are the dipole fields parallel and perpendicular to the incident beam direction, respectively. Therefore, a transformation of P_1 requires a rotation of E_z and E_x about the y-direction through an angle ϕ (see Fig. 3.2 for the geometry). The orthogonal transformation is given by (see Fig. D.1; see also Boas 1983)

$$\begin{pmatrix} E_x' \\ E_y' \end{pmatrix} = \begin{pmatrix} \cos\phi & \sin\phi \\ -\sin\phi & \cos\phi \end{pmatrix} \begin{pmatrix} E_z \\ E_x \end{pmatrix}. \qquad \text{(D.1)}$$

Thus P_1 is written as

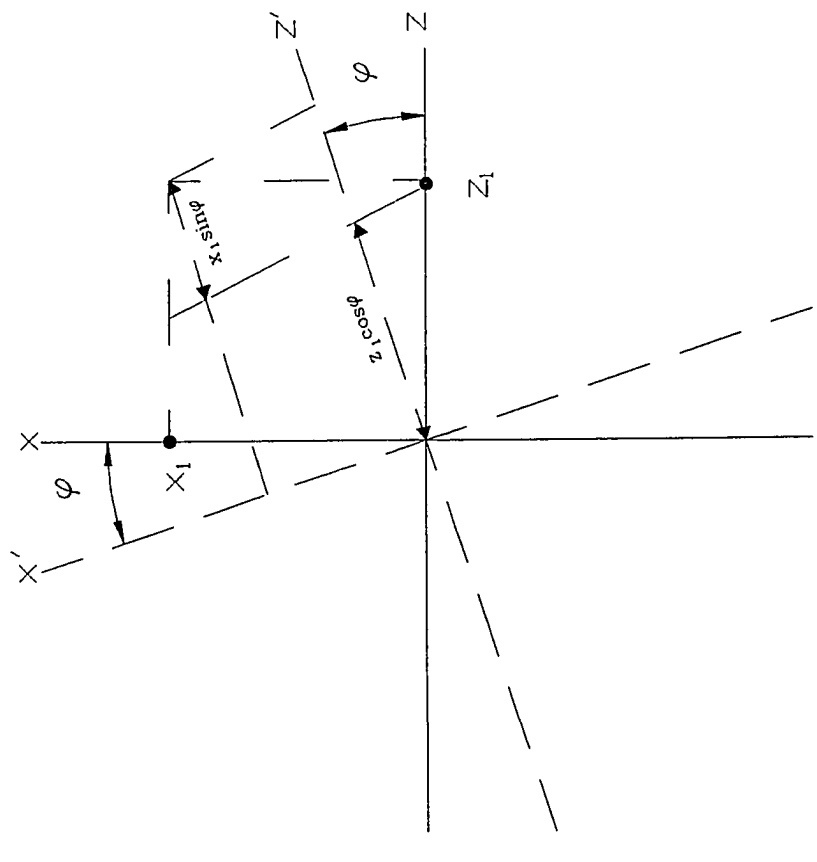

Figure D.1: Diagram illustrating an orthogonal transformation. The y-direction is perpendicular to the plane of the page.

$$P_1 = \frac{(I(0°)-I(90°)\cos 2\phi+2\sqrt{I(0°)I(90°)}\sin 2\phi}{I(0°)+I(90°)}. \qquad (D.2)$$

By applying equation (3.11) and writing the intensities in terms of the fitting parameters A and B the ratio σ_0/σ_1 becomes

$$\frac{\sigma_0}{\sigma_1} = -\frac{11B\cos(2\phi)-22\sqrt{A(A+B)}\sin(2\phi)-3(2A+B)}{7B\cos(2\phi)-14\sqrt{A(A+B)}\sin(2\phi)+3(2A+B)}. \qquad (D.3)$$

APPENDIX E

Production of near-zero energy projectile-frame protons in H_2^+ -He collisions at 4 keV

Reprinted from

Physical Review A, 41, 5934 (1990)

PHYSICAL REVIEW A VOLUME 41, NUMBER 11 1 JUNE 1990

Production of near-zero-energy projectile-frame protons in H_2^+-He collisions at 4 keV

D. H. Jaecks, O. Yenen, L. Wiese, and D. Calabrese
Behlen Laboratory of Physics, University of Nebraska, Lincoln, Nebraska 68588-0111
(Received 1 February 1990)

The dominant processes for producing near-zero-energy projectile-frame protons in H_2^+-He collisions at 4-keV ion energy have been experimentally identified. The $1s\sigma_u$ to $2p\pi_u$ and $3d\sigma_g$ transitions that produce these protons occur at internuclear separations of the H_2^+ ion that are 2.5–3 times the equilibrium separation.

INTRODUCTION

The study of inelastic processes in kilo-electron-volt H_2^+-He collisions continues to be of topical interest. Even though this and the He^+-H_2 system have been the subject of numerous investigations over the past 25 years, many aspects of the various inelastic processes in these systems are not well understood. For example, Quintana *et al.*[1,2] recently reported probabilities for $He(n=2)$ excitation in 1–3-keV H_2^+-He collisions that are larger than expected from the consideration of molecular-orbital (MO) models.[3,4] Russek and Furlan[5] have recently published initial MO calculations, which provide a qualitative picture of how this excitation can occur at c.m.-to-c.m. separations of less than 0.05 nm.

A large number of previous experiments involve the measurement of H^+ laboratory energy spectra that result from the collision-induced dissociation of H_2^+. A continuing problem in these experiments is the identification of the excited states of H_2^+ that contribute to the proton spectra.[6] This is an important problem since the HeH_2^+ system has become a prototype for the study of the dynamics of atom-molecule collisions. If one hopes to understand this system at a fundamental level, the various inelastic processes must be identified. This paper addresses one aspect of this long-standing identification problem.

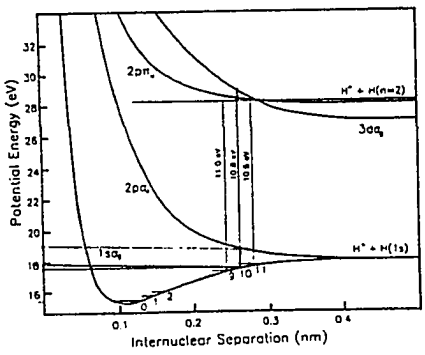

FIG. 1. Relevant electronic states of H_2^+. Location of $v=0,1,2,\ldots,9,10,11$ are also indicated.

The electronic excitation of H_2^+, with the possible exception of the $3d\sigma_g$ and $2p\pi_u$ states at internuclear separations greater than 0.286 nm, leads to direct dissociation into $H^+ + H(nl)$. The bound states of $3d\sigma_g$ can dipole radiate to the antibonding $2p\sigma_u$ state and the $2p\pi_u$ state can radiate to the bound or unbound component of $1s\sigma_g$ state, depending upon the internuclear separation. It has been shown that the $2p\pi_u$ and $3d\sigma_g$ electronic levels support bound vibrational states for internuclear separations greater than about 0.286 nm.[7] At keV collision energies, the rotation and vibration times of H_2^+ are short compared to collision times; therefore, the fixed-nucleus approximation can be used in any description of the collision process. For the case when the final H^+ projectile-frame velocity, upon dissociation, is parallel or antiparallel to the beam direction and assuming no deflection of H_2^+, the H^+ laboratory kinetic energy, due to H_2^+ excitation and dissociation, can readily be written

$$E(H^+)=(E_0-Q)/2+\varepsilon/2\pm\tfrac{1}{2}[(E_0-Q)\varepsilon]^{1/2},$$

where E_0 is the initial kinetic energy of H_2^+, Q is the inelastic energy loss during the collision, and ε is the excitation energy of H_2^+ above the dissociation limit of $H^+ + H(n,l)$. The initial H_2^+ is in a vibrational distribution when produced by ionization of H_2 in an electron impact or H_2-discharge source. Since the electronic eigenenergies are functions of the internuclear separation, a distribution of Q's and associated ε's contributes to a measured H^+ laboratory kinetic energy distribution. Figure 1 shows the bound and excited states that are relevant to our discussion.

EXPERIMENT

A typical H^+ laboratory energy distribution is shown in Fig. 2 for 4-keV H_2^+-He collisions that is similar to that measured by previous investigators.[6] The apparatus used to measure this distribution has been described in our previous work.[8,9] The H_2^+ was formed in a duoplasmatron source; however, for our present measurements, the axial magnetic field of the source was turned

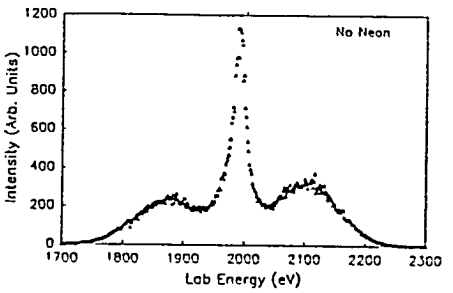

FIG. 2. On-beam-axis laboratory energy spectrum of protons from 4-keV H_2^+-He collisions.

off. After momentum analysis by a magnetic field, the collimated H_2^+ beam was passed through a differentially pumped collison cell maintained at single collision pressures. The kinetic energies of the H^+ produced from H_2^+ excitation and dissociation were measured by a large parallel-plate analyzer placed 0.845 m beyond the collision cell. The acceptance angle of the H^+ detection system at 0° scattering relative to the beam axis was ±0.03°. The distance between the entrance slit of the analyzer and the detector position was 0.5334 m.

The finite-sized detector at 0° is most efficient in collecting protons that have zero or near-zero energy in the c.m. of the moving H_2^+. Thus, the single, central peak in the energy spectra results from protons that dissociate from H_2^+ states with $\epsilon \approx 0$. Because of this sensitivity the measured laboratory distribution is a maximum at $E(H^+)=(E_0-Q_0)/2$, where Q_0 is the inelastic energy loss associated with transitions to levels of H_2^+ that dissociate with near-zero kinetic energy. The energy loss Q_0 may also have a distribution of values, depending upon the processes that contribute to near-zero-energy protons.

DISCUSSION

Several experimental studies have been directed toward the understanding and identification of the exact processes that produce near-zero-energy protons from the collision-induced dissociation of H_2^+. Fournier *et al.*[6] have most recently discussed some of these and include (a) $1s\sigma_g \rightarrow 2p\sigma_u$ electronic excitation from highly excited vibrational states at very large internuclear separation; (b) vibrational excitation into the continuum, with H_2^+ remaining in the electronic ground state; and (c) predissociation from collisionally produced vibrationally and rotationally excited, quasibound states, by tunneling through the angular momentum barrier.

We have included in Fig. 1 another process, namely, direct electronic excitation of the $2p\pi_u$ and $3d\sigma_g$ states from $1s\sigma_g$ vibrational levels at or near $v=11$. The energies of the $2p\pi_u$ and $3d\sigma_g$ states cross near an internuclear separation of $R=0.286$ nm. This crossing also occurs at an energy that nearly coincides with the $H^+ + H(n=2)$ dissociation limit, so any excitation of these two levels near $R=0.286$ nm, with $\epsilon \geq 0$, would give rise to protons of near-zero energy in the H_2^+ c.m. frame. Even with $\epsilon = 40$ meV, the dissociation time is on the order of 10^{-13} sec. It also should be noted that the $2p\pi_u$ state has a 40-meV potential barrier at an internuclear separation $R \approx 4$ nm. The indicated electronic excitation at $R=0.286$ nm would give an inelastic energy loss of $Q_0 \approx 10.6$ eV or slightly larger.

The three processes previously mentioned would give inelastic energy losses in the range of 0, 0–3.2, and 0–3.2 eV, respectively. If target excitation were to occur during the excitation, one would need to add another 20 eV to all of these numbers. We mention this possibility because Peek[10] has shown that within the Born approximation there is also the possibility of simultaneous target and H_2^+ excitation. Also the recent experimental and theoretical work of Quintana *et al.*[1] and Russek and Furlan[5] has shown that the target excitation channel in H_2^+-He collisions is readily accessible at small collision distances. At such distances, temporal distortion of the electron cloud, around the three nuclei, during the collision, would change the screening and the interaction force between the two protons. Such a transient change in the effective proton-proton interaction, during the collision, could lead to vibrational excitation to the continuum of the ground electronic state.

From the measured position of the central peak of the H^+ energy distribution, we have determined the value of $(E_0-Q_0)/2$ for 4-keV H_2^+ energies. This energy was chosen to study in detail, because it is in this energy region where the H_2^+ excitation and dissociation into $H(2p)+H^+$ has the largest cross section.[11] We find from 25 separate measurements a value of $Q_0=11.6\pm1.0$ eV, where the quoted error is one standard deviation. Within experimental error, this corresponds to the value of $1s\sigma_g \rightarrow 2p\pi_u$ or $1s\sigma_g \rightarrow 3d\sigma_g$ transitions at or near the internuclear separation of $R \approx 0.286$ nm. The $2p\pi_u$ state leads to $H^+ + H(2p_{\pm 1})$, upon dissociation, with the internuclear axis as the axis of quantization, and the $3d\sigma_g$ state leads to the Stark state, with equal contributions of $H^+ + H(2s)$ and $H^+ + H(2p_0)$.

Thus our initial conclusion from the measurement of Q_0 is that when high vibrational states of H_2^+ are present with sufficient probability ($v \approx 9$ or greater), the dominant process for producing near-zero-energy protons is electronic transitions from the ground $1s\sigma_g$ to the $2p\pi_u$ or $3d\sigma_g$ states, even though these initial vibrational states are not the most highly populated. An H_2^+ vibrational distribution, given by the Franck-Condon overlap of the H_2 ground vibrational state and the vibrational states of the $1s\sigma_g$ state, suggests that about 5% of the H_2^+ ions are in the $v=9$ to $v=11$ vibrational states.[12] We cannot experimentally distinguish between the $2p\pi_u$ and the $3d\sigma_g$ states from analysis of the H^+ states.

To test this conclusion further, we tried to alter the vibrational distribution of the H_2^+ inside the source by using a mixture of Ne and H_2, rather than just H_2. Herman and Pacak[13] have shown that for an electron-impact

source, the reaction at thermal energies within the source,

$$H_2^+(v)+Ne \rightarrow HNe^+ + H ,$$

occurs for H_2^+ vibrational quantum numbers $v \geq 2$ and not for $v=0,1$. When the $p(Ne)p(H_2)$ pressure in their source was run at a 5/1 ratio, the extracted H_2^+ was almost exclusively in the $v=0,1$ states.

We measured nine different H^+ dissociation spectra, all at different $p(Ne)/p(H_2)$ source pressure ratios. The construction of the source did not permit the direct measurement of the source pressure; however, with a quadrupole mass spectrometer, we were able to monitor the ratio in the extractor–einzel-lens region directly outside the source. We varied this ratio from 1.25 to 15. As the $p(Ne)/p(H_2)$ ratio in the source increased, we found that the peak position of the central peaks of the laboratory H^+ spectra decreased in energy, indicating an increasing effective Q. All of the measured values of the inelastic energy loss, as determined from the peak position of the H^+ spectrum, increased upon the insertion of Ne into the source. For example, at a $p(Ne)/p(H_2)$ pressure ratio of 1.25, $Q=14.0\pm1.0$ eV; at $p(Ne)/p(H_2)=5$, $Q=13.0\pm1.5$ eV; and at $p(Ne)/p(H_2)=15$, $Q=21.0\pm1.0$ eV. Here the quoted errors represent the range of three separate measurements at each pressure ratio.

We also found that the central peak of the laboratory energy distribution decreased relative to the "side peaks," indicating a relative decrease in the number of near-zero-energy protons. This effect is shown in the proton spectrum of Fig. 3 taken when the $p(Ne)/p(H_2)$ pressure ratio was 15/1.

Fournier *et al.*[6] found a similar behavior in the central peak by varying the vibrational distribution using a variable-energy–electron-impact source. The relative height of their central peak compared to the side peaks was the lowest when their electron energy was just sufficient to ionize H_2 to the lowest three vibrational states. The peak increased in size as the electron energy increased and as higher vibrational states in the source were populated.

We conclude that the insertion of Ne into the source does indeed depopulate the upper H_2^+ vibrational levels, at least to a degree that processes other than $1s\sigma_g \rightarrow 2p\pi_u, 3d\sigma_g$ electronic transitions become relatively important in producing near-zero c.m.-energy protons. The other possible processes have been mentioned earlier. Fournier *et al.*[6] did not consider this electronic process.

We must also consider the possible effect of significant deflection of the H_2^+ during the collision and the effect of it upon the interpretation of the data. Meierjohann and Vogler have experimentally shown that electronic excitation of H_2^+ in H_2^+-He collisions at 10 keV occurs only for H_2^+ scattering angles of less than 0.10°.[14] This extrapolates to 0.25° for a 4-keV energy if we assume, as in the diatom case, that the product of the laboratory scattering angle and incident ion energy, θE, is a measure of the distance of closest approach. The question arises, whether in the case of 0.25° scattering, there is any alteration of the interpretation of the shift in central peak of the energy spectra. In Fig. 4(a) we schematically show the Newton diagram whereby the H_2^+, with initial momentum P_0, is deflected through some laboratory angle θ_s, with a resulting final laboratory momentum P_L before dissociation. The recoil momentum of the He target is P_R.

One would still observe a single peak in the H^+ laboratory energy spectrum, on the beam axis, if $v_{c.m.}$ of the H^+ upon dissociation were 90° to the beam axis, as shown in Fig. 4(b), where V_p is the H^+ laboratory velocity at the single central peak position. Angles, other than 90°, would result in pairs of front-back peaks relative to the central peak.

From the elementary energy and momentum considerations suggested by Fig. 4 one can show for a given θ_s that the central peak position energy of H^+ can be written

$$E_p(H^+)=E_0/2-(Q_i+\varepsilon+E_R)/2 ,$$

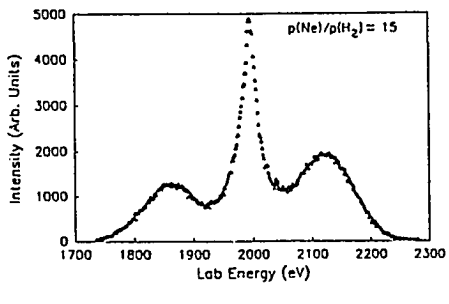

FIG. 3. On-beam-axis laboratory energy spectrum of protons from 4-keV H_2^+-He collisions, with $p(Ne)/p(H_2)$ source ratio 15/1.

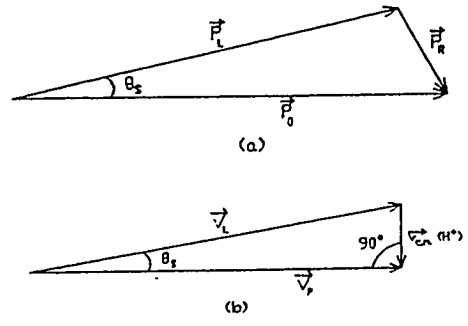

FIG. 4. (a) Momentum scattering diagram when H_2^+ suffers deflection. (b) Velocity diagram necessary to produce a single proton energy peak, if H_2^+ suffers deflection.

where Q_i is the combined inelastic excitation energy of the target and projectile, ϵ is the excitation energy of H_2^+ above the dissociation limit, and E_R is the recoil energy imparted to the He target.

The shift of this central peak from $E_0/2$ is a measure of the second term above if H_2^+ deflection occurs for a *majority* of the observed protons. Experimentally, we have measured this term to be from 11.6–21 eV, depending upon the $p(\mathrm{Ne})/p(H_2)$ concentration ratio in the source.

As we have pointed out, we expect c.m. deflections of less than 0.25°. The values of Q_i and ϵ, for any given scattering angle, and any *measured* shift $(Q_i+\epsilon+E_R)$, must be consistent with the energy-level diagrams of the H_2^+, and He systems. We also require that $Q_i > \epsilon$.

The recoil energy E_R of the He target is not strongly dependent upon Q_i. For a scattering angle of $\theta_1 = 0.50°$, E_R varies from 0.15 to 0.18 eV as Q_i varies from 10 to 30 eV. From Fig. 4, we can determine that $\epsilon = (E_0 - Q_i - E_R)\sin^2\theta_1$. Using this value of ϵ in the expression for the shift of the peak position, we find that for $\theta_1 = 0.5°$ the Q_i is 0.5 eV less than the Q determined when no H_2^+ scattering was assumed. Thus the original Q of 11.6 eV would have to be decreased by about 0.5 eV if significant deflection occurred. Such a decrease would not change the interpretation of the data regarding the process that produces near-zero-energy protons.

We have also shown that by depleting the higher vibrational states, $v=9$ through 11, the inelastic energy loss for the reaction that produces near-zero-energy protons shifts to 21 eV. Such an inelastic energy loss is consistent with simultaneous excitation of the He target and vibrational excitation of H_2^+ to the continuum and is consistent with the latest work of Quintana *et al.*[1] and Russek and Furlan.[5]

CONCLUSION

We have provided experimental evidence that the dominant process for producing near-zero-energy protons in H_2^+-He collisions, at 4-keV collision energy, is electronic excitation from high vibrational states of the bound $1s\sigma_g$ electronic state to the $2p\pi_u$ and/or $3d\sigma_g$ antibonding states. Such transitions occur for large proton-proton separations of 0.286 nm, which are 2.5–3 times the equilibrium separation. It is interesting that at large internuclear separations these electronic transitions have larger probabilities than transitions to the $2p\sigma_u$ state. The mechanism for such transitions is not yet known. We have also shown that the vibrational distribution of the H_2^+ ion can be altered by insertion of Ne in the H_2 discharge source.

ACKNOWLEDGMENTS

This work was supported by the National Science Foundation through Grant No. PHY-8701905.

[1]E. J. Quintana, A. Andriamsay, D. J. Sneider, and E. Pollack, Phys. Rev. A 39, 5045 (1989).
[2]Nicholas J. Kirchner, Anthony O'Keefe, James R. Gilbert, and Michael T. Bowers, Phys. Rev. Lett. 52, 26 (1983).
[3]D. Dowek, D. Dhuciq, V. Sidis, and M. Barat, Phys. Rev. A 26, 746 (1982).
[4]C. Kubach, C. Courbins-Gaussorques, and V. Sidis, Chem. Phys. Lett. 119, 523 (1985).
[5]Arnold Russek and Richard J. Furlan, Phys. Rev. A 39, 5034 (1989).
[6]P. G. Fournier, A. G. Brenton, P. Jonathan, and J. H. Beynon, Int. J. Mass Spectrom. Ion Phys. 79, 81 (1987), and references therein.
[7]C. L. Beckel, M. Shafi, and J. M. Peek, J. Chem. Phys. 59, 5288 (1973); M. Shafi and C. L. Beckel, *ibid.* 59, 5294 (1973).
[8]O. Yenen, D. H. Jaecks, and L. M. Wiese, Phys. Rev. A 39, 1767 (1989).
[9]R. H. McKnight and D. H. Jaecks, Phys. Rev. A 4, 2281 (1971).
[10]J. M. Peek, Phys. Rev. 140, 769 (1965).
[11]B. Van Zyl, Duane H. Jaecks, and R. Geballe, Phys. Rev. 136, 1561 (1964).
[12]Gordon H. Dunn, J. Chem. Phys. 44, 2592 (1966).
[13]Z. Herman and V. Pacak, Int. J. Mass. Spectrom. Ion Phys. 24, 355 (1977).
[14]B. Meierjohann and M. Vogler, Z. Phys. A 282, 7 (1977).

REFERENCES

N. Anderson, J.W. Gallagher, and I.V. Hertel, Phys. Rep. **165**, 1 (1988), and references therein.

N. Anderson, in: *Fundamental Processes of Atomic Dynamics*, J.S. Briggs, H. Kleinpoppen, and H.O. Lutz, eds., Plenum Press 1988, p.311.

R. Anholt, Rev. Mod. Phys. **57**, 995 (1985).

M. Barat and W. Lichten, Phys. Rev. A **6**, 211 (1972).

D. Basu, S.C. Mukherjee, and D.P. Sural, Phys. Rep. **42C**, 145 (1978).

D.R. Bates, K. Ledsham, and A.L. Stewart, Phil. Trans. Roy. Soc. London **A246**, 215 (1953).

D.R. Bates and R. McCarroll, Adv. Phys. **12**, 39 (1962).

C.L. Beckel, M. Shafi, and J.M. Peek, J. Chem. Phys. **59**, 5288 (1973).

K. Blum, and H. Jackubowicz, J. Phys. **B11**, 909 (1978).

M.L. Boas, *Mathematical Methods in the Physical Sciences*, (John Wiley & Sons, New York, 1983), p. 410.

S.V. Bobashev, Adv. At. Mol. Phys. **14**, 341 (1978).

M. Born and J. Oppenheimer, Ann. Physik **84**, 457 (1927).

D. Calabrese, O. Yenen, L.M. Wiese, and D.H. Jaecks, Rev. Sci. Instrum. (submitted for publication, 1993).

D. Dowek, D. Dhuicq, V. Sidis, M. Barat, Phys. Rev. A **26**, 746 (1982).

G.H. Dunn, J. Chem. Phys. **44**, 2592 (1966).

C. Dupré, A. Lahmam-Bennani, and A. Duguet, Meas. Sci. Technol. **2**, 327 (1991).

U. Fano and L. Fano, *Physics of Atoms and Molecules An Introduction to the Structure of Matter*, (University of Chicago Press, Chicago, 1972), p. 443.

U. Fano and W. Lichten, Phys. Rev. Lett. **14**, 627 (1965).

U. Fano and J. Macek, Rev. Mod. Phys. **45**, 553 (1973).

L. Fornari, Ph.D. Thesis, UNL (1981).

P.J. Fournier, A.G. Brenton, P. Jonathan, and J.H. Beynon, Int. J. Mass Spectrom. Ion Phys. **79**, 81 (1987), and references therein.

D.K. Gibson and J. Los, Physica **35**, 258 (1967).

C. Greene, (University of Colorado, unpublished lecture series, 1981).

J. Heinrichs, Phys. Rev. **176**, 141 (1968), and references therein.

G. Herzberg, *Electronic Spectra of Diatomic Molecules*, (D. Van Nostrand, New York, 1966), p.315.

R. Hoffman, G. Gaukler, G. Nolte, H. Schmidt-Bocking, and R. Schuch, Nucl. Instr. and Meth. **197**, 391 (1982).

F. Hund, Z. Phys. **40**, 742 (1927).

J.D. Jackson, *Classical Electrodynamics*, (John Wiley & Sons, New York, 1975), p. 394.

D.H. Jaecks, W. de Rijk, and P.J. Martin, in: *Proceedings of the Seventh International Conference on the Physics of Electronic Atomic Collisions, Amsterdam, 1971*, L.M. Branscomb, E. Ehrhardt, R. Geballe, F.J. de Heer, N.V. Fedorenko, J. Kistemaker, M. Barat, E.E. Nikitin, and A.C.H. Smith eds., (North-Holland,

Amsterdam, 1972), p. 424.

D.H. Jaecks, O. Yenen, M. Natajaran, and D. Mueller, Phys. Rev. Lett. **50**, 825 (1983).

D.H. Jaecks, O. Yenen, L. Wiese, and D. Calabrese, Phys. Rev. A **41**, 5934 (1990).

R. Kato, J. Phys. Soc. Japan **16**, 2525 (1961).

Q.C. Kessel and B. Fastrup in: *Case Studies in Atomic Physics III*, E.W. McDaniel and M.R.C. McDowell, eds., American Elsevier Publishing Company, New York, 1974, p. 140.

M. Kimura and N.F. Lane, Adv. At. Mol. Phys. **26**, 79 (1990).

C. Kubach, C. Courbin-Gaussorgues, and V. Sidis, Chem. Phys. Lett. **119**, 523 (1985).

P.J. Kuntz, Chem. Phys. Lett. **16**, 581 (1972).

A.H. Laufer, J.A. Pirog, J.R. McNesby, J. Opt. Soc. Am. **55**, 64 (1965).

W. Lichten, J. Phys. Chem. **84**, 2102 (1980), and references therein.

W. Lichten, Phys. Rev. **131**, 229 (1963).

W. Lichten, Phys. Rev. **164**, 131 (1967).

J. Los and T.R. Grovers, in: *Collision Spectroscopy*, R.G. Cooks cd. Plenum Press, New York 1978, p. 289.

J.H. Macek and D.H. Jaecks, Phys. Rev. A **4**, 1288 (1971).

H.A. Macleod, *Thin Film Optical Filters*, (American Elsevier Publishing Company, New York, 1969), p.30.

M.M. Madsen and J.M. Peek, Atomic Data **2**, 171 (1971).

I.C. Malcom and J.W. McConkey, J. Phys. B **12**, 267 (1979).

P.J. Martin, Ph.D. Thesis, UNL (1975).

D.R. McLaughlin and D.L. Thompson, J. Chem. Phys. **70**, 2748 (1979).

D.L. Montgomery, Ph.D. Thesis, UNL (1982).

R.S. Mulliken, Phys. Rev. **32**, 186 (1928).

J.V. Neumann and E. Wigner, Physik Z., **30**, 467 (1929).

E.D. Palik, *Handbook of Optical Constants of Solids*, (Academic, Orlando, Fla., 1985), Table X, p. 753.

I.C. Percival and M.J. Seaton, Phil. Trans. Roy. Soc. London **251**, 113 (1958).

E. Pollack and Y. Hahn, Adv. At. Mol. Phys. **22**, 243 (1986).

H. Rosenthal and H.M. Foley, Phys. Rev. Lett. **23**, 1480 (1969).

A. Russek and R. Furlan, Phys. Rev. A **39**, 5034 (1989).

J.A.R. Samson, *Techniques of Vacuum Ultraviolet Spectroscopy*, (Wiley, New York, 1967) Chap. 6, p. 180; Tab. 9.3, p. 312.

E.G. Schneider, Phys. Rev. **49**, 341 (1936).

M. Shafi and C.L. Beckel, J. Chem. Phys. **59**, 5294 (1973).

V. Sidis and D. Dowek, in: *Electronic and Atomic Collisions*, invited papers of XIII International Conference on the Physics of Electronic and Atomic Collisions, Berlin, July 1983, J. Eichler, I.V. Hertel, and N. Stolterfoht eds. (North Holland, Amsterdam, 1984), p. 403.

O.H.W. Siegmund, M. Lampton, J. Bixler, S. Bowyer, and R.F. Malina, IEEE Trans. Nucl. Sci. **NS-33**, 724 (1986).

G.G. Stokes, Proc. Roy. Soc. (London) **11**, 545 (1862).

P.J.O. Teubner, W.E. Kaupila, W.L. Fite, and R.J. Girnius, Phys. Rev. A **2**, 1763 (1970).

R.J. Van Brunt and R.N. Zare, J. Chem. Phys. **48**, 4304 (1968).

B. Van Zyl, D.H. Jaecks, and R. Geballe, Phys. Rev. **136**, 1561 (1964).

A.B. Wedding, A.G. Mikosza, and J.F. Williams, Opt. Soc. Amer. **8**, 1729 (1991).

L.M. Wiese, M.S. Thesis, UNL (1993).

J.L. Wiza, P.R. Henkel, and R.L. Roy, Rev. Sci. Instrum. **46**, 1217 (1977).

Rev. G.D. Yarnold, H.C. Bolton, J. Sci. Instr. **26**, 38 (1949).

O. Yenen, Ph.D. Thesis, UNL (1986).

O. Yenen, D.H. Jaecks, and L.M. Wiese, Phys. Rev. A **39**, 1767 (1989).

O. Yenen, L.M. Wiese, D. Calabrese, and D.H. Jaecks, Phys. Rev. A **42**, 324 (1990).

R.N. Zare, J. Chem. Phys. **47**, 204 (1967).

F.P. Ziemba and E. Everhart, Phys. Rev. Lett. **2**, 299 (1959).